NATIONAL AERONAUTICS AND SPACE ADMINISTRATION

Technical Report No. 32-722

The Mariner II Microwave Radiometer Experiment

Douglas Emron Jones

JET PROPULSION LABORATORY
CALIFORNIA INSTITUTE OF TECHNOLOGY
PASADENA, CALIFORNIA

January 1, 1966

NATIONAL AERONAUTICS AND SPACE ADMINISTRATION

Technical Report No. 32-722

The Mariner II Microwave Radiometer Experiment

Douglas Emron Jones

R. H. McFee, *Manager*
Lunar and Planetary Sciences Section

JET PROPULSION LABORATORY
CALIFORNIA INSTITUTE OF TECHNOLOGY
PASADENA, CALIFORNIA

January 1, 1966

Prepared Under Contract No. NAS 7-100
National Aeronautics & Space Administration

CONTENTS

TABLES

FIGURES

FIGURES (Cont'd)

FIGURES (Cont'd)

ABSTRACT

Aboard the *Mariner II* spacecraft was a dual-channel microwave radiometer, which obtained three scans across the planet Venus at wavelengths of 13.5 and 19 mm. The relationship of the peak temperature values of the three scans supports a hot-surface model for the planet. Several atmosphere–surface configurations were assumed in an attempt to match the limb-darkening ratios and temperature values measured at both wavelengths. The model that agrees most closely with the data is one that consists of a specular surface and an isothermal cloud-type layer at a temperature near 350°K. The anomaly that occurred toward the end of scan 2 was in the same region of the planet as that observed by the terrestrial measurements at 8 to 14 microns and is consistent with a marked increase in opacity of the 350°K cloud layer in this region. The marked difference between the 13.5- and 19-mm temperatures indicates the presence of an abrupt discontinuity in the microwave spectrum of Venus that cannot be due to uncondensed water vapor and hence requires the presence of a molecule or molecules in the atmosphere of Venus that condense or polymerize into liquid form at $T \geq 350°K$ and exhibit line spectra in the vicinity of 13.5 mm and shorter.

The magnitude of the relative dielectric coefficient of the surface is found to lie between 3 and 4. The surface temperature variation that best fits the data is of the form $T_s = 700°K + (80 \pm 5)°K \cos \phi$. An upper limit of ~100 atmospheres for the surface pressure is obtained for an atmosphere containing 20% CO_2 and 80% N_2.

I. BACKGROUND AND CONCEPTION OF THE EXPERIMENT

Previous measurements of the microwave brightness temperature of the planet Venus have referred to an average over the planetary disc, because of the poor spatial resolution of ground-based radio telescopes. Measurements related to specific regions of the planet were required in order to substantiate or eliminate some of the models proposed for the atmosphere and surface conditions of the planet.

A. The Problem

It was the purpose of this experiment to obtain high-spatial-resolution measurements of the planet Venus at two microwave wavelengths, 13.5 and 19 mm. Specifically, the objectives were:

1. To investigate the variations in intensity at 13.5- and 19-mm wavelengths from different portions of the planetary disc, including the daylight and dark hemispheres, the poles, and the region of the terminator.

2. To establish the place of origin of, and the radiation mechanism responsible for, the observed centimeter- and millimeter-wavelength radiation.

By 1960, the exploration of the solar system was beginning to move at such a pace that thought was being given to atmospheric entry capsules and soft landers for the planets. At that time there were a number of models postulated for Venus, and it was important that the correct model category be determined and that detailed information regarding the specific model be obtained. Some conclusions leading to the hot-surface class of models had been reached by a majority of the workers in the field, based upon interpretations of various measurements in a number of wavelength regions. However, difficulties with this class of models motivated a number of workers to consider nonthermal mechanisms to explain some of the observations.

B. Ground-Based Observations of Venus

The first observations of the planet Venus at microwave wavelengths were by Mayer, McCullough, and Sloanaker (Ref. 1) in 1956. Their measurements at 3.15 and 9.4 cm resulted in brightness temperature values of 560 ± 73°K and 580 ± 160°K respectively and related to the dark portion of the planet. These temperatures were much greater than the 8- to 14-micron temperature of about 230°K obtained by Petit and Nicholson (Ref. 2) and later confirmed by Sinton and Strong (Ref. 3). In addition, the rotational temperature of CO_2, as determined from the intensity distribution of the vibration rotation bands at 7820 and 8689 Å obtained by Chamberlain and Kuiper (Ref. 4), was about 285°K, based upon radiation transfer theory. The microwave measurements obviously referred to a different region of the planet.

The short-centimeter measurements of Mayer et al. (Ref. 1) caused a number of measurements to be made, extending from 4 mm to 21 cm. These observations showed that the brightness temperature of the planet was approximately 600°K for wavelengths of 3 cm and longer. On the other hand, for wavelengths of 4 and 8 mm, a brightness temperature of 350 to 400°K was appropriate. If all of the microwave data obtained were given equal weight, a somewhat confused picture for the planet resulted.

The several characteristics of the microwave data stimulated many theoretical investigations that were related to Venus and directed principally toward defining the origin of the high-temperature emission. Such investigations led to models that also predicted the basic shape of the curve for brightness temperature vs wavelength, extending from 4 mm to the long-centimeter region.

Most of the theoretical discussions have either assumed or tried to justify a high-temperature surface as the origin of the centimeter radio emissions (Refs. 5–9), but alternative explanations have suggested that the origin is thermal emission from the ionosphere (Ref. 10), fluctuating charges on particles in the atmosphere (Ref. 11), or plasma instabilities in the ionosphere (Refs. 12 and 13). These latter models allowed for cooler surface temperatures. Roberts (Ref. 14) has given a recent review of these topics.

If one ruled out the dense-ionosphere model, primarily because of the results of the radar experiments, there still remained the fluctuating-charge and plasma-instability models. Though somewhat unrealistic by terrestrial standards, they were no more unrealistic than the suggested high temperatures of the greenhouse or aelospheric models. It was apparent that as more workers considered the problem of the microwave temperature

of Venus, a large number of models would be forthcoming that would be difficult, if not impossible, to substantiate definitely or to eliminate by radio or radar observations from the Earth.

C. Development of the Experiment

In 1960, a 4-channel microwave radiometer experiment operating at wavelengths of 4.0, 8.0, 13.5, and 19 mm was proposed and accepted for a NASA flyby mission by the Jet Propulsion Laboratory (JPL) to the planet Venus planned for mid-1962. The spacecraft was designated *Mariner A*, and, weighing about 1100 lb, was to be launched by an *Atlas–Centaur*. Details of the experiment and its objectives have been documented elsewhere (Ref. 15) and consequently will not be reviewed in detail here except to list the experimental objectives (Ref. 16), which were:

1. To establish the place of origin of, and the radiation mechanism responsible for, the observed centimeter- and millimeter-wavelength radiation.

2. To investigate the variations in intensity and spectrum from different positions of the planetary disc, including the daylight and dark hemispheres and the region of the terminator.

3. To place upper limits on the effect of water vapor on the microwave spectrum.

In the summer of 1961 it became apparent that the *Centaur* would not be ready in time to meet the required launch date, and a smaller spacecraft, which was basically a modified *Ranger* type and was designated *Mariner R*, was considered. The launch vehicle was to be an *Atlas–Agena*. The spacecraft weight was only 447 lb, and the total scientific payload was 41 lb.

Several microwave radiometer configurations were considered for this mission, but it was apparent that anything other than a stripped-down version of the *Mariner A* instrument would probably not meet schedules. The possibilities were: one radiometer operating at 4 mm, one at 8 mm, or the dual-channel unit operating at 13.5 and 19 mm. The dual-channel portion appeared more attractive than either of the other two instruments for reasons other than that data at two wavelengths instead of one would be obtained. It was difficult to justify the flying of a one-wavelength channel, because many of the models required a careful comparison of the relative variation observed at two or more wavelengths. A system operating at 13.5 and 19 mm would still allow the first two objectives of the *Mariner A* experiment to be largely achieved. The two-channel portion of the *Mariner A* experiment was proposed and accepted for flight on the *Mariner R* spacecraft. (After launch, the spacecraft was designated *Mariner II*.)

II. IMPLEMENTATION OF THE EXPERIMENT

The microwave instrument and the scan system, as well as the interface between the instrument and the data system, are described in this Section.

A. The Microwave Radiometer

The microwave radiometer flown to Venus on *Mariner II* was of the crystal video type, operating in the standard Dicke mode of chopping between the main antenna, pointed at the target, and a reference horn pointed at cold space. Since the reference horn would see very nearly 0°K, the output voltage of the instrument would be proportional to the source temperature seen by the main antenna. The instrument operated simultaneously at wavelengths centered at 19 mm (15.8 Gc) and 13.5 mm (22.2 Gc). A block diagram of the radiometer is shown in Fig. 1. Figure 2 shows a back view of the instrument with the cover removed, and Fig. 3 shows the instrument mounted on the spacecraft.

This type of radiometer was far inferior to the conventional ground-based types because of its poor sensitivity, but since the main antenna beam for this experiment was to be essentially filled by the planetary disc, the antenna temperature would be perhaps two orders of magnitude higher than for the Earth-based type of observations, and hence good sensitivity was not an important criterion.

For this type of radiometer, it can be shown (Ref. 17) that the change in antenna temperature that produces a change in dc output just equal to the rms noise fluctuations in the output is given by

$$\Delta T_{\text{rms}} = \frac{\pi^2}{8\Delta\nu M_c}\sqrt{\frac{290\,F}{k\,RC}} \tag{1}$$

where

ΔT_{rms} = change in antenna temperature

Δ_ν = predetection bandwidth

M_c = crystal figure of merit

F = noise figure of audio amplifier

k = Boltzmann constant

RC = time constant of the low-pass filter at the output of the phase-sensitive detector

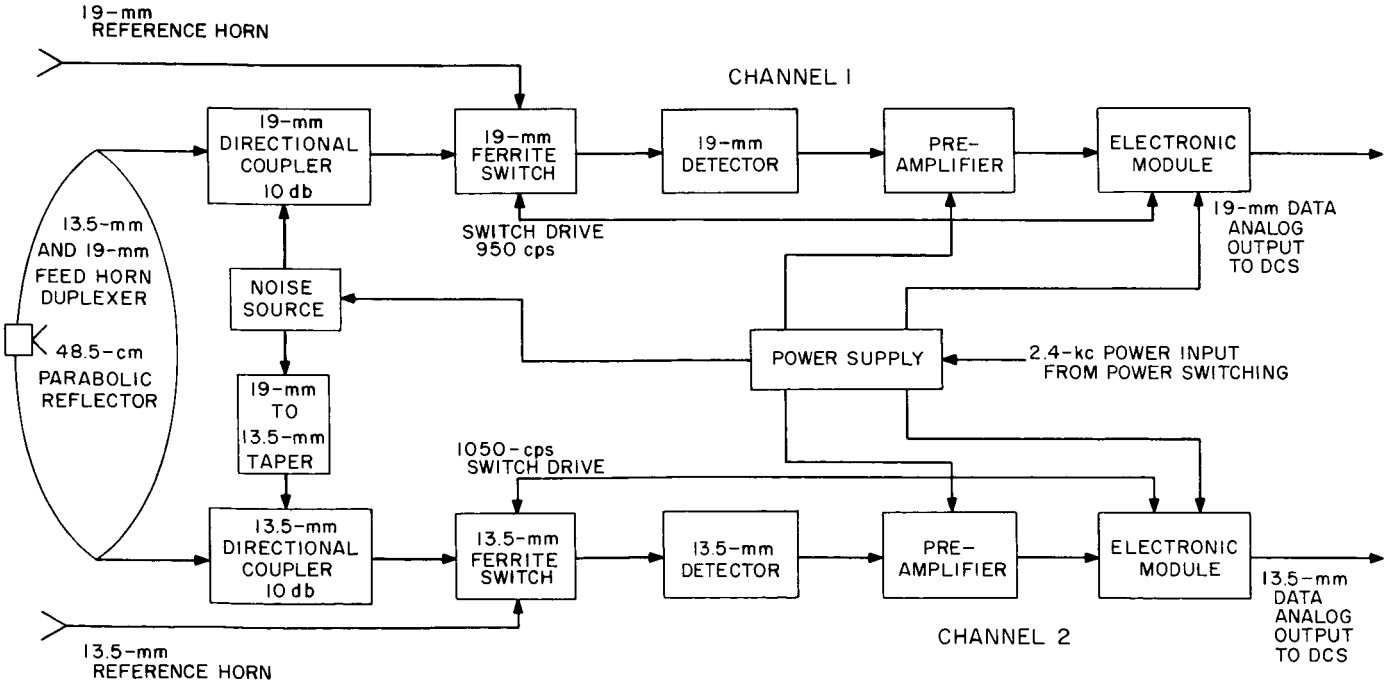

Fig. 1. *Mariner II* microwave radiometer block diagram

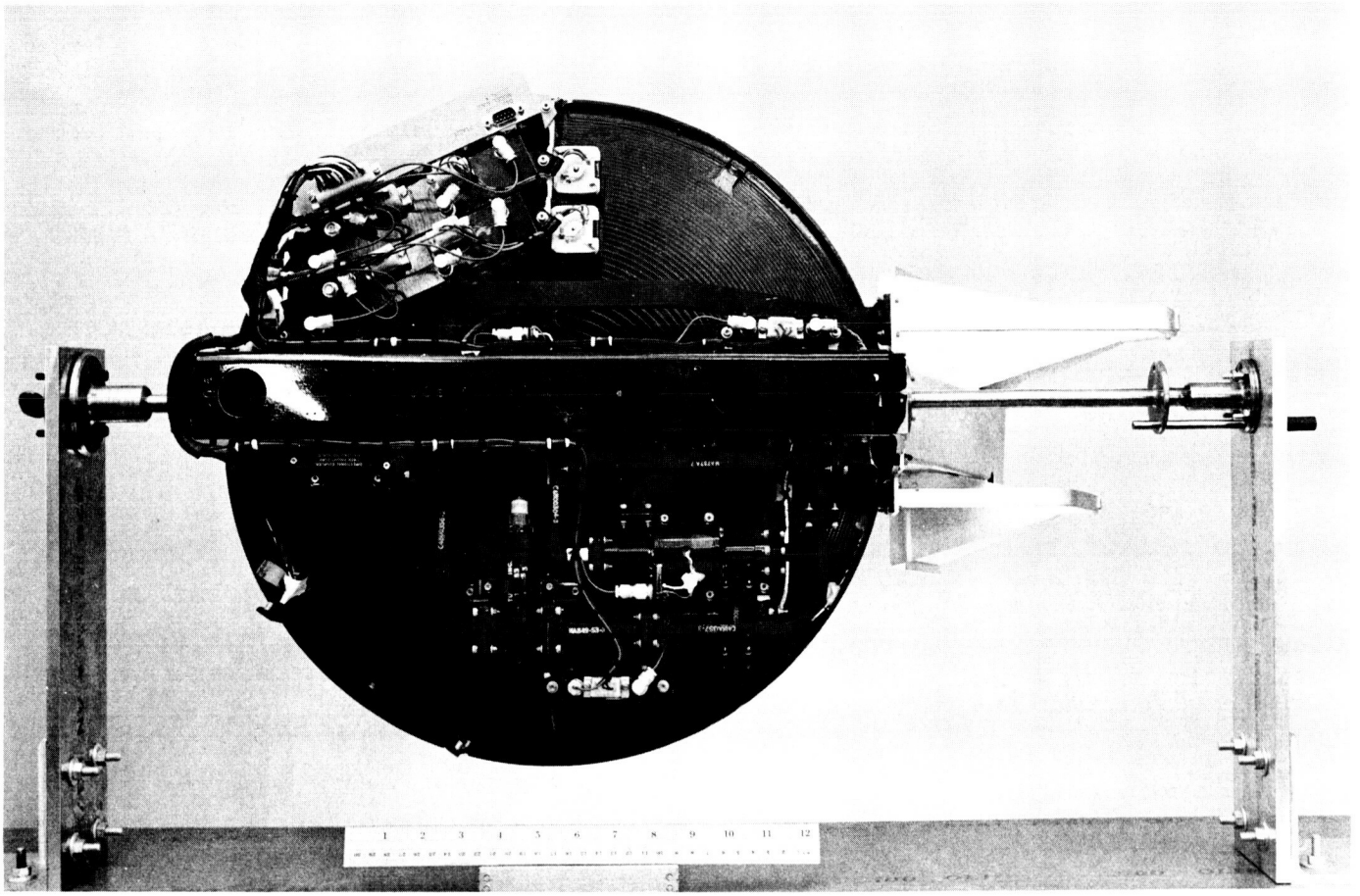

Fig. 2. Rear view of the radiometer with heat shield removed

For $\Delta\nu = 0.1\ \nu$, $M_c = 180$ (at 15.8 Gc), $\Delta\nu = 1.6 \times 10^9$, $F = 4$ db, and $RC = 20$ sec, one obtains $\Delta T_{\text{rms}} \sim 7°\text{K}$. Assuming an antenna efficiency of 0.65 results in a signal-to-noise ratio of 50 to 1 for a 550°K planet.

The design goal to be achieved for the experiment was $\Delta T_{\text{rms}} \leq 8°\text{K}$ for channel 1 (15.8 Gc) and $\leq 5°\text{K}$ for channel 2 (22.2 Gc) with predetection bandwidths of 1.58 and 1.5 Gc respectively. The measured value of ΔT_{rms} on channel 1 was actually better than the design value by almost a factor of 2, but for channel 2 it was about 50% higher than the design goal and consequently, to obtain maximum sensitivity, the predetection bandwidth was opened up until it was limited only by the passband of the ferrite switch, or ~2.5 Gc, thereby causing most of the spectral features of this channel to be lost.

Had the antenna efficiency been 0.65, the signal-to-noise ratios would have been ~70 and ~35 for channels 1 and 2 respectively. However, the measured antenna efficiency was far less than this value. With a black body at ~290°K filling the main beam and first side lobe, a deflection of ~1.0 v was obtained. With ΔV_{rms} ~0.06 v, this would give signal-to-noise ratios at Venus of ~32 and ~21 for channels 1 and 2 respectively. Hence, the efficiency was closer to ~0.4. The decrease in efficiency was found to be primarily due to the diplex feed unit.

A feature of the instrument was a built-in calibration unit. It consisted of a specially ruggedized 5000°K gas discharge tube coupled to both channels through directional couplers, with a taper used in the 13.5-mm channel. The resulting calibration signal into each channel was approximately 350°K. This tube was calibrated against an absorber disc of known temperature and angular size and served as a secondary calibration source (see Section III).

The output voltage was to vary from +1 v dc for 0°K input temperature to +6 v dc for approximately an 800°K input temperature change. The analog voltage output of each channel was sampled by the spacecraft Science Data

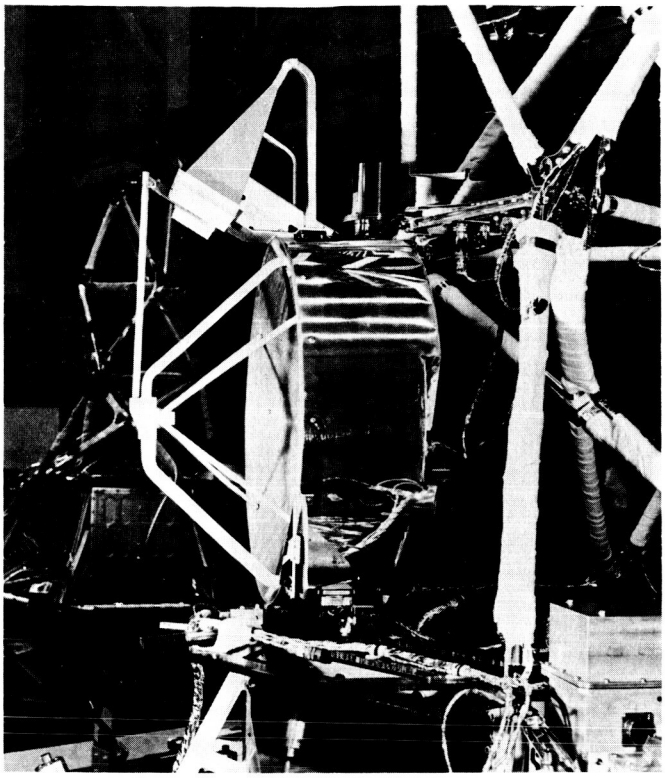

Fig. 3. View of the radiometer shown mounted on the spacecraft

Conditioning System every 20.16 sec to 7-bit accuracy, or in voltage increments of 0.047 v. The two radiometer data channels were sampled 9.6 sec apart.

B. Scan Logic

Because of constraints on weight, on power, and, primarily, on time, it was necessary that the scan logic circuitry obtain the required information regarding the location of the planet (specifically, the limbs of the planet) from the microwave radiometer itself. This imposed very serious constraints on the radiometer, particularly with regard to noise level, sensitivity, and baseline stability.

Trajectory uncertainties required a system that could locate and track the planetary disc anywhere within an arc of $\pm$ 55 deg about the reference plane that contained the Earth–probe–Sun angle. The total angle of scan was chosen to be $\pm$ 60 deg to allow for at least 2 beamwidths being off the planet for baseline data. Weight constraints allowed the scanning mechanism to have only one degree of freedom, with the subsequent motion in a plane fixed perpendicular to the probe–Sun line. The duration of time that the scan plane would intersect the planet was on the order of 30 min. A compromise, caused by the long time constant of the instrument, between degree of coverage of the planetary disc (number of scans) and spatial resolution was necessary. Of necessity, it was decided to have two scan rates, a search mode of 1 deg/sec and a data mode of 0.1 deg/sec, the latter corresponding to a little less than one beamwidth per time constant. Planetary readings were spaced approximately one beamwidth apart. The 1 deg/sec rate was a compromise between the desired goal of obtaining data pertaining to the anti-subsolar point, the instrument response, and the sampling logic.

In order to arrive at the scan trigger voltage levels that would be best adapted to the output of the instrument (considering the noise level, response time, and sensitivity of the instrument), assumed antenna efficiencies, planet temperatures, etc., were used to estimate the resulting output voltages.

Two voltage levels were of interest. That nearest the zero-input baseline level (chosen to be 1 v) was the level that had to be attained in order to change the scanning rate from the search mode of 1 deg/sec to the data mode of 0.1 deg/sec. A higher level had to be exceeded in order to "arm" the scan reversal logic. After certain portions of the scan circuitry had been "armed," six consecutive readings below the first trigger voltage level were sufficient to cause the scanning direction to be changed. As the radiometer beams came back onto the planet, the level would rise again, "re-arming" the scan reversal circuitry.

The choice of the trigger level had to be a compromise between output noise level and the expected duration of time that the output signal was above this during a fast-scan passage across the disc of the planet. Unfortunately, it was necessary that this be the case because the radiometer outputs controlled the scan logic only at the radiometer data sampling times, making the baseline stability, noise level, and sensitivity of the instrument very critical.

If for any reason both radiometer outputs were to remain below 1.5 v for 150–160 sec or longer, the fast-scan mode would be initiated and the internal calibration noise tube activated for 120 sec. During this calibration period, the scan logic would prevent the system from going automatically into the slow-scan mode. This re-initiation of the search mode was to insure that as little data time as possible be lost if a large burst of noise accidentally triggered the slow-scan mode prior to actual

acquisition of the planet. Without this feature, the system would go into slow scan and stay there after a single data point exceeding 1.5 v. It will be noted later that it was the combination of the fast-scan search mode and the fact that the noise tube did not fire that resulted in the scan across the sunlit portion of the planet, without which very little in the way of conclusions regarding models for the planet could have been made.

In order to estimate the probable output levels that would occur during the search mode, the voltage into the integrator was assumed to have a trapezoidal waveform having slopes compatible with the probable drift scans for the assumed antenna pattern. The time base of these waveforms was compatible with the scan rate of 1 deg/sec and the assumed angular size of the planet. The brightness temperatures assumed for the planet were in the vicinity of 250 to 400°K for 13.5 mm and between 400 and 600°K for 19 mm.

The output response of an RC integrator to such a waveform can be easily shown to be

$$V(t) = \frac{V_0}{t_0}\left\{\left[t - RC\left(1 - e^{-\frac{t}{RC}}\right)\right]U(t) - \left[(t - t_0 - RC\left(1 - e^{-\frac{t-t_0}{RC}}\right)\right]U(t - t_0) - \left[t-T+t_0)-RC\left(1 - e^{-\frac{t-T+t_0}{RC}}\right)\right]U(t-T+t_0) + \left[(t - T) - RC\left(1 - e^{-\frac{t-T}{RC}}\right)\right]U(t - T)\right\} \quad (2)$$

where $U(t)$ = the Heaviside function

V_0 = peak value of the trapezoidal voltage

t_0 = time to increase from $V = 0$ to $V = V_0$

T = total waveform time base

The value of V_0, of course, would be given ideally by (see Section III)

$$V_0 = \frac{\alpha G_0}{4\pi}\int_{\Omega_V} T_V(\theta, \phi)\, F(\theta, \phi)\, d\Omega \quad (3)$$

and (see Appendix A) where we write $V(t)$ for $x(t)$ and V_0 for $y(t)$,

$$V(t) = \int_0^t V_0(t - \tau)\frac{e^{-\frac{\tau}{RC}}}{RC}\, d\tau \quad (4)$$

However, to estimate V_0, the equation used was

$$V_0 = \frac{\alpha G_0 T_V}{4\pi}\int_{\Omega_V} F(\theta, \phi)\, d\Omega \quad (5)$$

The value of $(G_0/4\pi)\int_{\Omega_V} F(\theta, \phi)\, d\Omega$ for the center of the planet was assumed to be ~ 0.65 for both channels. With $\alpha \sim 1$ v/200°K (antenna temperature), this resulted in $V_0 \sim T_V/307$ v. At 19 mm, this gave an estimated range for V_0 of 1.3 to 1.95 v, and at 13.5 mm, of 0.8 to 1.3 v. For a 20-sec time constant, this meant that for a 400°K planet at both 13.5 and 19 mm and for a trigger level of 0.5 v above the baseline, only after the scan plane had crossed to about an s/R_p value of ~ 0.4 would the output level be such that the planet would be acquired with 100% probability.[1]

After the instruments were built and tested, it was found that the antenna diplexer units were effectively far less efficient than had been previously assumed. To offset this factor, it was necessary to increase the electronic gain. Of course the noise level was increased, and the baseline drift with temperature was more apparent.

The radiometer flown to Venus had such a resultant sensitivity at launch that if it were looking at a "black" disc subtending 13 deg, the output would indicate 1 v for a disc temperature of 254°K on channel 1 and for a disc temperature of 279°K on channel 2[2]. This was the projected sensitivity at the planet under the predicted operating temperature environment. Hence, for a 500°K planet at 19 mm, the value of V_0 for channel 1 would have been 2.0 v, and for 400°K at 13.5 mm, V_0 would have been $\sim$1.43 v. With this sensitivity, there was a probability of 1.0 that the planet would be acquired by the time s/R_p had decreased to 0.7.

Of the available voltage levels, a compromise value of 1.25 v above the baseline level was chosen for the scan reversal circuitry. This level would be exceeded when the scan plane was at a dark-side s/R_p value of 0.9 for a 500°K planet on channel 1 and at a dark-side s/R_p value of 0.8 for a 400°K planet on channel 2.

The number of scans that would have been obtained had the equipment not suffered such large changes in baseline level and sensitivity would depend upon the size of the planetary disc at the time of passage and

[1] See Fig. 15.

[2] See Table 4.

particularly on how soon the planet was "acquired" by the radiometer. For the actual miss distance that occurred, assuming the planet to be acquired toward the beginning of the $s/R_p = 0.9$ scan, the number of scans would have been ~13 (this includes time spent off the planet during scan reversal).

III. PREFLIGHT CALIBRATIONS

The primary calibration used an absorber disc at ambient temperature. A secondary calibration was also performed just prior to launch, using a noise tube radiator. On–off measurements of the Sun were also made. This Section discusses each of these measurements.

A. The Absorber Disc Calibration

In the past, the calibration of Earth-based radio telescopes has been fairly straightforward, consisting of the determination of the on-axis gain G_0 and the antenna pattern $F(\theta, \phi)$. One then determines the brightness temperature T_B of the planet by measuring its antenna temperature ΔT_A and solving the equation

$$\Delta T_A = \frac{1}{4\pi}\int_\Omega G(\theta, \phi)\ T(\theta, \phi)\ d\Omega$$

$$= \frac{G_0}{4\pi}\int_\Omega F(\theta, \phi)\ T(\theta, \phi)\ d\Omega \qquad (6)$$

for $T_B(\theta, \phi)$ In the case of a microwave radiometer that has a very broad RF bandwidth the problem is not quite so simple. One is faced with two additional factors: the variation in on-axis gain with frequency (which may or may not exhibit resonance effects) and the RF bandwidths of the various parts of the system must be considered. In general, radiometers utilize the comparatively narrow band character of the IF strip as the band-limiting device, and, because of this, the relative bandwidths of the main feed diplexer, reference horn, and ferrite switch parts are not required to be known. However, this was not the case for the type of radiometer used for the *Mariner* experiment since there was no IF strip and all RF bandwidths were made as wide as possible to increase the sensitivity of the instrument.

Measurements of gain vs frequency were made on the antenna and diplexer units for serial numbers 3 and 4 (Ref. 18). In the RF passband of the diplexer it was noted that the antenna gain varied appreciably and the two units measured differed markedly in RF bandwidth. The difficulties involved in interpreting the measured gains in terms of a temperature measurement of Venus were obvious.

A means of measuring the required instrument characteristics by using a broad band noise source was devised. This involved scanning the radiometer from cold sky to a disc of material at ambient temperature that had a reflectivity of zero and an emissivity of one (to within 1%).

At the frequency ν, the received power at the detector (including the polarization factor of ½) due to a source of brightness temperature $T_B(\theta,\phi,\nu)$ is

$$P^* = \frac{k}{c^2}\int_\Omega \int_{\Delta\nu} T_B(\theta,\phi,\nu)\nu^2\, A(\theta,\phi,\nu)\, d\nu\, d\Omega \qquad (7)$$

where k is Boltzmann's constant and and c is the velocity of light. Now the effective area of the antenna $A(\theta, \phi, \nu)$ is related to the antenna gain through (Ref. 19):

$$A(\theta,\phi,\nu) = \frac{G(\theta,\phi,\nu)c^2}{4\pi\nu^2} \qquad (8)$$

Hence

$$P^* = \frac{k}{4\pi}\int_\Omega \int_{\Delta\nu} T(\theta,\phi,\nu)\, G(\theta,\phi,\nu)\, d\nu\, d\Omega \qquad (9)$$

Since

$$F(\theta,\phi,\nu) = \frac{A(\theta,\phi,\nu)}{A_0(\nu)} = \frac{G(\theta,\phi,\nu)}{G_0(\nu)}$$

one obtains

$$P^* = \frac{k}{4\pi}\int_\Omega \int_{\Delta\nu} T(\theta,\phi,\nu)\, G_0(\nu)\, F(\theta,\phi,\nu)\, d\nu\, d\Omega \qquad (10)$$

Consider the signal obtained when one looks from cold sky to a disc absorber of known subtended angle and temperature. Without the disc,

$$\begin{aligned} P_1^* = \frac{k}{4\pi}\Bigg\{ &\int_{\Omega_D}\int_{\Delta\nu} T_{\text{sky}}(\theta,\phi,\nu)\, G_0(\nu)\, F(\theta,\phi,\nu)\, d\nu\, d\Omega \\ &+ \int_{\Omega_{\text{sky}}-\Omega_D}\int_{\Delta\nu} T_{\text{sky}}(\theta,\phi,\nu)\, G_0(\nu)\, F(\theta,\phi,\nu)\, d\nu\, d\Omega \\ &+ \int_{4\pi-\Omega_{\text{sky}}}\int_{\Delta\nu} T_{\text{gnd}}(\theta,\phi,\nu)\, G_0(\nu)\, F(\theta,\phi,\nu)\, d\nu\, d\Omega \\ &\text{plus instrument radiation terms}\Bigg\} \end{aligned} \qquad (11)$$

With the disc subtending the solid angle Ω_D,

$$\begin{aligned} P_2^* = \frac{k}{4\pi}\Bigg\{ &T_D\int_{\Omega_D}\int_{\Delta\nu} G_0(\nu)\, F(\theta,\phi,\nu)\, d\nu\, d\Omega \\ &+ \int_{\Omega_{\text{sky}}-\Omega_D}\int_{\Delta\nu} T_{\text{sky}}(\theta,\phi,\nu)\, G_0(\nu)\, F(\theta,\phi,\nu)\, d\nu\, d\Omega \\ &+ \int_{4\pi-\Omega_{\text{sky}}}\int_{\Delta\nu} T_{\text{gnd}}(\theta,\phi,\nu)\, G_0(\nu)\, F(\theta,\phi\nu)\, d\nu\, d\Omega \\ &\text{plus instrument radiation terms}\Bigg\} \end{aligned} \qquad (12)$$

The difference ΔP_D is then

$$\Delta P_D^* = \frac{k}{4\pi}\int_{\Omega_D}\int_{\Delta\nu}\left[T_D - T_{\text{sky}}(\theta,\phi,\nu)\right] G_0(\nu)\, F(\theta,\phi,\nu)\, d\nu\, d\Omega \qquad (13)$$

At the planet, the instrument looks at cold space and then at the planet, resulting in a ΔP_V^* given by

$$\Delta P_V^* = \frac{k}{4\pi} \times\int_{\Omega_V}\int_{\Delta\nu}\left[T_V(\theta,\phi,\nu) - T_{\text{space}}(\theta,\phi,\nu)\right] G_0(\nu)\, F(\theta,\phi,\nu)\, d\nu\, d\Omega \qquad (14)$$

In order to insure the absoluteness of the calibration, an internal noise source in the form of a gas discharge tube was incorporated in the instrument. This was energized during the absorber disc calibrations and at various times throughout the mission as outlined in Section IV. Denoting the effective antenna temperature of the calibration signal by T_{cal}, we have

$$\Delta P_{\text{cal}} = kT_{\text{cal}}\,\Delta\nu_{\text{cal}} \qquad (15)$$

Designating β as the ratio of the absorber disc deflection to that of the internal noise tube, we have

$$\beta_D = \frac{\int_{\Omega_D}\int_{\Delta\nu}\left[T_D - T_{\text{sky}}(\theta,\phi,\nu)\right] G_0(\nu)\, F(\theta,\phi,\nu)\, d\nu\, d\Omega}{4\pi T_{\text{cal}}\,\Delta\nu_{\text{cal}}} \qquad (16)$$

Similarly, for the planet,

$$\beta_V = \frac{\int_{\Omega_V}\int_{\Delta\nu}\left[T_V(\theta,\phi,\nu) - T_{\text{space}}(\theta,\phi,\nu)\right] G_0(\nu)\, F(\theta,\phi,\nu)\, d\nu\, d\Omega}{4\pi T_{\text{cal}}\,\Delta\nu_{\text{cal}}} \qquad (17)$$

The β_D values for the instrument flown to Venus were 0.174 ±0.015 PE and 0.340 ±0.024 PE for the 19- and 13.5-mm channels respectively and include two noise tube changes and a diplexer modification. (Note that what is measured is a voltage deflection.) The relationship between the power detected at the crystal and the output voltage is dependent upon the characteristics of the amplifiers, etc., at the time of the measurement. However, this applies to both the noise tube signal and the disc or planet

signals. By taking ratios, this factor cancels out. Denoting $\gamma = \beta_V/\beta_D$, we have

$$\int_{\Omega_V}\int_{\Delta\nu}\left[T_V(\theta,\phi,\nu) - T_{\text{space}}(\theta,\phi,\nu)\right] G_0(\nu)\, F(\theta,\phi,\nu)\, d\nu\, d\Omega = \gamma \int_{\Omega_D}\int_{\Delta\nu}\left[T_D - T_{\text{sky}}(\theta,\phi,\nu)\right] G_0(\nu)\, F(\theta,\phi,\nu)\, d\nu\, d\Omega \tag{18}$$

If one assumes that the bracketed expressions can be replaced by T'_V and T'_D respectively, and further, that the integration over ν results in some G_0, $F(\theta,\phi)$, and frequency-averaged temperatures, there results simply

$$T'_V = \gamma\, T'_D \frac{\int_{\Omega_D} \overline{F(\theta,\phi)}\, d\Omega}{\int_{\Omega_V} \overline{F(\theta,\phi)}\, d\Omega} \tag{19}$$

The results of the experiment that have been published so far used the simple expression in Eq. (19). The antenna pattern $F(\theta,\phi)$ used was that measured at center frequency for each of the two channels.

Although only an E-plane antenna pattern was measured for serial 3, the instrument that was flown to Venus, the eccentricity of the pattern could not have departed significantly from those of serial 2 and 4, and these were found to have an eccentricity of less than 0.24, or a semi-major to semi-minor axis ratio of less than 1.031. The dependence of the antenna pattern on ϕ was therefore neglected.

The tests were performed on top of Table Mountain at an altitude of about 2.5 km under conditions of very low relative humidity so that atmospheric radiation, mainly from water vapor, was small. Table Mountain is located near Wrightwood, California, at the edge of the Mojave Desert.

The absorber disc used for the primary calibrations was 10 ft in diameter and made of plywood covered with a ¼-in. sheet of microwave-absorbent material. The disc was suspended 44 ft above the radiometer so that it subtended an angle of 13 deg. The reference horns were terminated with microwave absorber to insure that no ground radiation could enter the reference horns because of any movement of the radiometers during the disc deflection measurements. It was necessary that the radiometer be pointed alternately at the sky and the disc by moving the radiometer through an angle of about 20 deg, instead of ideally keeping the radiometer fixed and moving the disc in and out of the radiometer beam. Moving the radiometer axis 20 deg off the center of the disc caused a disc side lobe contribution of less than a computed 0.5% of the on-axis deflection. This also kept the main lobe more than 40 deg away from any trees in the vicinity of the test site.

Because of the nature of the source, no near field correction to the absorber disc deflections has been included. The fact that the disc was so nearly a perfect absorber would make such a correction negligible.

An estimate of the error resulting from neglecting the frequency dependence of $G_0(\nu)$ and $F(\theta,\phi,\nu)$ was obtained by numerically computing and comparing the factors in Eqs. (18) and (19) above. For ease of computation, an attempt was made to find a simple mathematical expression that would fit the antenna pattern fairly well, resulting in the expression

$$F(\theta) \sim \frac{\sin^2 \pi b\, \nu\theta}{(\pi b\, \nu\theta)^2} \tag{20}$$

For $G_0(\nu)$, a tabulated set of values was used that was obtained by plotting a smooth extrapolated curve through the measured points. The values used are seen in Table 1.

Table 1. On-axis gain G_0 vs frequency ν

Channel 1		Channel 2	
ν, cps	$G_0(\nu)$	ν, cps	$G_0(\nu)$
15.00×10^9	1260	21.10×10^9	2830
15.10	1300	21.20	3430
15.20	1650	21.30	3830
15.30	2060	21.40	4070
15.40	2420	21.50	4220
15.50	2620	21.60	4330
15.60	2760	21.70	4380
15.70	2840	21.80	4340
15.80	2884	21.90	4240
15.90	2860	22.00	4190
16.00	2770	22.10	4150
16.10	2600	22.20	4170
16.20	2360	22.30	4200
16.30	2240	22.40	4240
16.40	2160	22.50	4300
16.50	2100	22.60	4380
16.60	2060	22.70	4480
		22.80	4590
		22.90	4700
		23.00	4820
		23.10	4910
		23.20	5000
		23.30	4920

Values for γ corresponding to three different assumptions regarding the frequency dependence of the factors T, F, and G_0 were computed. For both γ_1 and γ_2, the frequency dependence of T is neglected; in the case of γ_1, the frequency dependence of G_0 and F is not neglected, while in the case of γ_2 it is. The expressions for γ_1 and γ_2 are

$$\gamma_1 = \left(\frac{T'_V}{T'_D}\right) \frac{\int_{\Omega_V}\int_{\Delta\nu} G_0(\nu)\sin^2 \pi b\,\nu\theta/(\pi b\,\nu\theta)^2\, d\nu\, d\Omega}{\int_{\Omega_D}\int_{\Delta\nu} G_0(\nu)\sin^2 \pi b\,\nu\theta/(\pi b\,\nu\theta)^2\, d\nu\, d\Omega} \tag{21}$$

and

$$\gamma_2 = \left(\frac{T'_V}{T'_D}\right) \frac{\int_{\Omega_V} \sin^2 \pi b\,\nu_0\theta/(\pi b\,\nu_0\theta)^2\, d\nu\, d\Omega}{\int_{\Omega_D} \sin^2 \pi b\,\nu_0\theta/(\pi b\,\nu_0\theta)^2\, d\nu\, d\Omega} \tag{22}$$

In γ_3 and γ_4, allowance is made for the fact that T'_V is frequency-dependent. The expressions for γ_3 and γ_4 are (with $k^* = \Delta T/\Delta\nu$)

$$\gamma_3 = \frac{\int_{\Omega_V}\int_{\Delta\nu} [T_0 - k^*(\nu - \nu_0)]\, G_0(\nu)\sin^2 \pi b\,\nu\theta/(\pi b\,\nu\theta)^2\, d\nu\, d\Omega}{T'_D\int_{\Omega_D}\int_{\Delta\nu} G_0(\nu)\sin^2 \pi b\,\nu\theta/(\pi b\,\nu\theta)^2\, d\nu\, d\Omega} \tag{23}$$

$$\gamma_4 = \frac{\int_{\Omega_V}\int_{\Delta\nu} G_0(\nu)[T_0 + k^*(\nu - \nu_0)]\sin^2 \pi b\,\nu\theta/\pi b\,\nu\theta)^2\, d\nu\, d\Omega}{T'_D\int_{\Omega_D}\int_{\Delta\nu} G_0(\nu)\sin^2 \pi b\,\nu\theta/(\pi b\,\nu\theta)^2\, d\nu\, d\Omega} \tag{24}$$

The dependence of temperature on frequency as indicated in γ_3 is the more probable of the two. However, γ_4 was

Table 2. Frequency-averaged antenna pattern $\overline{F(\theta)}$ vs θ for channel 1

θ, deg	$F(\theta)$	θ, deg	$F(\theta)$	θ, deg	$F(\theta)$	θ, deg	$F(\theta)$	θ, deg	$F(\theta)$
0.0	1.0000	3.0	0.00375	6.0	0.00099	9.0	0.00255	12.0	0.00183
0.1	0.9980	3.1	0.00218	6.1	0.00100	9.1	0.00248	12.1	0.00168
0.2	0.9900	3.2	0.00128	6.2	0.00102	9.2	0.00243	12.2	0.00152
0.3	0.9750	3.3	0.00198	6.3	0.00104	9.3	0.00240	12.3	0.00144
0.4	0.9600	3.4	0.00268	6.4	0.00106	9.4	0.00235	12.4	0.00140
0.5	0.9350	3.5	0.00355	6.5	0.00110	9.5	0.00230	12.5	0.00140
0.6	0.9000	3.6	0.00438	6.6	0.00114	9.6	0.00225	12.6	0.00143
0.7	0.8650	3.7	0.00470	6.7	0.00117	9.7	0.00215	12.7	0.00149
0.8	0.8170	3.8	0.00540	6.8	0.00125	9.8	0.00200	12.8	0.00152
0.9	0.7650	3.9	0.00565	6.9	0.00134	9.9	0.00188	12.9	0.00153
1.0	0.7090	4.0	0.00570	7.0	0.00144	10.0	0.00180	13.0	0.00148
1.1	0.6390	4.1	0.00552	7.1	0.00159	10.1	0.00180	13.1	0.00137
1.2	0.5780	4.2	0.00520	7.2	0.00178	10.2	0.00183	13.2	0.00122
1.3	0.5150	4.3	0.00480	7.3	0.00205	10.3	0.00188	13.3	0.00110
1.4	0.4550	4.4	0.00433	7.4	0.00239	10.4	0.00198	13.4	0.00102
1.5	0.3990	4.5	0.00375	7.5	0.00278	10.5	0.00208	13.5	0.00095
1.6	0.3480	4.6	0.00315	7.6	0.00316	10.6	0.00220	13.6	0.00089
1.7	0.3000	4.7	0.00267	7.7	0.00353	10.7	0.00230	13.7	0.00085
1.8	0.2500	4.8	0.00212	7.8	0.00390	10.8	0.00240	13.8	0.00082
1.9	0.2040	4.9	0.00170	7.9	0.00416	10.9	0.00243	13.9	0.00079
2.0	0.1650	5.0	0.00146	8.0	0.00434	11.0	0.00244	14.0	0.00078
2.1	0.1300	5.1	0.00133	8.1	0.00465	11.1	0.00243	14.1	0.00075
2.2	0.0980	5.2	0.00116	8.2	0.00455	11.2	0.00241	14.2	0.00078
2.3	0.0725	5.3	0.00107	8.3	0.00442	11.3	0.00238	14.3	0.00079
2.4	0.0515	5.4	0.00104	8.4	0.00420	11.4	0.00235	14.4	0.00080
2.5	0.03565	5.5	0.00102	8.5	0.00385	11.5	0.00230	14.5	0.00081
2.6	0.02415	5.6	0.00099	8.6	0.00350	11.6	0.00224	14.6	0.00082
2.7	0.01640	5.7	0.00098	8.7	0.00318	11.7	0.00218	14.7	0.00082
2.8	0.01025	5.8	0.00098	8.8	0.00286	11.8	0.00210	etc.	
2.9	0.00625	5.9	0.00098	8.9	0.00268	11.9	0.00198		

Table 3. Frequency-averaged antenna pattern $\overline{F(\theta)}$ vs θ for channel 2

θ, deg	$F(\theta)$	θ, deg	$F(\theta)$	θ, deg	$F(\theta)$	θ, deg	$F(\theta)$	θ, deg	$F(\theta)$
0.0	1.00000	3.0	0.00178	6.0	0.00252	9.0	0.00213	12.0	0.00230
0.1	0.99750	3.1	0.00238	6.1	0.00274	9.1	0.00198	12.1	0.00229
0.2	0.98750	3.2	0.00239	6.2	0.00290	9.2	0.00188	12.2	0.00228
0.3	0.97000	3.3	0.00314	6.3	0.00306	9.3	0.00180	12.3	0.00225
0.4	0.94500	3.4	0.00328	6.4	0.00320	9.4	0.00173	12.4	0.00222
0.5	0.90750	3.5	0.00328	6.5	0.00334	9.5	0.00168	12.5	0.00218
0.6	0.86000	3.6	0.00313	6.6	0.00349	9.6	0.00164	12.6	0.00212
0.7	0.79500	3.7	0.00292	6.7	0.00361	9.7	0.00162	12.7	0.00203
0.8	0.72500	3.8	0.00262	6.8	0.00374	9.8	0.00161	12.8	0.00193
0.9	0.65000	3.9	0.00239	6.9	0.00385	9.9	0.00160	12.9	0.00180
1.0	0.57750	4.0	0.00214	7.0	0.00399	10.0	0.00162	13.0	0.00150
1.1	0.50000	4.1	0.00190	7.1	0.00412	10.1	0.00164	13.1	0.00140
1.2	0.43500	4.2	0.00164	7.2	0.00422	10.2	0.00170	13.2	0.00134
1.3	0.36750	4.3	0.00150	7.3	0.00428	10.3	0.00174	13.3	0.00129
1.4	0.30750	4.4	0.00138	7.4	0.00430	10.4	0.00178	13.4	0.00126
1.5	0.25000	4.5	0.00128	7.5	0.00432	10.5	0.00184	13.5	0.00124
1.6	0.19250	4.6	0.00123	7.6	0.00432	10.6	0.00189	13.6	0.00123
1.7	0.15000	4.7	0.00122	7.7	0.00431	10.7	0.00193	13.7	0.00124
1.8	0.11250	4.8	0.00122	7.8	0.00430	10.8	0.00198	13.8	0.00125
1.9	0.08500	4.9	0.00121	7.9	0.00424	10.9	0.00202	13.9	0.00126
2.0	0.06000	5.0	0.00132	8.0	0.00414	11.0	0.00207	14.0	0.00127
2.1	0.03950	5.1	0.00139	8.1	0.00412	11.1	0.00211	14.1	0.00128
2.2	0.02600	5.2	0.00146	8.2	0.00398	11.2	0.00213	14.2	0.00128
2.3	0.01575	5.3	0.00154	8.3	0.00375	11.3	0.00218	14.3	0.00128
2.4	0.00825	5.4	0.00164	8.4	0.00355	11.4	0.00221	14.4	0.00127
2.5	0.00335	5.5	0.00174	8.5	0.00330	11.5	0.00224	14.5	0.00126
2.6	0.00152	5.6	0.00186	8.6	0.00305	11.6	0.00228	14.6	0.00125
2.7	0.00130	5.7	0.00200	8.7	0.00280	11.7	0.00229	14.7	0.00124
2.8	0.00128	5.8	0.00216	8.8	0.00255	11.8	0.00231	etc.	
2.9	0.00140	5.9	0.00234	8.9	0.00235	11.9	0.00230		

computed to see how sensitive the result is to the frequency dependence of the temperature (along with γ_1).

Since the only contribution to the frequency of T'_D is through T_{sky}, which is very small compared with T_D, the frequency dependence of T'_D has been neglected in γ_3. Computed values of γ_1 through γ_4 show that they differ by no more than 0.2%. Hence the assumptions leading to Eq. (19) will introduce an error considerably smaller than the probable error attached to the measurement of the β ratios.

As indicated in the discussion of primary calibration in the Data Reduction and Analysis Section, a measurement of the antenna pattern was necessary. This was done at midfrequency for each channel, or at 15.8 and 22.2 Gc. The resultant pattern is shown on a plot of log power vs angle in Fig. 4 and is tabulated in Tables 2 and 3 for computational purposes. The 3-db beamwidths were 2.64 and 2.2 deg for channels 1 and 2 respectively. The angular deviations of the radiometer beams with respect to the mechanical axis of the dish were as follows:

Channel	Angular deviation, deg	
1	Azimuth	0.0
	Elevation	0.0
2	Azimuth	−0.2
	Elevation	0.0

The scan axis of the radiometer is vertical, the reference horns are at the top, and counterclockwise is considered positive.

As a part of the calibration procedure, the overall linearity of the radiometer was measured by injecting noise into the radiometer at the main RF feed in a number of discrete increments utilizing a precision attenuator. The full-scale linearity was measured to be better than 2%.

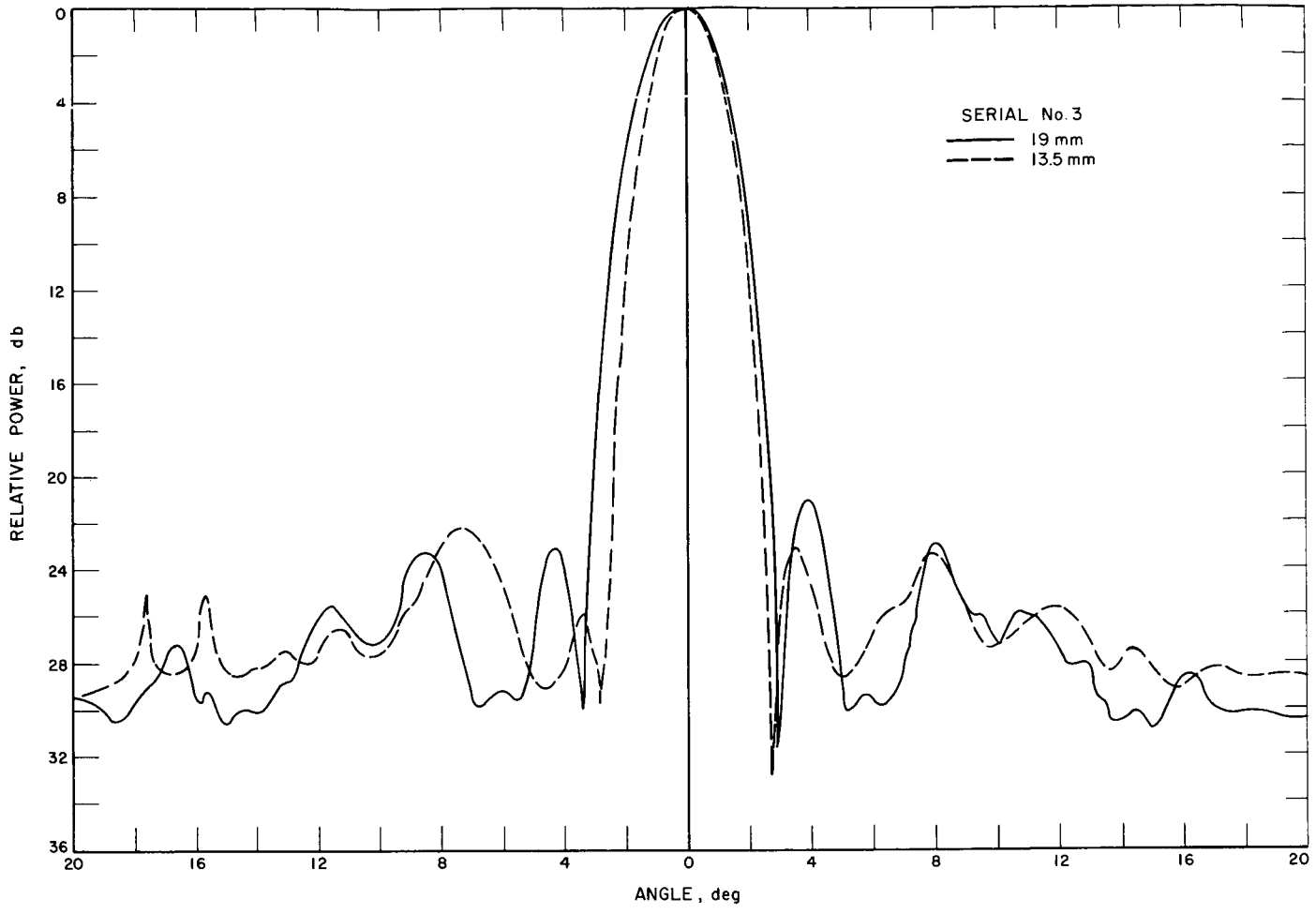

Fig. 4. *E*-plane antenna patterns

B. Secondary Calibration

Primarily as a precautionary measure, a series of correlating RF gain measurements on the radiometers was conducted at the Jet Propulsion Laboratory (JPL) facility at Cape Kennedy. Instrument failure was a possibility that had always to be considered, and, because of the tightness of the schedule, etc., it was felt that a secondary calibration that included the diplexer and antenna gain characteristics should be developed for use at the Cape. Under the constraints imposed, the best that could be utilized was a noise radiometer measurement that was conducted in the spacecraft hangar. Briefly, the measurement consisted of the response of the radiometer to a wide-band noise signal fed into a standard gain horn, the radiating system located as far away as possible, compatible with signal-to-noise and building constraints. The resulting deflection was compared with the internal calibration signal.

Let us consider two radiometers having had the primary absorber disc calibration performed. The resulting deflections are [assuming G_0 and $F(\theta, \phi)$ as in the case leading to Eq. (19)]

$$D_1 = \frac{\alpha_1 \overline{G_{0_1}}\, T_D \Delta\nu_1}{4\pi} \int_{\Omega_D} \overline{F_1(\theta, \phi)}\, d\Omega \tag{25}$$

and

$$D_2 = \frac{\alpha_2 \overline{G_{0_2}}\, T_D \Delta\nu^2}{4\pi} \int_{\Omega_D} \overline{F_2(\theta, \phi)}\, d\Omega \tag{26}$$

Defining β as before, there results

$$\beta_1 = \frac{\overline{G_{0_1}} T_D}{4\pi\, T_{\text{cal}_1}} \left(\frac{\Delta\nu}{\Delta\nu_{\text{cal}}}\right)_1 \int_{\Omega_D} \overline{F_1(\theta, \phi)}\, d\Omega \tag{27}$$

(as before, α_1 and α_2 relate voltage deflection to antenna temperature for the two radiometers being considered)

and

$$\beta_2 = \frac{\overline{G_{0_2}}\, T_D}{4\pi\, T_{\mathrm{cal}_2}} \left(\frac{\Delta\nu}{\Delta\nu_{\mathrm{cal}}}\right)_2 \int_{\Omega_D} \overline{F_2(\theta, \phi)}\, d\Omega \tag{28}$$

Then

$$\gamma_{12} = \frac{T_{\mathrm{cal}_2}\, \overline{G_{0_1}} \left(\frac{\Delta\nu}{\Delta\nu_{\mathrm{cal}}}\right)_1 \int_{\Omega_D} \overline{F_1(\theta, \phi)}\, d\Omega}{T_{\mathrm{cal}_1}\, G_{0_2} \left(\frac{\Delta\nu}{\Delta\nu_{\mathrm{cal}}}\right)_2 \int_{\Omega_D} \overline{F_2(\theta, \phi)}\, d\Omega} \tag{29}$$

The response of the radiometers, when illuminated by the noise radiator, will be

$$D_1' = \alpha_1\, kT_N\, \Delta\nu_1\, \overline{G_{0_1}}\, \eta(R, \lambda)\chi(\lambda) \int_{\Omega_N} \overline{F_1(\theta, \phi)}\, d\Omega \tag{30}$$

and

$$D_2' = \alpha_2\, kT_N\, \Delta\nu_2\, \overline{G_{0_2}}\, \eta(R, \lambda)\chi(\lambda) \int_{\Omega_N} \overline{F_2(\theta, \phi)}\, d\Omega \tag{31}$$

where $\eta(R, \lambda)$ is the near field correction factor and $\chi(\lambda)$ the noise tube–standard gain horn coupling factor. Taking the ratio of D_1' to the corresponding internal noise calibration deflection, etc., resulting in β_1' and β_2', and forming the ratio β_1'/β_2', we obtain

$$\frac{\beta_1'}{\beta_2'} = \gamma_{12}' = \frac{\overline{G_{0_1}}}{\overline{G_{0_2}}} \frac{(\Delta\nu/\Delta\nu_{\mathrm{cal}})_1}{(\Delta\nu/\Delta\nu_{\mathrm{cal}})_2} \frac{T_{\mathrm{cal}_2}}{T_{\mathrm{cal}_1}} \frac{\int_{\Omega_N} \overline{F_1(\theta, \phi)}\, d\Omega}{\int_{\Omega_N} \overline{F_2(\theta, \phi)}\, d\Omega} \tag{32}$$

Comparing γ_{12}' and γ_{12}, we find

$$\gamma_{12} = \gamma_{12}' \frac{\int_{\Omega_D} \overline{F_1}(\theta, \phi)\, d\Omega \Big/ \int_{\Omega_N} \overline{F_1(\theta, \phi)}\, d\Omega}{\int_{\Omega_D} \overline{F_2}(\theta, \phi)\, d\Omega \Big/ \int_{\Omega_N} \overline{F_2(\theta, \phi)}\, d\Omega} \tag{33}$$

The ratio term multiplying γ_{12}' for serial 3 and serial 2 was found to be essentially unity to within 2%.

For the noise radiator tests, the radiometer and noise radiator were optically aligned to within 0.1 deg in angle and to within $\pm\frac{1}{8}$ in. in distance. All measurements were made in the solar panel storage area of the JPL spacecraft hangar. Tests involving the placement of absorbing or reflecting material at various locations on the floor and within about 6 ft of the boresight axis showed undetectable level changes. The tests were all conducted within ± 2 in. of a standard test area.

C. On–Off Measurements of the Sun

On–off measurements of the Sun were taken at Table Mountain on May 18, 1962, to check on the overall calibration procedure. The results of several on–off measurements gave

$$(\beta_{\mathrm{Sun}})_{13.5\ \mathrm{mm}} = 0.423 \pm 0.017$$

$$(\beta_{\mathrm{Sun}})_{19\ \mathrm{mm}} = 0.185 \pm 0.005$$

Since two noise tube changes were incorporated in the unit after May 18, the β values must be multiplied by 1.115 and 0.966 respectively,

$$(\beta_{\mathrm{Sun}})'_{13.5\ \mathrm{mm}} = 0.471 \pm 0.019$$

$$(\beta_{\mathrm{Sun}})'_{19\ \mathrm{mm}} = 0.179 \pm 0.006$$

Since

$$T_{\mathrm{Sun}} = \frac{\beta_{\mathrm{Sun}}}{\beta_{\mathrm{D}}} \frac{T_0 \int_{\Omega_D} F(\theta, \phi)\, d\Omega}{\Omega_{\mathrm{Sun}}}\, e^{\tau}\, \delta(\tau)$$

we get

$$(T_{\mathrm{Sun}})_{13.5\ \mathrm{mm}} = \frac{0.471}{0.340} \frac{(290)(1.566 \times 10^{-3})}{6.654 \times 10^{-5}}\, e^{0.03} \cdot \frac{280}{283}$$

$$= 9600 \pm 700^{\circ}\mathrm{K}$$

$$(T_{\mathrm{Sun}})_{19\ \mathrm{mm}} = \frac{0.179}{0.174} \frac{(290)(2.193 \times 10^{-3})}{6.654 \times 10^{-5}}\, e^{0.01}$$

$$= 10{,}000 \pm 1000^{\circ}\mathrm{K}$$

where the e^{τ} and $\delta(\tau)$ factors correct for atmospheric absorption and radiation.

The rms error quoted above is the result of the error in β_{Sun}, β_{D}, and the error associated with the measurement of the change in the internal calibration signal as a result of noise tube changes. These values compare favorably with measurements at other wavelengths, and particularly with the value of $8870 \pm 980^{\circ}$K at the 11.8-mm wavelength obtained by Staelin et al. (Ref. 20) later the same year.

IV. FLIGHT SEQUENCE

The flight sequence consisted of the cruise phase and the encounter phase. The radiometer operated in the cruise phase both before and after the encounter phase. The operational aspects of both phases are discussed in this Section.

A. The Cruise Phase

Pre-encounter operation of the instrument was to consist of simultaneously providing power to the radiometer and activating a calibration sequence consisting of having the noise tube on for six frames or about 222 sec and off for 222 sec. Three successive calibration sequences spaced 15.76 hr apart were to occur every 189.12 hr. These calibration sequences were to provide an engineering history of the behavior of the instrument's various parameters of interest. Certainly the extent of the partial failures actually exhibited by the instrument could not be foreseen, but the inclusion of the cruise calibration sequence allowed much greater confidence in the extrapolation of the calibration signal into the encounter phase, and particularly to the time when actual planetary data were being taken.

The prelaunch characteristics of the radiometer are presented in Table 4. At the first calibration sequence of the cruise phase, the baseline of channel 1 should have read about −4.82 v and that of channel 2, about −1.90 v at the corresponding ~30°F operating temperature. Both were to come very close to the desired +1.0-v value as a result of the expected increase in temperature.

A total of 24 noise tube calibrations occurred, 22 before planetary encounter and two after planetary passage. All of the usable calibration-on and calibration-off data are plotted in Fig. 5. It was immediately obvious that problems had developed in regard to channel 2, because the baseline level was more than 2.5 v higher than expected, although the magnitude of the calibration signal was close to the expected value. Subsequent calibrations showed a gradual decrease in baseline level and amplifier gain, and the extrapolation of this trend to encounter showed the sensitivity of this channel to be so marginal that not much information was to be expected.

At day 264 (September 21, 1962) there was an indicated nonstandard mode of operation in channel 1 as well, since the baseline was too high and the gain too low. Subsequently the baseline of channel 1 increased to about 2.0 v near day 300 (October 27, 1962) and remained near this value for the remainder of the flight. As seen in Fig. 5, the actual gain of channel 1 decreased to zero and then reversed polarity.

A nonstandard mode of operation exhibited by both channels was the change in postdetection time constant noted during flight. Channel 1, for example, indicated a time constant shortly after launch of 20 sec, which increased to about 60 sec near day 334 (November 28, 1962) and from there to about 40 sec at day 348 (December 14, 1962). Channel 2 also exhibited an increase in time constant. The calibration of day 348 indicated a value of 50 sec. Time constant values of 40 and 50 sec were used in the reduction of data for channels 1 and 2 respectively.

Table 4. Serial 3 prelaunch characteristics

Channel No.	ΔV_{disc}, v	ΔV_{cal}, v	ΔV_{pp}, v	$\Delta V_{pp}/\Delta V_{cal}$	Baseline set, v	$\Delta V_{110°F}/\Delta V_{75°F}$
1	1.1015	5.83	0.37	0.064	−3.54	1.13
2	1.085	3.15	0.40	0.127	−1.25	0.95

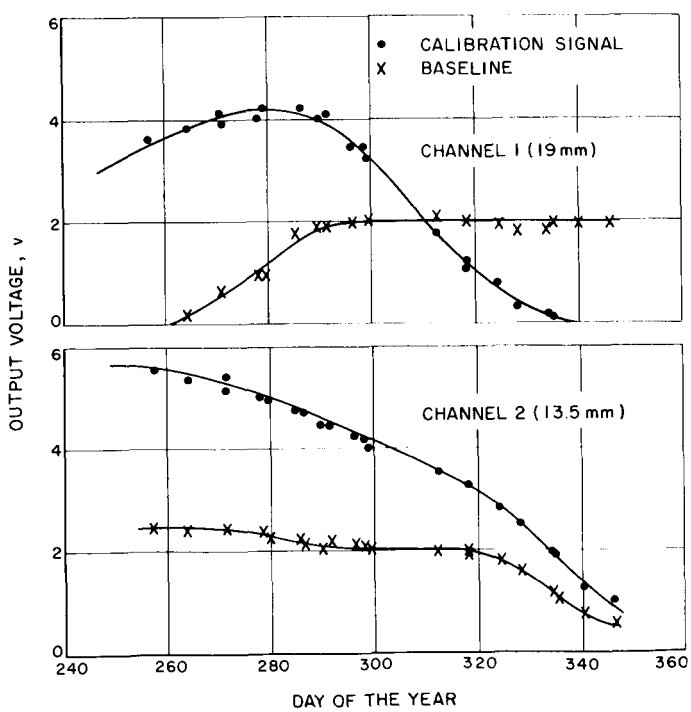

Fig. 5. Flight calibration history

B. The Encounter Phase

At about 13:38:46 GMT spacecraft time on December 14, 1962, the encounter mode of operation began, and the radiometer immediately started scanning at the slow 0.1-deg/sec rate as expected, since the baseline level of channel 1 was above the fast- to slow-scan trigger level. A further result of the baseline shift was the failure to obtain radiometer noise tube calibrations every 32.56 min before planet acquisition, as planned.

During the approximately 5½ hr before detection of the planet, approximately 15 complete 120-deg scans were obtained. This permitted a rather detailed study of the characteristics of the base line dependence on scan angle of each channel, as well as the noise characteristics of each. The details of the baseline variations are discussed in Section V.

Initial contact with Venus by the radiometer beams was made at 18:59 GMT spacecraft time. At that time, the spacecraft was about 46,800 km from the center of the planet. The location of the resulting scans is shown in Fig. 6. It can be seen that the juxtaposition on the planetary disc was ideal. In view of the difficulties with the baseline levels and their vital role in the scan logic, the positioning of the scans on the planet and the acquisition of the third scan were extremely fortunate.

The sequence of events leading to the obtaining of the third scan is rather remarkable. The fact that the phase reversal occurred in channel 1 resulted in the output level decreasing as the radiometer beams scanned the planet. Because the planet subtended ~16 deg, and because the second scan passed close to the optical terminator, the output level of channel 1 was 1.5 v or less for seven consecutive readings. Consequently, in combination with eight readings from channel 2 that were below 1.5 v, the minimum 15 consecutive low readings caused the fast-scan mode to be activated. The fast- to slow-scan logic circuitry was inhibited for the minimal three data lines but the noise tube did not fire. During prelaunch final systems test, the same malfunction occurred, but 73 consecutive subsequent runs produced no repeat of the failure. If the noise tube had fired for 2 min, it is doubtful that the third scan would have been obtained.

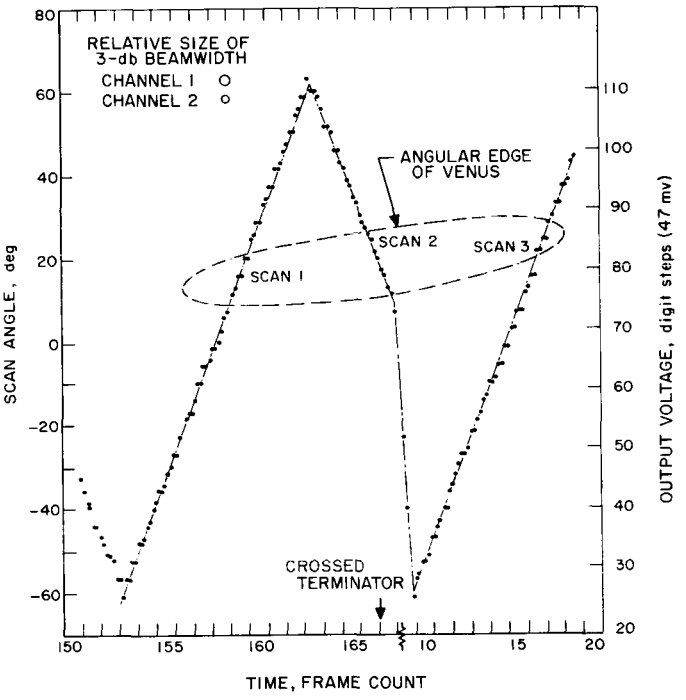

Fig. 6. Radiometer scan pattern during encounter

V. DATA REDUCTION AND ANALYSIS

The primary Venus data consisted of the pre-planet-baseline measurements, the planetary measurements, and the post-planet-calibration measurements. Reduction and analysis of the baseline data were necessary in order to determine the noise characteristics of the radiometer. The baseline level dependence upon scan angle and the magnitude and time constant of the calibration signals of both channels were required for the reduction of the planetary scan voltage waveforms. This Section discusses this portion of the experiment.

A. Baseline Averages and Radiometer Noise Level

As stated previously, for approximately 5½ hr before planetary detection, the radiometer was operating and scanning continuously. The data obtained were useful both in studying the baseline-vs-angle dependence that was found to exist and in determining the noise characteristics of the radiometer. The former was critical in the reduction of the channel 2 planet data.

Allowing about 5 min for warmup, baseline readings corresponding to each radiometer scan (RSC) reading were averaged, and the average deviation was computed at first with no regard for the scan direction (ascending or descending). The results are plotted in Figs. 7 and 8. Channel 1 is seen to show a definite increase in baseline level amounting to about 1.5 denary units or 0.07 v at the scan extreme. Between RSC readings of 35 and 95, the baseline was essentially constant.

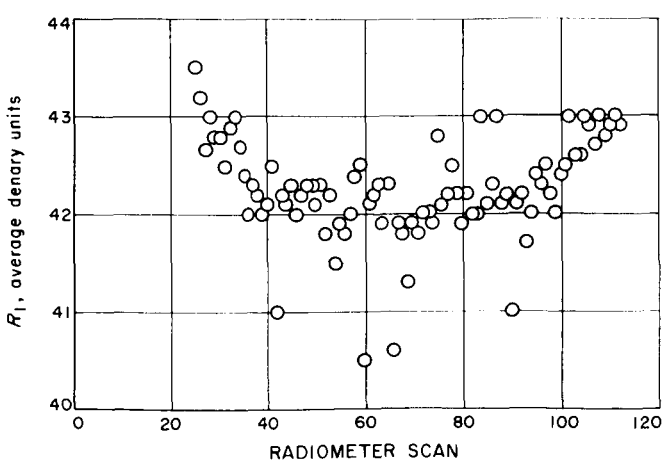

Fig. 7. Channel 1 baseline vs scan position

Channel 2 showed baseline changes in the opposite direction from those of channel 1. At both extremes of the scan, the baseline level decreased. At the lower RSC end, the baseline showed a decrease of between 0.75 and 1.0 denary unit or a voltage drop of between 0.035 and 0.047 v. The decrease at the high RSC end was much more pronounced, amounting to a voltage change from midscan values of about 0.176 v.

A careful study of the channel 2 planetary data, utilizing the computed average baseline data, strongly suggested that the baseline of this channel may depend upon the scan direction; that is, upon whether the scan is ascending or descending. Consequently, baseline averages for ascending and descending modes were computed separately. There was no noticeable difference between the ascending and descending modes for channel 1, but there was for channel 2. The ascending and descending baseline averages are plotted separately in Fig. 9 for channel 2. The possibility that the average baseline for channel 2 was time-dependent was not pursued, as the statistics would not have been good enough.

An analysis of the baseline data with reference to instrument noise characteristics was then carried out. It was of importance to determine the data uncertainty which was caused by noise, and that which was caused by the analog-to-digital (A/D) conversion window width. This was particularly the case for channel 2. If the analysis is restricted to readings between RSC values of 35 and 95, and to a frame count (FC) $\geq$ 60, the average baseline value for channel 1 is 42.1 denary units. The sample deviation s^* was found to be

$$s^* = \left[\frac{\sum_{i=1}^{n} (x_i - \bar{x})^2}{n-1}\right]^{1/2} = 0.038 \text{ v}$$

Using this as an estimate of the variance σ, a probable error of $\sim$0.026 v was obtained.

Another noise parameter pertinent to the planetary data analysis was the maximum indicated level of change in successive data samples. The maximum change that occurred in channel 1 was a step change of 3 denary units, and this occurred only once during the entire encounter data mode. It should also be noted that the peak-to-peak noise showed a definite decrease after initiation of the encounter mode until about FC 60. The step change of

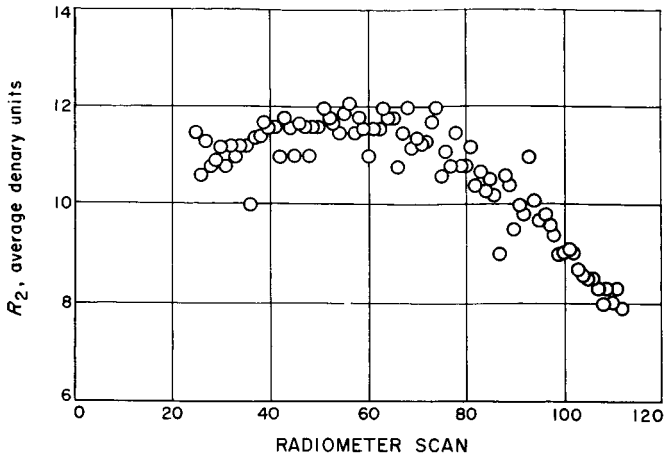

Fig. 8. Channel 2 baseline vs scan position, with ascending and descending readings averaged together

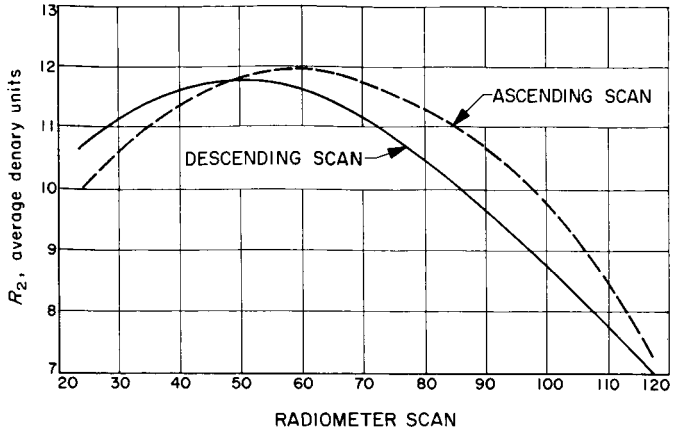

Fig. 9. Channel 2 baseline vs scan position, with ascending and descending readings averaged separately

3 denary units occurred toward the end of FC 36. After FC 60, if the scan extremes of RSC < 35 and > 95 are excluded, there were only 15 2-level step changes in comparison with a combined 0- and 1-level change total of 536. Hence the probability of a 2-level change occurring was only about 2.7% for channel 1. For a calibration signal of about 47 denary units, the ratio of $\Delta V_{pp}/\Delta V_{cal}$ is about 0.075 (assuming $\Delta V_{pp} = \Delta V_{PE}$, which shows an increase of about 60% over the prelaunch value of 0.064, allowing for the time constant change.

For channel 2 it was necessary that standard deviations for the ascending and descending scans be computed separately. Also, because the characteristics of the noise in this channel were an even more pronounced function of time, only data after FC 60 were included. For the ascending mode, the region between RSC 55 and 65 was chosen, while for the descending mode, that between RSC 45 and 55 was chosen. Even over these ranges, the curvature of the plots for baseline vs RSC contributes about 0.1 denary "false" error. The computed values of s^* were 0.74 and 0.56 denary unit for the ascending and descending scan portions respectively, yielding a properly weighted average value of $\overline{s^*} = 0.66$ resulting in a $\overline{PE}$ of 0.44. If the curvature error is subtracted from $\overline{s^*}$, there results a $\overline{PE}$ value of $\sim$0.38 denary unit, or 0.018 v. Assuming again that $\Delta V_{pp} \simeq 6\Delta V_{PE}$, we find that $\Delta V_{pp}/\Delta V_{cal} \sim 0.108/0.44 = 0.26$. This is to be compared with the prelaunch value of 0.13. Hence, there appears to have been about a factor of 3 in signal-to-noise ratio degradation, again allowing for the change in time constant. Part of this, of course, is caused by the finite A/D window width.

B. Calibration Signals

The internal noise tube calibration signals used for the reduction of the data were those that occurred about 1 hr after the planetary data were obtained (calibration number 23). These are plotted in Figs. 10 and 11. An exponential curve was least-squares fitted to the decay portions of the calibration signals. In the case of channel 1, the amplitude of the calibration-on voltage corresponding to turnoff had to be extrapolated into the zero or negative voltage region. The amplitude and level reading of the calibration signal voltage at turnoff, as well as the RC time constant, were varied in obtaining the least-squares fit to the actual calibration signal waveform. A least-squares fit was obtained for $V_0 = -0.06$, $\Delta V = 2.04$, and RC $= 40$. Extrapolation of the waveform beyond turnoff to compensate for the calibration-on warmup characteristics of this channel resulted in a ΔV for β calculations of 2.16 v. The fit neglected the A/D window width.

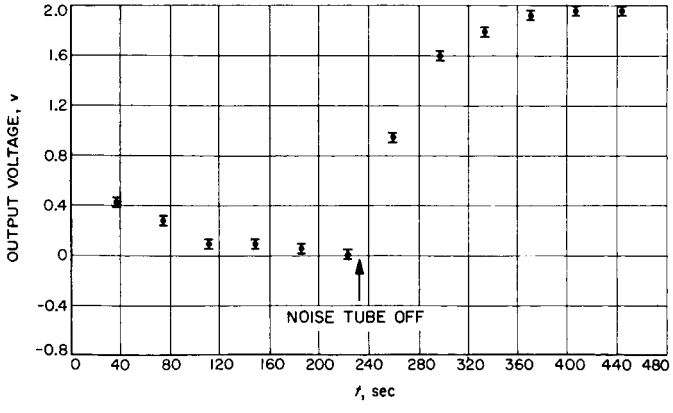

Fig. 10. Channel 1 calibration, day 348

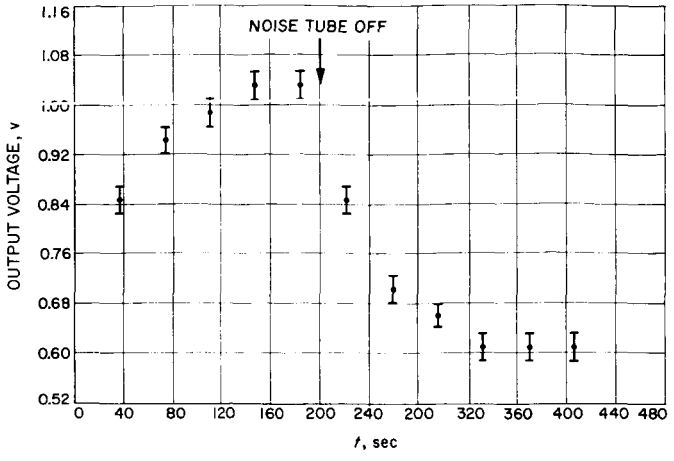

Fig. 11. Channel 2 calibration, day 348

The channel 2 calibration signal was reduced in a manner similar to that of channel 1. The resulting values of ΔV and RC were 0.44 v and 50 sec respectively. The sample standard deviation, again neglecting the A/D window width, was 0.012 v.

C. *Planetary Data*

The plots of the planetary data from both channels are shown in Figs. 12 and 13. The average baseline levels are indicated by the dashed lines. The scans show clearly the effects of beam smoothing and the large value of the RC time constant. In order to discuss the data in terms of any proposed planetary models it was obviously necessary that both of these effects be removed from the data. As a first iteration of the reduction process, smooth curves were drawn through the data points, a simple RC time constant restoration equation was applied, and the resulting curves were compared with theoretical isothermal planet drift scans in which the actual antenna pattern was used. This method of analysis was used for the initial publication regarding this experiment (Ref. 16).

The relationship between the input voltage to an RC integrator and the output voltage (see Appendix A) is

$$x(t) = y(t) + RC\frac{dy}{dt} \tag{34}$$

where $x(t)$ is the input waveform, $y(t)$ the output waveform, and RC the network time constant. This equation was used to remove the effects of time constant smoothing from the smooth curves drawn through the data points.

In order to remove the effects of beam smoothing, the values of the integrals in Eq. (19) of Section III were com-

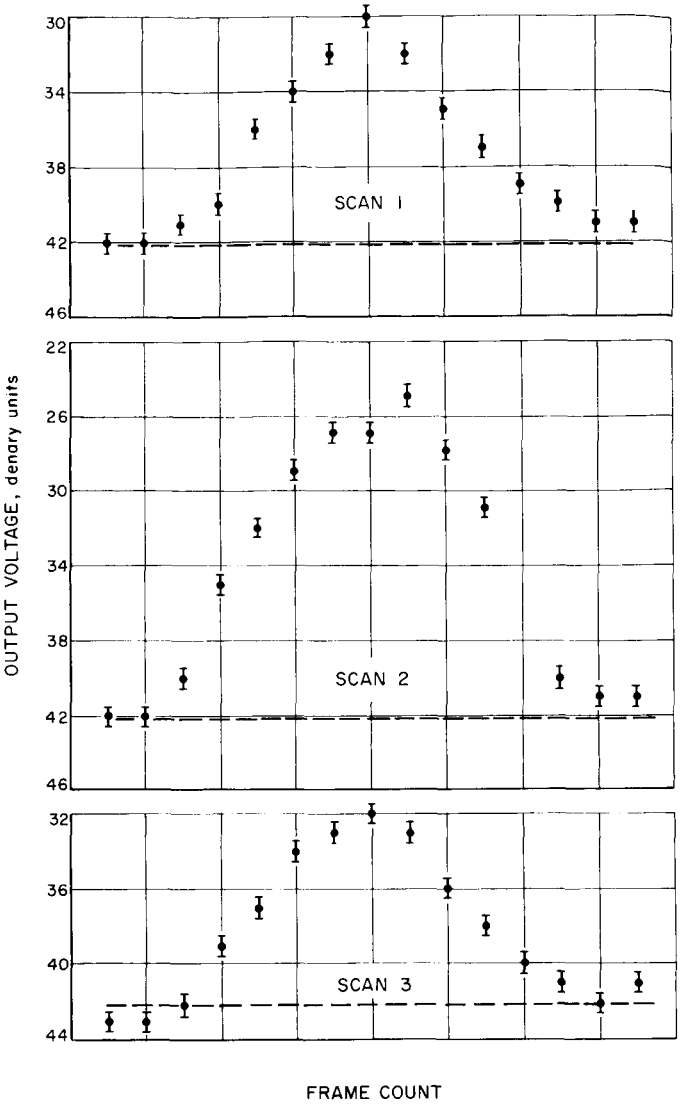

Fig. 12. Channel 1 planetary scans

puted. As a first approximation, the planet was assumed to be an isothermal sphere. Then $I_v(\Omega)$, given by

$$I_v(\Omega) = \int_{\Omega_i} F(\theta',\phi')\, d\Omega \tag{35}$$

and a similar integral applying to the disc absorber, must be computed. In order to simplify the computation, it was assumed that the ellipticity of the beam was negligible so that the dependence of $F(\theta,\phi)$ on ϕ could be dropped (see Section III). Considering the data, it was felt that the increased complexity in the calculations that would result was not justified.

Figure 14 shows the geometry of the problem. The angle α is the angle between the x'' z'' plane of the radiometer-

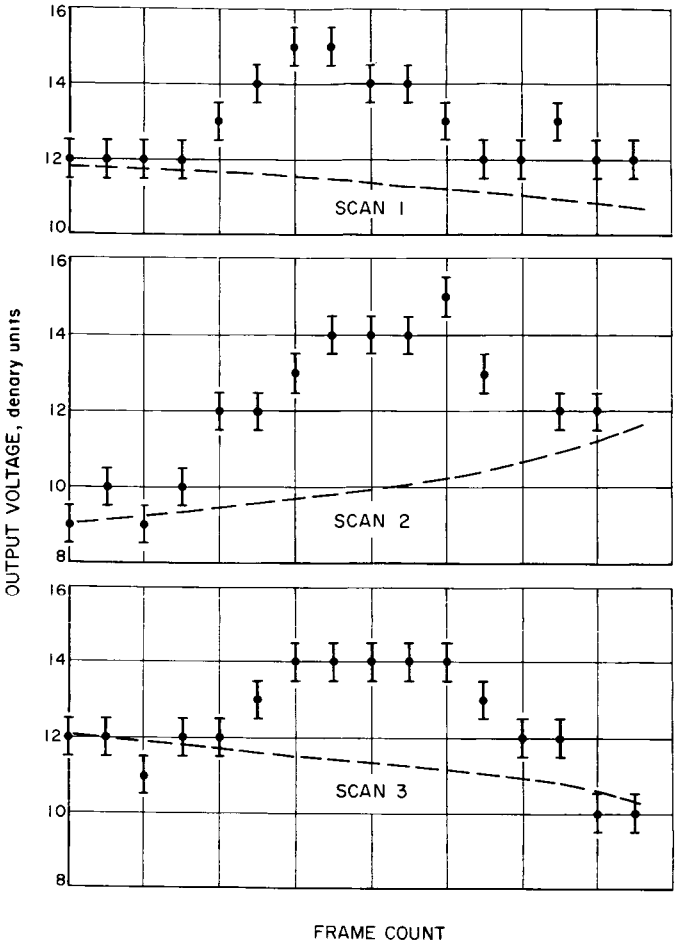

Fig. 13. Channel 2 planetary scans

centered coordinate system and the xy plane of the planet-centered coordinate system. Now, from the Figure,

$$R_p \cos\theta = r \sin\theta' \sin\phi' \cos\alpha + r \cos\theta' \sin\alpha + h$$

$$R_p \sin\theta \cos\phi = d + r \sin\theta' \sin\phi' \sin\alpha - r \cos\theta' \cos\alpha$$

$$R_p \sin\theta \sin\phi = s - r \sin\theta' \cos\phi' \qquad (36)$$

Utilizing the fact that the ϕ' integration limits will be on arcs of constant θ' between tangency points of r and the sphere, or

$$R_p^2 + r^2 = s^2 + d^2 + h^2 \qquad (37)$$

there results

$$Q \cos\phi' - T \sin\phi' = P$$

where

$$P = 1 + \frac{h}{\sqrt{H}} \cos\theta' \sin\alpha - \frac{d}{\sqrt{H}} \cos\theta' \cos\alpha \qquad (38a)$$

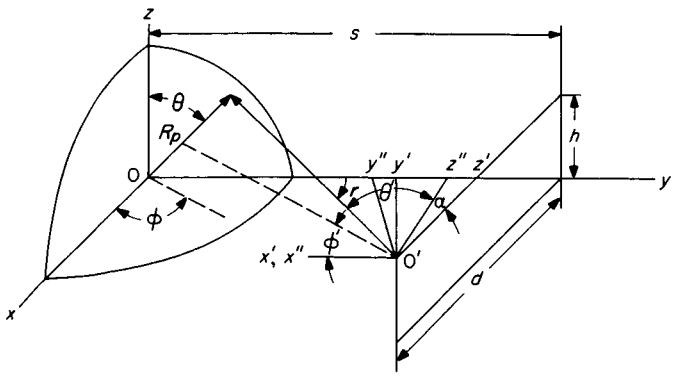

Fig. 14. Planet–radiometer pattern convolution geometry

$$Q = \frac{s}{\sqrt{H}} \sin\theta' \qquad (38b)$$

$$T = \frac{h}{\sqrt{H}} \sin\theta' \cos\alpha + \frac{d}{\sqrt{H}} \sin\theta' \sin\alpha \qquad (38c)$$

$$H = \sqrt{s^2 + d^2 + h^2 - R^2} \qquad (38d)$$

The s/R values used for the three planetary scans were 0.74, 0.00, and 0.87 for scans 1, 2, and 3 respectively. Changes in the planet–spacecraft distance that occurred during a scan amounted to only about 0.3% and hence were neglected. Values for s/R were obtained from computed values of the angle between the radiometer beam axis and the planetary surface normal at midscan. Plots of I_v vs scan angle α for the three scans are shown in Fig. 15 for channel 1 and in Fig. 16 for channel 2.

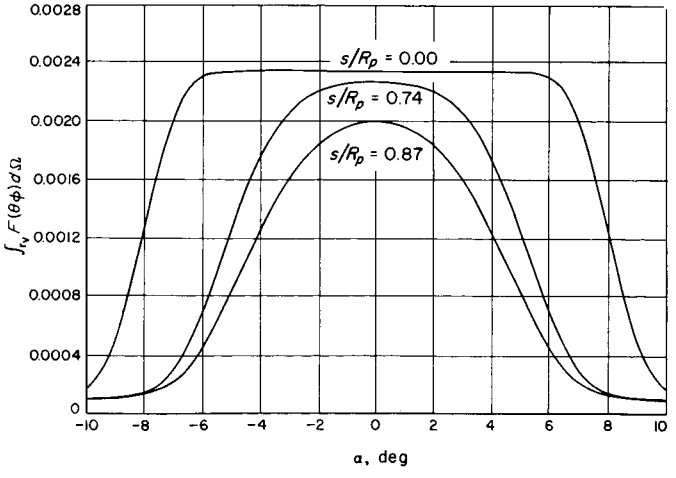

Fig. 15. The pattern integral $\int_{\Omega_v} F(\theta, \phi)\, d\Omega$ vs α, channel 1

For the integral in the numerator of Eq. (19) the value of

$$I_D(\theta) = 2\pi \int_0^{\theta} F(\theta') \sin\theta' \, d\theta' \qquad (39)$$

was computed. Plots of $I_D(\theta)$ vs θ for both channels are shown in Fig. 17.

The procedure of estimating a smooth curve through the data points and applying Eq. (34) did not lend itself to nearly as reliable an estimate of the probable error as desired. Consequently, the method of "least squares" was used to obtain a best fit of an isothermal model. The method consisted of computing drift scans normalized to unity at midscan and multiplying these by a factor k'. Curves of various k' values were "fitted" until the quantity

$$s^* = \left[\sum_{i=1}^{n} \frac{(x_{i_d} - x_{i_t})^2}{n-1} \right]^{1/2}$$

was a minimum. Here x_{i_d} is the voltage value of the data point, and x_{i_t} is the corresponding theoretical value. The minimum value of s^* so obtained was then used as a best estimate of the variance.

In this approach to the data analysis, an assumed input waveform $(x)t$ is theoretically "smoothed" by an RC integrator in order to obtain an output $y(t)$ that can be compared with the actual data plots. The relationship (see Appendix B) is

$$y(t,k',RC) = k' \int_0^t \alpha(t-\tau) \frac{\exp(-\tau/RC)}{RC} \, d\tau \qquad (40)$$

In Figs. 18 through 23 are plotted the actual data and the corresponding best-fit curves. The resulting β and peak temperature values for the three scans of both channels are listed in Table 5. Of interest in the interpretation of the data are the relative temperatures; that is,

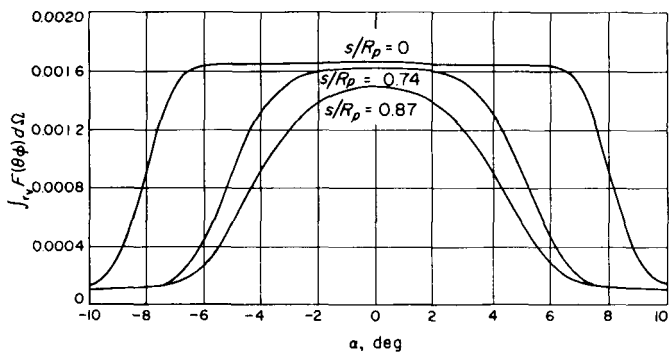

Fig. 16. The pattern integral $\int_\Omega F(\theta, \phi)\, d\Omega$ vs α, channel 2

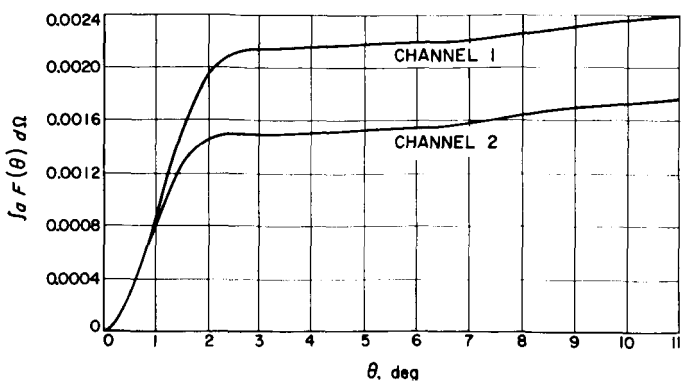

Fig. 17. The pattern integral $\int_\Omega F(\theta)\, d\Omega$ vs θ channels 1 and 2

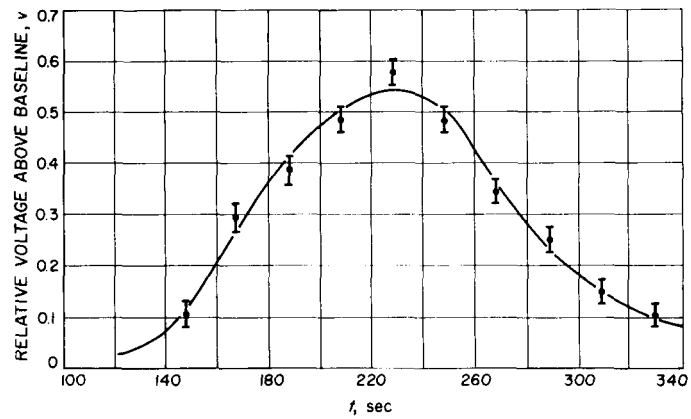

Fig. 18. Channel 1, scan 1 ($k' = 0.640$)

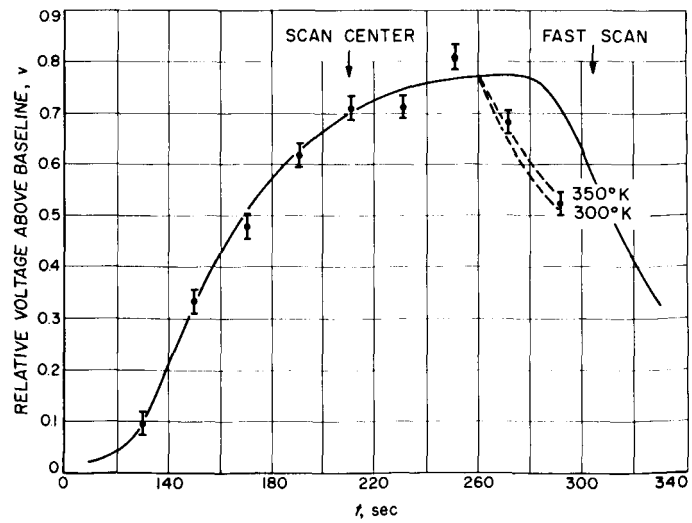

Fig. 19. Channel 1, scan 2 ($k' = 0.809$)

Table 5. Calibration signal parameters and midscan planet temperatures

Channel No.	RC, sec	Calibration amplitude, v	s^*, v	Scan No.	k', v	s^*, v	β	T_V, °K	Relative PE, °K	r_{12}	PE
1	40	2.16	0.021	1	0.640	0.021	0.291	490	11	0.821	±0.024
				2	0.809	0.024	0.368	595	12	—	—
				3	0.590	0.025	0.268	511	14	0.860	±0.027
2	50	0.44	0.012	1	0.206	0.018	0.470	380	22	0.970	±0.075
				2	0.221	0.017	0.504	392	21	—	—
				3	0.200	0.017	0.455	394	23	1.001	±0.085

$r_{12}(= T_{B_1}/T_{B_2})$ and $r_{32}\ (= T_{B_3}/T_{B_2})$. These are also tabulated along with the relative probable error. The relative probable error was computed from

$$\Delta r_{ij} = \sqrt{\left(\frac{\partial r_{ij}}{\partial T_{B_i}} \Delta T_{B_i}\right)^2 + \left(\frac{\partial r_{ij}}{\partial T_{B_j}} \Delta T_{B_j}\right)^2} \qquad (41)$$

It is of interest to compare the values of s^* pertaining to the scans listed in Table 5 with the values for the two channels computed from the baseline data. For both channels it is noted that the baseline s^* values are about 50–60% higher than the scan values. This is not significant, particularly if it is noted that there were more than 20 runs for channel 1 and 26 runs for channel 2 of blocks of 6 to 10 data points in which there was no output change at all.

It is readily apparent that with the temperature ratios r_{12} and r_{32} giving evidence of the existence of limb darkening, the computed values of T_{B_1}, etc., themselves will be in error because, for the data analysis, the planet was assumed to be isothermal. The effect of the presence of limb-darkening will be to shift all T_B values down from the on-axis, zero-beamwidth values. For T_{B_2}, the presence of limb-darkening means that the level of radiation into the side lobes will be lower than the on-axis value, and hence the effective T_B will be lowered from its true value. However, for scans 1 and 3, the tendency for limb-darkening to pull the value of T_B down may well be offset by the fact that the off-axis planetary radiation will be predominantly from an effective T_B that is higher than the on-axis component. The net result is that the degree of limb-darkening as observed by a radiometer of much narrower beamwidth would in all probability be greater. It is estimated that the degree of limb-darkening is probably 1% greater than that quoted here for channel 1.

It is evident in Figs. 19 and 22, pertaining to scan 2 of channels 1 and 2 respectively, that a temperature anomaly occurred toward the end of this scan. If we refer to the discussion of the probable noise characteristics of the radiometer at the planet, it is seen that this anomaly cannot be considered as being due only to noise, particularly for channel 1. The possibility exists that the channel 2 anomaly was due to a combination of noise and the finite A/D window width, although the position of the anomaly with respect to the one that occurred in channel 1 would appear to be more than a coincidence. Careful consideration of these factors results in the strong probability that the anomaly in channel 2 is real also.

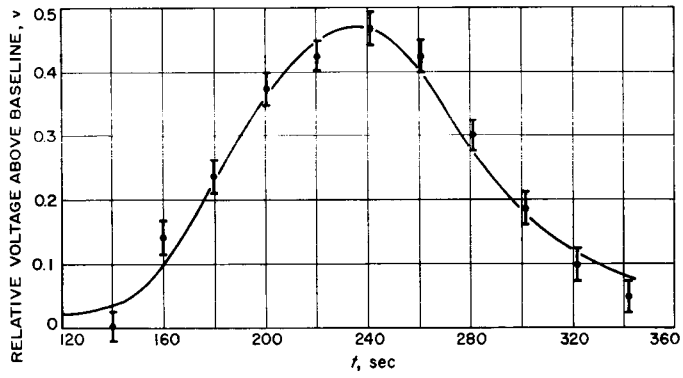

Fig. 20. Channel 1, scan 3 ($k' = 0.590$)

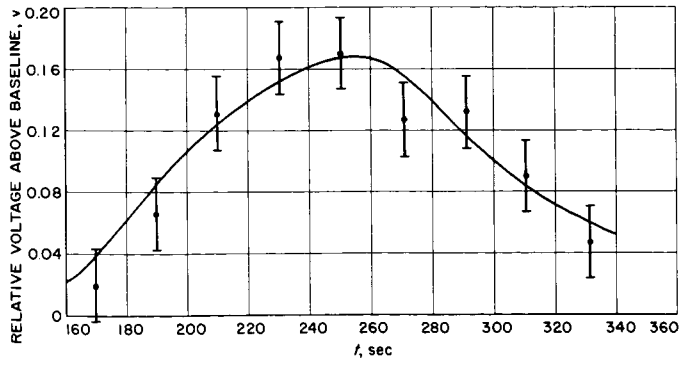

Fig. 21. Channel 2, scan 1 ($k' = 0.206$)

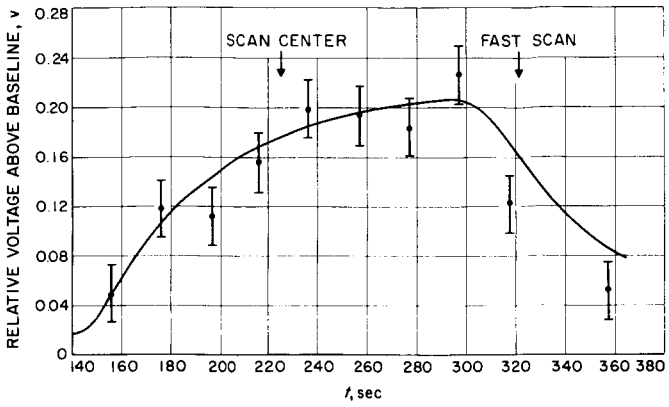

Fig. 22. Channel 2, scan 2 ($k' = 0.221$)

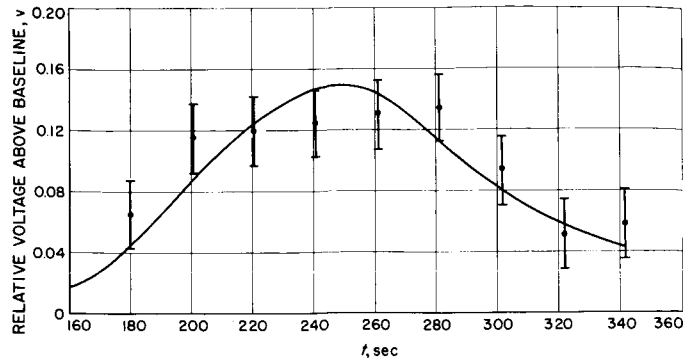

Fig. 23. Channel 2, scan 3 ($k' = 0.200$)

VI. INTERPRETATION OF DATA

One method of attempting to interpret the planetary data is to compute the limb-darkening ratios predicted by a number of assumed models for the planet that would correspond to measurements at the subject wavelengths at each of the midscan positions. In this manner, the number of assumed models that can exist will be decreased to the point at which critical tests at these and other wavelengths may establish which model is the correct one. This is the method that is used in this Section. The models assumed were fairly simple, as the goal was to determine only the gross features of the type of atmosphere–surface model combination that would best fit the data. The data are not good enough to include some of the complicating features that one can conceive of for the various subclasses of these general-type models.

A. 19-mm Limb-Darkening Evidence and Analysis

If the planetary disc were isothermal, then obviously all the values of T_V should have been equal. However, in the case of the 19-mm data, they are not, and since the values of T_V for scans 1 and 3 are both less than that of scan 2, limb-darkening is indicated. Only the peak values of each scan have been considered, but it is obvious that the shapes of the individual scans are consistent only with drift scans produced by an isothermal or a limb-darkened planet.

Consideration was given to the possibility that some effect other than that due to the planet itself might have caused the observed differences in scan temperatures. There was a remote possibility that because of the spacecraft–planet geometry and the orientation of the reference horns with respect to the scan plane, etc., some of the planetary radiation may have gotten into one of the side-lobe response areas of the reference horns. This, of course, has particular reference to scan 3. Scan 1 and scan 2 are conceivably compatible, since one would expect a brightness temperature dependence on phase angle for most of the models that have been proposed. Although the change from a value of 489°K for scan 1 to a value of 595°K for scan 2 is characteristic of a rather strong phase effect, at least the effect is in the right direction. If radiation from the planet were to enter the reference horns during scan 3, while not doing so during scans 1 and 2, the indicated scan 3 temperatures would be decreased.

At the time the sunlit scan was being taken, the planet extended over a region of the pertinent E-plane antenna pattern where the response varied smoothly from -23 to -30 db. Considering the fact that the RF bandwidth of the reference horn section for channel 1 was larger than that of the diplexer section, and assuming a worst-case condition for the antenna pattern of -23 db, the computed T_A at the crystal (owing to the planet getting into the reference horn side lobes) is still more than 2 orders of magnitude below that of the main feed. Hence, this possible explanation for the low value of T_{B_3} must be ruled out.

In attempting to match the indicated 19-mm limb-darkening theoretically, several types of atmospheric structure–surface temperature distribution combinations were utilized in computing brightness temperature ratios corresponding to the location of the antenna beams on the planetary disc at the midpoint of each scan. For the first model, the atmosphere was assumed to consist of CO_2 and N_2 under high pressure, and the surface was assumed to be isothermal and rough at 19 mm. Several models with differing proportions of CO_2 and N_2 were considered. Adiabatic and subadiabatic atmospheric lapse rates were assumed for the region below the clouds, with the region above the clouds assumed to be isothermal at 235°K.

The radiative transfer equation leads, for the case of an infinitely narrow beamwidth, to the equation for the brightness temperature (see Appendix B):

$$
\begin{aligned}
T_B(\theta) = {} & \\
& \epsilon T_s \exp(-\tau_{\max} \sec\theta) \\
& + A \exp\left\{\left[\zeta A \left(\frac{\gamma-1}{a}\right) T_c^{a/(\gamma-1)} - \tau_c'\right] \sec\theta\right\} \\
& \times \int_{T_c}^{T_s} T^{a/(\gamma-1)} \exp\left(-\zeta A \frac{\gamma-1}{a} T^{a/(\gamma-1)} \sec\theta\right) \sec\theta \, dT \\
& + T_c\left[1 - \exp(-\tau_c' \sec\theta)\right] + T_R
\end{aligned}
\tag{42}
$$

with T_R the reflected atmospheric radiation. Under the assumption that the surface is perfectly rough at 19 mm,

the reflected term is due to the sky radiation averaged over all angles. For this model there results (see Appendix B)

$$T_R \sim 2\zeta(1-\epsilon_d) \times A \exp\left\{-\left[2\zeta A\left(\frac{\gamma-1}{a}\right)T_s^{a/(\gamma-1)} + \tau_{\max}\sec\theta\right]\right\} \times \int_{T_s}^{T_c} T^{a/(\gamma-1)} \exp\left[2\zeta A\left(\frac{\gamma-1}{a}\right)T^{a/(\gamma-1)}\right] dT + (1-\epsilon_d)T_c\,(1-e^{-2\tau_c'}) \exp\left\{-(2\tau_a' + \tau_{\max}\sec\theta)\right\} \tag{43}$$

For an atmosphere containing 20% CO_2 and 80% N_2, values for γ and m are 1.362 and 52.4×10^{-24} respectively. In Figs. 24 and 25 are curves of $r_{12}(=T_{B_1}/T_{B_2})$ vs P_s and $r_{32}(=T_{B_3}/T_{B_2})$ vs P_s for an adiabatic atmosphere and for various T_s and ϵ combinations such that $\epsilon T_s \sim 625°K$. A plot of T_{B_2} vs P_s for this model is shown in Fig. 26. In order to estimate the effect of decreasing the amount of CO_2 assumed in the atmosphere, similar calculations for 5% CO_2 and 95% N_2 were made. This amount of CO_2 is nearer the value given by Spinrad (Ref. 21). For this case the values of γ and m used were 1.387 and 48.0×10^{-24} respectively. The resulting variations of r_{12} and r_{32} vs P_s at constant T_s and ϵ were similar to those for the 20% CO_2 case except, of course, that they were shifted to higher pressures.

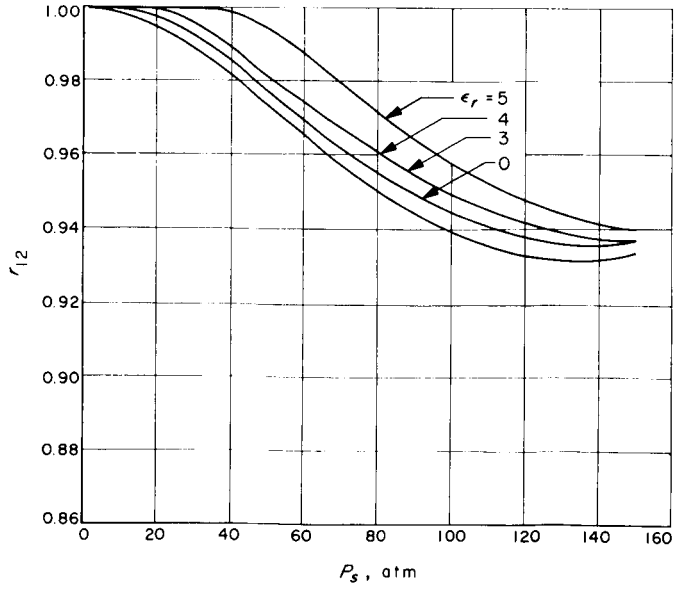

Fig. 24. Brightness temperature ratio r_{12} vs surface pressure P_S, adiabatic atmosphere, 20% CO_2 rough surface, constant T_S

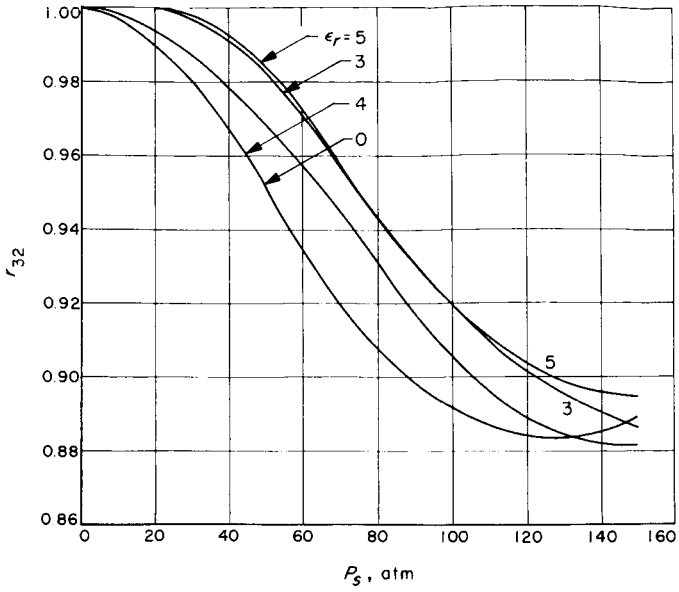

Fig. 25. Brightness temperature ratio r_{32} vs surface pressure P_S, adiabatic atmosphere, 20% CO_2 rough surface, constant T_S

Figures 24 and 25 show the gross effect on r_{12} and r_{32} of increasing the dielectric coefficient of the surface material. As the dielectric coefficient is increased, the region of the atmosphere in the vicinity of the surface begins to play a comparable role in the observed brightness temperature. This effect is seen in Fig. 26 where, for example, with $\epsilon_r = 5.0$, the value of T_{B_2} actually increases with pressure until a maximum value is obtained at $P_s \sim 70$ atmospheres. At higher pressures, absorption by the cooler upper regions begins to dominate.

It is apparent that the uniform surface–adiabatic atmosphere model with a nonresonant-type absorber in constant mixing ratio throughout the atmosphere cannot predict limb-darkening ratios that satisfactorily match the observed ratios. Also, the curves of T_{B_2} vs λ for this model do not satisfactorily match the observed microwave spectrum.

Allowance for departure from adiabaticity was then included. Here it was assumed that the atmospheric subadiabatic index ζ was constant for the three scans. As an iteration of this model, it was assumed that in the sunlit region the atmosphere had an adiabatic lapse rate, in the dark portion some index value ζ, and in the terminator region an index value of $(\zeta + 1)/2$. Plots of the ratios r_{12} and r_{32} vs P_s at constant T_s and for various constant subadiabatic indices ζ are shown in Figs. 27 and 28 for a 20% CO_2, 80% N_2 atmosphere. Again, the 5% CO_2 model

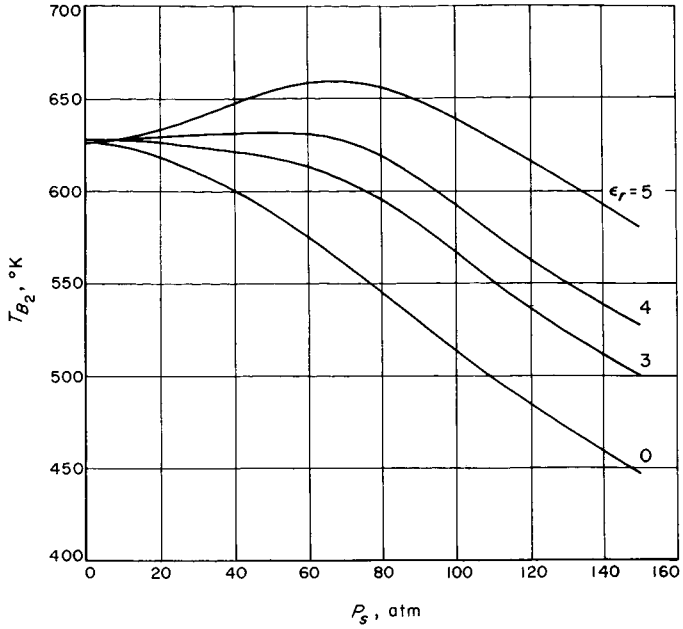

Fig. 26. Brightness temperature T_{B_2} vs surface pressure P_S, adiabatic atmosphere, 20% CO_2, rough surface

results are similar except for the magnitudes of surface pressure required. The plots are for $\epsilon = 0.89$ ($\epsilon_r = 4.0$) only, the values for $\epsilon = 1.0$ and 0.82 not being noticeably different. The results of assuming a variation in the subadiabatic index over the disc of the planet are seen in Fig. 29.

It is apparent that the effect of increasing the subadiabatic index is to increase the ratios r_{12} and r_{32}. This would indicate that an atmosphere with a lapse rate

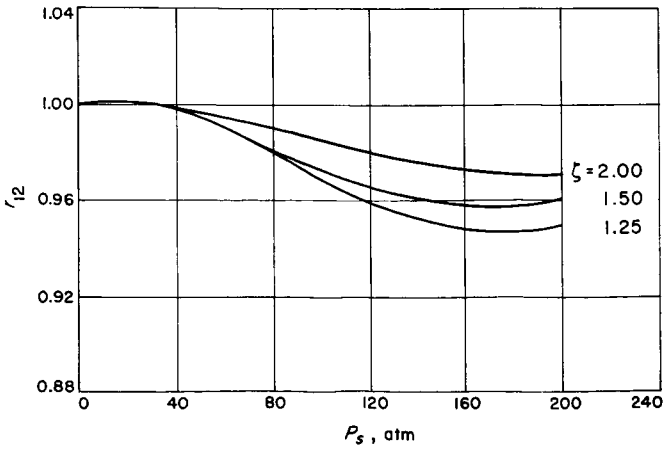

Fig. 27. Brightness temperature ratio r_{12} vs surface pressure P_S, 20% CO_2, constant ζ, ϵ, T_S, rough surface

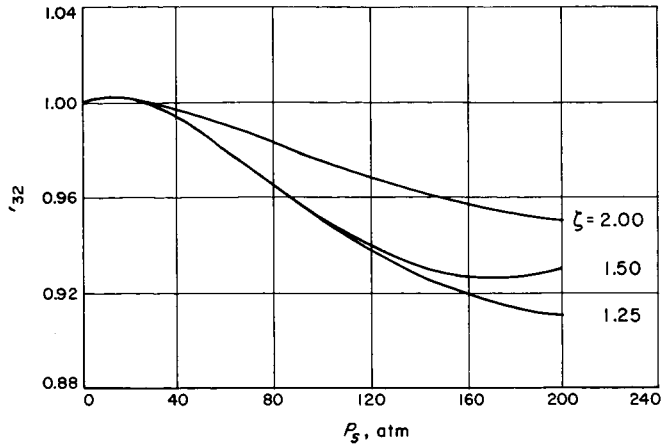

Fig. 28. Brightness temperature ratio r_{32} vs surface pressure P_S, 20% CO_2, constant ζ, ϵ, T_S, rough surface

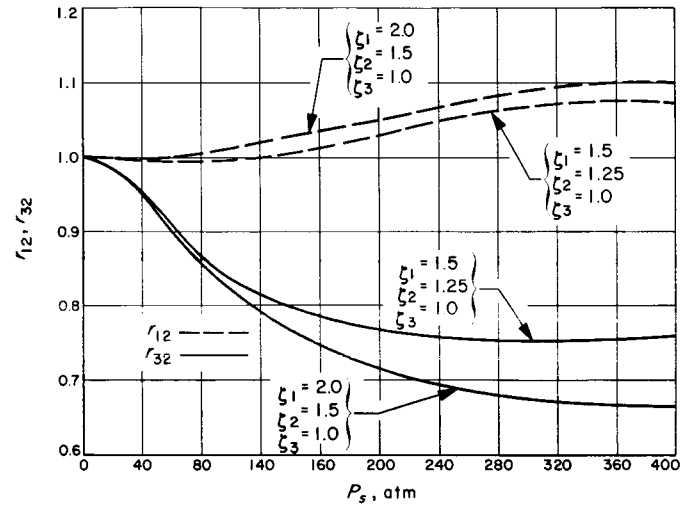

Fig. 29. Brightness temperature ratios r_{12} and r_{32} vs surface pressure P_S, adiabatic–subadiabatic, 20% CO_2, rough surface (T_S = 625°K, ϵ = 1.00)

greater than the adiabatic value might yield limb-darkening ratios compatible with the measured values. For obvious reasons, this possibility was not pursued. In Fig. 29 it is noted that if the surface pressure is approximately constant over the planet, the dark-side brightness temperature would be greater than that of the light side if the subadiabatic index of the dark side is greater than that of the light side (see Ref. 9).

Figures 30 through 32 show plots of T_{B_2} vs P_s for various values of ϵ_r and ζ. The effect of increasing ϵ_r (and T_s to keep $\epsilon T_s \sim$ 620–625°K) is similar to that observed for the adiabatic model except that it is noted that

increasing the subadiabatic index decreases the relative absorbing effect of the upper cooler regions of the atmosphere at the same surface pressure.

It is clear that neither an adiabatic nor subadiabatic atmosphere in combination with a rough surface will predict the observed limb-darkening ratios. A simple isothermal-layer or cloud-type model was then assumed. The equation that applies to this model is simply (assuming again that the surface is a perfectly diffuse scatterer)

$$T_B = \epsilon_n T_s\, e^{-\tau \sec\theta} + T_A\,[1 - e^{-\tau \sec\theta}] + (1 - \epsilon_n) T_A\,[1 - e^{-2\tau}]\, e^{-\tau \sec\theta} \qquad (44)$$

where T_A is the assumed atmospheric layer temperature, τ the integrated opacity of the layer, and $\epsilon_n T_s$ the surface brightness temperature. The values for T_A, τ, and $\epsilon_n T_s$ were varied in an attempt to obtain midscan temperature ratios that matched the observed ratios. The results of these calculations are shown in Figs. 33 and 34 for $\epsilon_n = 1.0$. The curves are plots of r_{12} and r_{32} vs integrated opacity τ at constant atmospheric temperature T_A. The particular set is for $\epsilon_n T_s \sim 625°$K. For $T_A = 200°$K and for $\tau \geq 0.2$, values sufficiently close to the observed values are obtained for the r_{32} ratio. A value of τ greater than 0.8 is required for r_{12}. As mentioned before, one constraint that any model must satisfy is that the predicted integrated disc temperature must not be less than that obtained from the Earth. The triangles on the curves indicate points beyond or to the right of which gross

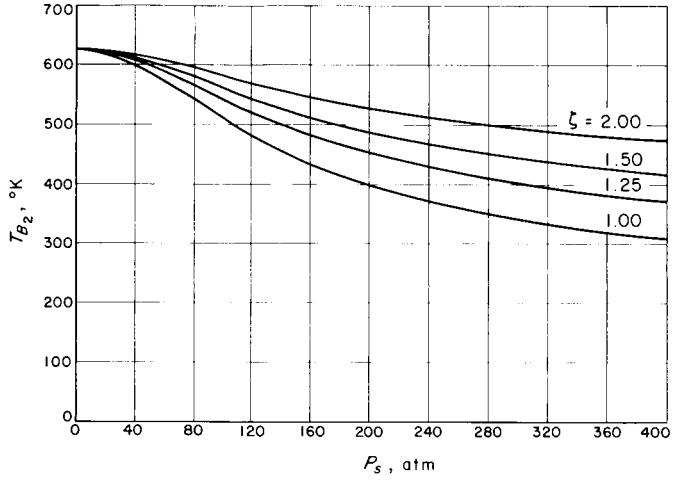

Fig. 30. Brightness temperature T_{B_2} vs surface pressure P_S, subadiabatic atmosphere (T_S = 625°K, ϵ = 1.00)

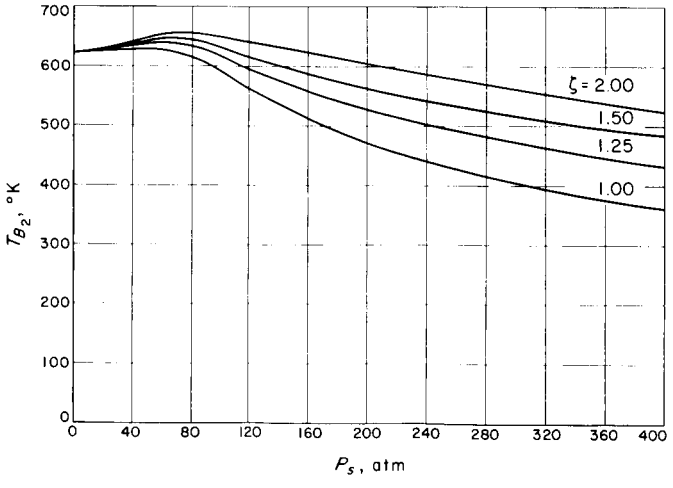

Fig. 31. Brightness temperature T_{B_2} vs surface pressure P_S, subadiabatic atmosphere (T_S = 700°K, ϵ = 0.89)

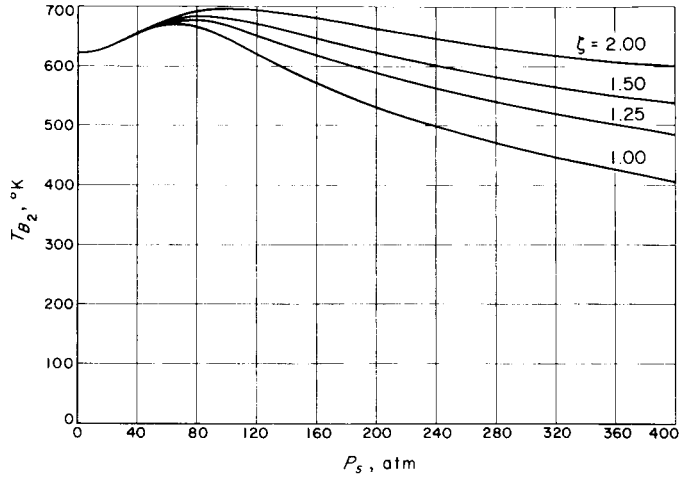

Fig. 32. Brightness temperature T_{B_2} vs surface pressure P_S, subadiabatic atmosphere (T_S = 760°K, ϵ = 0.82)

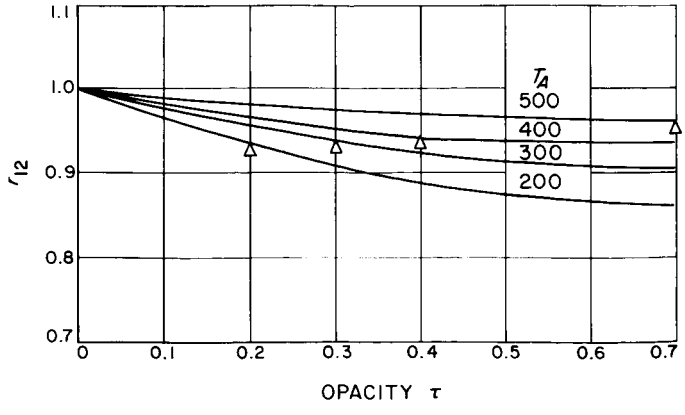

Fig. 33. Brightness temperature ratio r_{12} vs τ, isothermal layer model

disagreement with Earth-based data occurs. Imposing this restriction results in the conclusion that the degree of limb-darkening predicted by this model is not sufficient to explain the observed darkening ratios. Allowing for a temperature gradient in the cloud increases the limb-darkening, but not to a sufficient degree.

Several possible means of explaining the excessive limb-darkening are related to the brightness temperature of the surface. One might argue that the composition of the surfaces pertaining to scans 1 and 3 is radically different from that of scan 2, in that the gross emissivity of the surface in the latter was significantly higher than in the former. However, the anomalous surface composition differences would have to be prevalent over the entire three scans, and such large emissivity differences over such large areas would surely have been detected by radar. Another possibility regarding the character (roughness and dielectric coefficient) of the surface exists, which, in combination with a microwave-absorbing atmosphere, explains the observed limb-darkening.

The surface emissivity factor used previously in Eqs. (42), (43), and (44) was assumed to be independent of the angle between the emergent radiation and the local normal to the surface (perfectly diffuse scatterer). If it is assumed that the surface discontinuities are small enough, then the surface will behave as a specular reflector, ϵ will be a function of θ, and polarization effects will be seen. Even if the vertical discontinuities are large compared with λ, the surface can still appear relatively smooth and exhibit polarization effects nearly as great as a "smooth" surface if the correlation length between discontinuities is long compared with λ. The brightness temperature of such a surface as a function of θ will show a marked variation difference, depending upon whether one is observing vertical or horizontal polarization, and the magnitude of this effect is a function of the electrical properties of the surface material.

The expressions for the well-known horizontal and vertical emissivities (see Appendix B) are

$$\epsilon_h = 1 - \frac{(\cos\theta - Q^{1/2}\cos\psi/2)^2 + Q\sin^2\psi/2}{(\cos\theta - Q^{1/2}\cos\psi/2)^2 + Q\sin^2\psi/2}$$

$$\epsilon_v = 1 - \frac{(\epsilon_r\cos\theta - Q^{1/2}\cos\psi/2)^2 + (\epsilon_i\cos\theta + Q^{1/2}\sin\psi/2)^2}{(\epsilon_r\cos\theta + Q^{1/2}\cos\psi/2)^2 + (\epsilon_i\cos\theta - Q^{1/2}\sin\psi/2)^2}$$

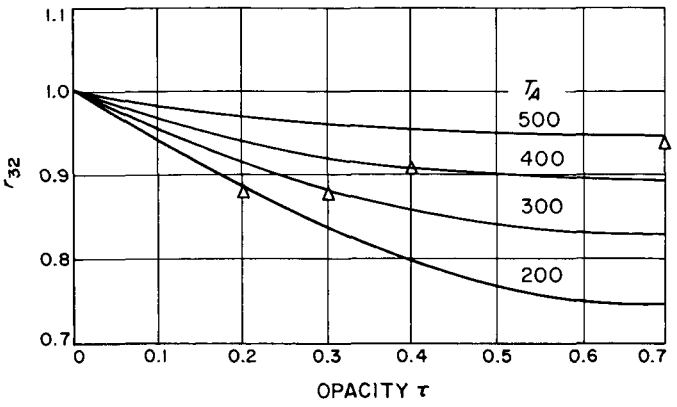

Fig. 34. Brightness temperature ratio r_{32} vs τ, isothermal layer model

The pertinent emissivity to be used for the peak values of the three scan centers is ϵ_h, while ϵ_r applies to portions of scan 2 other than at scan center and will be discussed later.

With the assumption that the surface was smooth at 19 mm, ratios r_{12} and r_{32} were recomputed for the several model atmospheres discussed previously, using values of ϵ_h derived from assumed values of ϵ_r and ϵ_i. The values of ϵ_h corresponding to the midpoints of the three scans for various assumed values of ϵ_r (ϵ_i is assumed to be zero) are listed in Table 6, along with computed values of r_{12} and r_{32} pertaining to surface brightness temperatures under the assumption that the effect we are observing is due entirely to the surface. For the variable T_s case, a simple synchronous-type distribution of the form

$$T_s = T_0 + \Delta T\cos\phi \qquad (45)$$

was assumed, where ϕ is the longitude angle on the planet, referred to the subsolar point. Whereas it is possible to obtain a crude match to the observed ratios for ϵ_r values between 4.0 and 6.0, the fact that no "limb brightening" at the Brewster angle was evident in scan 2 is compatible only with $\epsilon_r \sim 2.0$ or less, even if beam smoothing is considered. Beam smoothing still requires $r_{42} \leq 1.03$, where the subscript 4 refers to observations at the Brewster angle. Another problem with this interpretation is the fact that the measured peak temperature for scan 2 is 595°K, and hence atmospheric absorption is required.

Table 6. Horizontally polarized emissivity ϵ_h and corresponding r_{i2} values for brightness temperature ratios r_{12} and r_{32}, under the assumption of no atmosphere

ϵ_r	ϵ_h			Brightness temperature ratio				
				At fixed T_s		At variable T_s		
	Scan 1	Scan 2	Scan 3	r_{12}	r_{32}	ΔT, °K	r_{12}	r_{32}
2.0	.920	.970	.853	.95	.88	—	—	—
3.0	.841	.928	.748	.91	.80	50	.865	.858
4.0	.780	.889	.678	.88	.76	65	.815	.818
5.0	.733	.854	.627	.86	.73	80	.790	.801
6.0	.698	.823	.587	.84	.71	90	.770	.785
8.0	.634	.772	.527	.82	.68	100	.750	.754
10.0	.589	.730	.484	.81	.66	100	.740	.730

The results of incorporating the values of ϵ_h listed in Table 6 in the computations involving the adiabatic model are shown plotted in Figs. 35 through 39. It is seen that under the assumption that the value of T_{B_2} was indeed ~595°K (that is, less than 625°K), the required surface pressures corresponding to the various values of ϵ_r result in r_{12} and r_{32} values that are both too high for the fixed T_s case. For those values of ϵ_r that result in r_{12} values that are within two probable errors of the measured ones, r_{32} is clearly too high. Also, the Brewster "peaking" for the higher ϵ_r values is difficult to reconcile with the shape of scan 2. If one assumes that all of the channel 2 temperatures are too low, then one runs into the same Brewster "peaking" problem as noted for the "atmosphereless" model discussed earlier. There must be at least a minimal amount of atmospheric absorption, dependent upon the value of ϵ_r, to wash out the Brewster effect sufficiently. It is concluded that in attempting to match the limb-darkening ratios and the brightness temperature values of the *Mariner* experiment, as well as to keep the predicted brightness temperatures compatible with the measurements of McCullough and Boland at 2.07 cm (Ref. 22), one clearly runs into difficulty with a model invoking only CO_2 gas under high pressure in

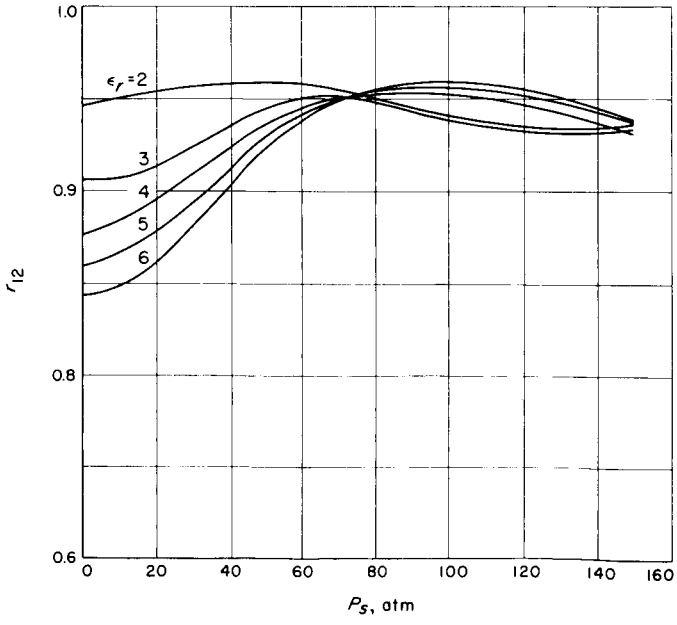

Fig. 35. Brightness temperature ratio r_{12} vs surface pressure P_S, adiabatic atmosphere, 20% CO_2, smooth surface, constant T_S

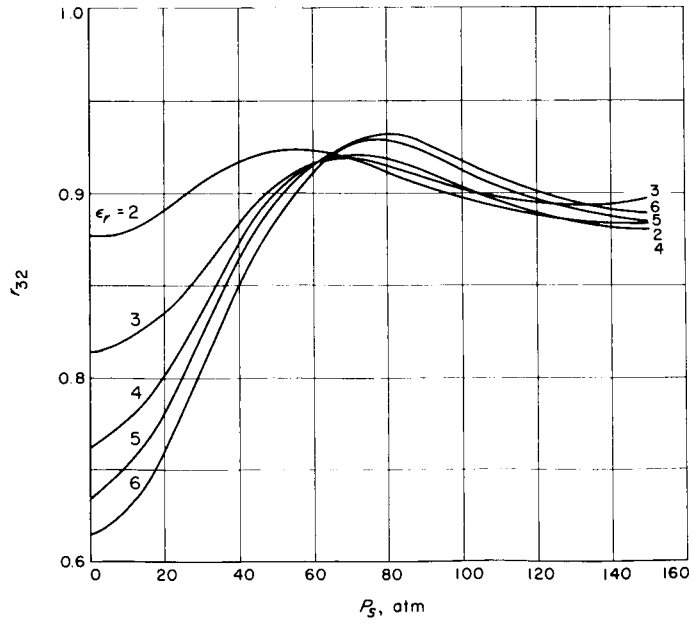

Fig. 36. Brightness temperature ratio r_{32} vs surface pressure P_S, adiabatic atmosphere, 20% CO_2, smooth surface, constant T_S

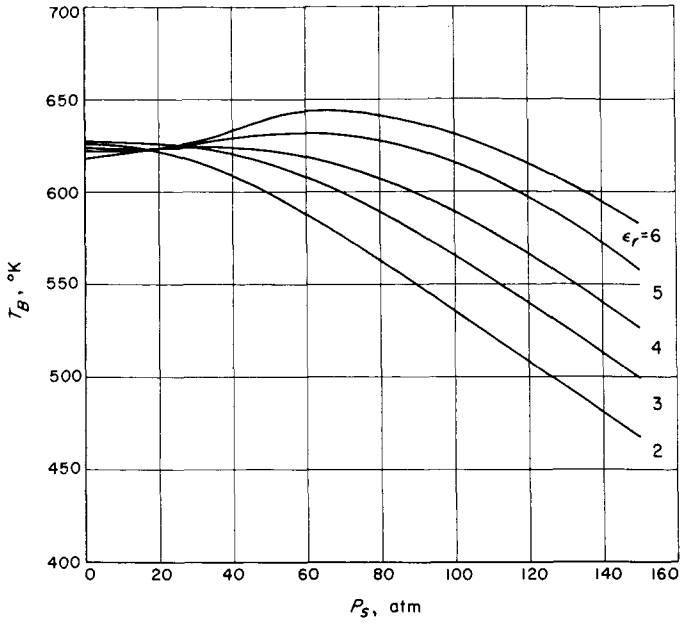

Fig. 37. Brightness temperature T_{B_2} vs surface pressure P_S, adiabatic atmosphere, 20% CO_2, smooth surface

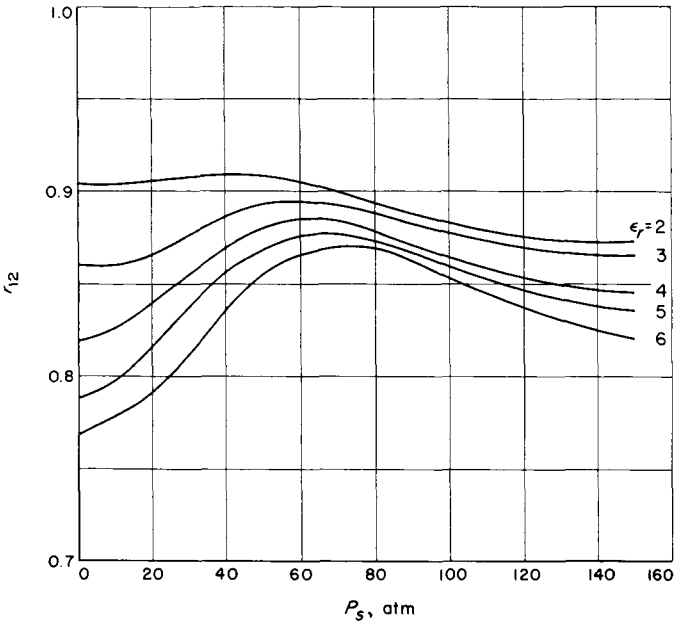

Fig. 38. Brightness temperature ratio r_{12} vs surface pressure P_S, adiabatic atmosphere, 20% CO_2, smooth surface, variable T_S

combination with either a specular or diffuse type of surface.

It is therefore instructive to consider the simple isothermal or cloud-type model in combination with a specular surface. Using Eq. (44) suitably modified to incorporate the effects of a specular surface, values of r_{12} and r_{32} were computed for such fixed values of T_s that again $T_{B_S} \sim 625°K$. In addition, values of r_{42}, which refer to the predicted Brewster angle brightening ratio modified by atmospheric absorption and beam smoothing, were also computed. The fixed T_s case was obviously unsuccessful, but fairly satisfactory results were obtained for the variable T_s case. For an ϵ_r value of 3.0, a good fit was obtained with $\Delta T = 75°K$ and $T_A = 250°K$, and a fair fit with $T_A = 350°K$. For $\epsilon_r = 4.0$, a good fit was obtained with $\Delta T = 85°K$ and $T_A = 350°K$, and a fair fit with $T_A = 250°K$. These models are compatible with the constraint imposed on r_{42} by the shape of the first half of scan 2. It is concluded that a specular surface having a value of ϵ_r between 3 and 4, in combination with an isothermal-layer or cloud-type model atmosphere having T_A between 250 and 350°K, best fits the peak temperature ratios of the 19-mm scans.

The lower value of 250°K for T_A could be considered to be compatible with a liquid-water cloud, whereas a value much greater than 250°K would not. To be able

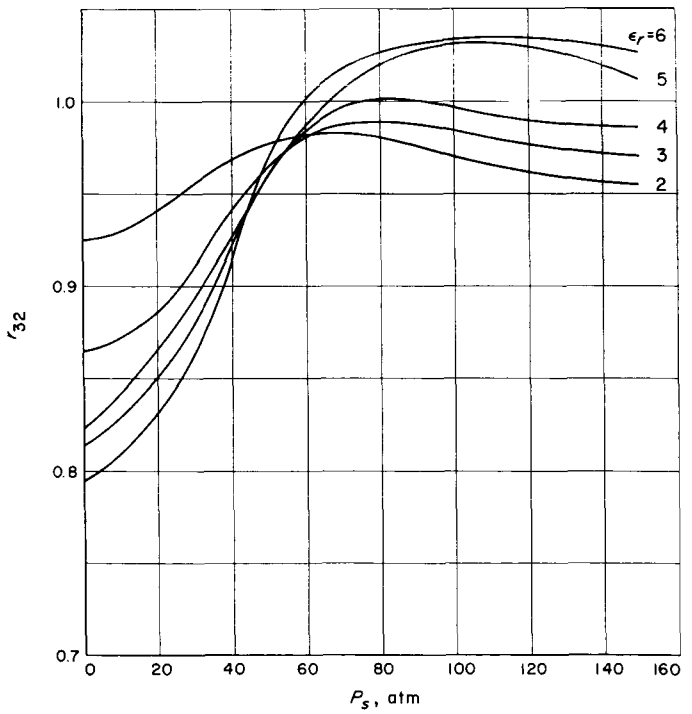

Fig. 39. Brightness temperature ratio r_{32} vs surface pressure P_S, adiabatic atmosphere, 20% CO_2, smooth surface, variable T_S

to establish through the use of other data that the cloud temperature was more likely 350 than 250°K would force one to consider a substance other than condensed water vapor as making up the cloud. On the other hand, establishing the existence of a 250°K cloud would also be of great importance.

Considering the Earth-based data at 4 mm of Kuzmin and Salomonovich (Ref. 21) and at 4.3 mm of Grant, Corbett, and Gibson (Ref. 22) and the large number of measurements in the vicinity of 8 mm (Refs. 23, 26), it is possible to estimate the value of T_A of the model considered here that is most compatible with these terrestrial data. Assuming that τ goes as $1/\lambda^2$, one readily finds that the predicted integrated dark-side brightness temperature spectrum obtained by assuming a T_A value between 300 and 350°K best fits the data.

It is also instructive to compute the predicted phase angle dependence of the brightness temperature at 19 mm under the assumption that the atmosphere has been removed. In this manner, a comparison with the terrestrial 3.15- and 10-cm phase data can be made. If the surface temperature is assumed to be of the synchronous type (see Eq. 45), then the integrated disc temperature vs phase angle i (angle between the Earth and the Sun as seen from Venus) is given by

$$T_B = \epsilon\left(T_0 + \frac{2}{\pi}\Delta T \cos i\right) \tag{46}$$

For the model with $T_A = 250°K$, $\Delta T = 75°K$, and $\epsilon_r = 3.0$,

$$T_B = 625 + 44 \cos i$$

and for the model with $T_A = 350°K$, $\Delta T = 85°K$, and $\epsilon_r = 4.0$,

$$T_B = 625 + 48 \cos i$$

The above variable factors are to be compared with the 41°K value of Drake at 10 cm (Ref. 27) and the 73°K value of Mayer et al. at 3.15 cm (Ref. 28).

B. Scan 2 Temperature Anomaly

The premature drop in temperature that occurred in both channels toward the end of scan 2 is very pronounced, as can be seen in Figs. 19 and 22. As the fast scan was not activated until after the first data sample of FC 168, the abnormally low readings that occurred after reading 5 of FC 167 cannot be due to a power-switching transient. The effect of such a transient is clearly seen in data line 2 of FC 168. Hence the observed anomaly must have been caused by an apparently lower value of brightness temperature attributable to this region of the planetary disc. As the signal-to-noise ratio in channel 2 was quite marginal, only the data of channel 1 will be discussed.

At the time the first anomalous data sample was made (sample 6, FC 167), the beam spot defined by the 3-db antenna response region was entirely on the planet. The following data point (sample 1, FC 168) refers to the beam spot being ~10% off the planet.

At the time sample 6 of FC 167 was taken, the beam center intersected the planetary surface at close to 69.9 deg south latitude and 15.3 deg west longitude. The terminator line is here assumed to be 0 deg longitude and 0 deg latitude, defined by the great circle that has its plane perpendicular to that of the optical terminator and parallel to the orbital plane of Venus.

The *Mariner* infrared data also exhibited an anomaly towards the end of scan 2 (Ref. 29). The measurement of the infrared temperature distribution across the disc of the planet by Murray et al. (Ref. 30) on December 14 also showed a definite anomalous feature in a region very close to that pertaining to the microwave and *Mariner* infrared anomaly. As thermal maps made before and after the December 14 measurements indicated this feature to be variable, the anomaly is assumed to be a storm zone. With three different instruments detecting the temperature anomaly, its existence appears to have been definitely established. One interesting aspect of the anomaly is that if one assumes that the brightness temperature decreases in a step fashion midway between data points 5 and 6 of FC 167, and if the effects of beam smoothing are included, a brightness temperature level in the anomaly region of ~300 to 350°K fits very well (see Fig. 19).

C. 13.5-mm Temperature

A model atmosphere consisting of only CO_2 and N_2 under high pressure is not capable of matching both the 13.5- and 19-mm data. The simple isothermal-layer model will not fit the data from both channels unless one assumes that the opacity increases more rapidly than as ν^2. It is possible to get a marginal fit if a model consisting of melting ice spheres as suggested by Lilley (Ref. 31) and Deirmendjian (Ref. 32) is assumed. However, for such a model there appears to be conflict with the 4-mm data, since the value of T_B for this model would be too low at this wavelength. Another possibility is that the low 13.5-mm temperature readings are due to line absorption.

In an attempt to match the *Mariner* 13.5-mm data, the simple cloud model, which met with fair success in matching the observed limb-darkening ratios at 19 mm, was modified to include line absorption. In developing and testing this type of model, other data in addition to those obtained from the *Mariner* experiment were considered.

Most of the Earth-based microwave data pertaining to the dark-side brightness temperature of Venus and lying in the wavelength region of 4 to 100 mm are plotted in Fig. 40 (see Refs. 20–28, 34, and 35). The *Mariner* values plotted are extrapolations of the actual data, assuming the cloud model for 19 mm and simply extrapolating the suggested trend of the 13.5-mm data. The *Mariner* plots also show the relatively broad RF bandwidth of the two channels, that of channel 2 strongly affecting any interpretation of the temperature values in terms of the possible existence of line absorption.

A wavelength region of particular interest in Fig. 40 is where $\lambda \leq 19$ mm. As mentioned earlier, the region from 4 to 8 mm suggests the existence of a cloud-type absorber at an effective temperature of 300 to 350°K. However, the 11.8-mm data of Staelin et al. (Ref. 20) and the *Mariner* 13.5-mm data are not compatible with cloud absorption alone and appear to require the presence of a molecule, or molecules, in the Venus atmosphere that exhibit line absorption. In particular, the *Mariner* data would appear to suggest the presence of uncondensed water vapor, although there are a large number of molecules that have resonance lines within the RF passband of the *Mariner* instrument: methyl alcohol, formaldehyde, ketene, isocyanic acid, nitromethane, and sulfur dioxide, to name a few.

There have been several searches for the presence of H_2O in the atmosphere of Venus. Bottema, Plummer, and Strong (Ref. 36) performed measurements in the water vapor band at 1.13 microns. They require 98 microns of precipitable water at atmospheric pressure to match the observed modulation of the spectrum. Using wide-band filter photometry at 1.4 microns, Dollfus (Ref. 37) derived a Cytherean H_2O abundance of 100 microns above the effective reflecting layer. Both results appear to conflict with the results of Spinrad (Ref. 38) unless it is assumed that the measurements at 1 to 1.4 microns refer to a region much deeper in the Venus atmosphere. An upper limit of 100 microns for the amount of precipitable water vapor above some assumed effective reflecting layer is adopted here in the model calculations.

The assumed temperature-vs-height profile of the model atmosphere used in the calculations of this Section

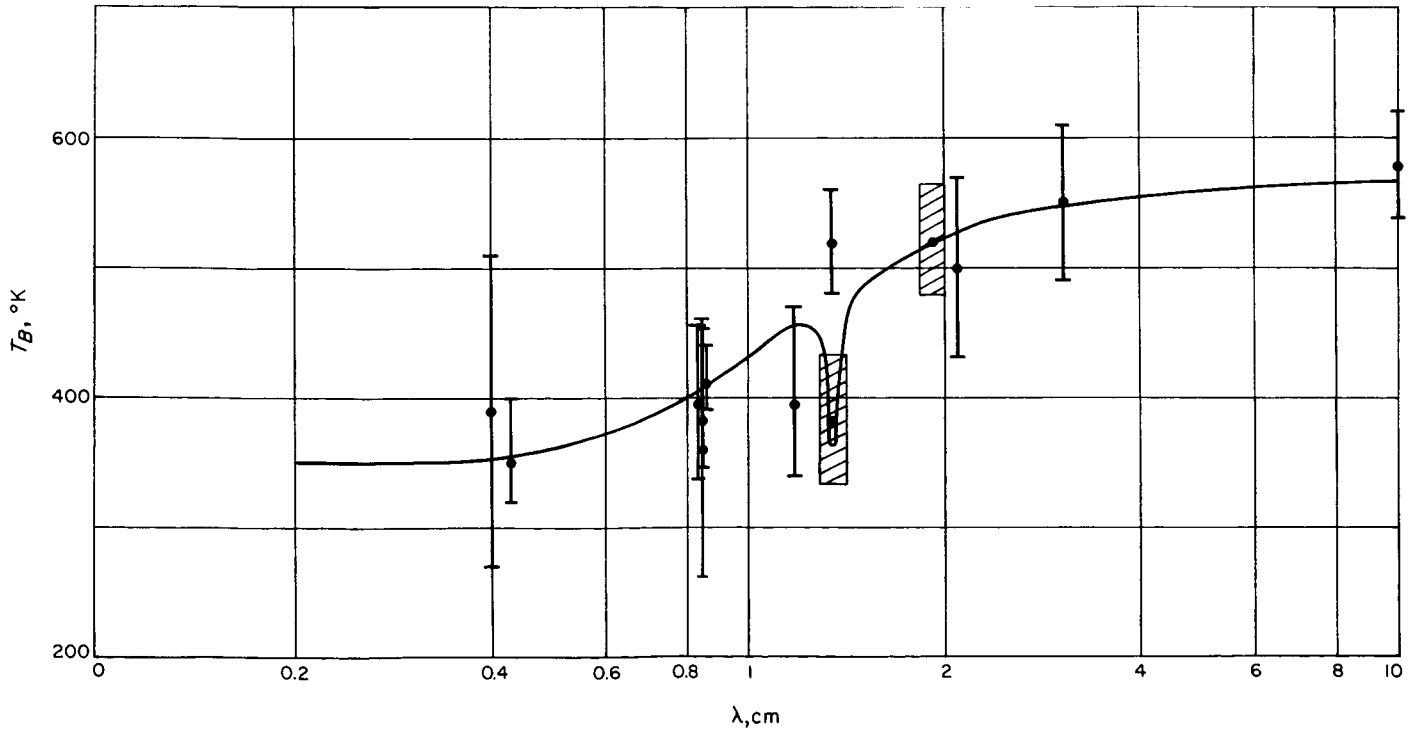

Fig. 40. Venus dark-side disc temperatures and stratified atmosphere

is shown in Fig. 41. In this model it is assumed that there is an isothermal cloud-type layer of unspecified microwave absorber at ~350°K, with the atmosphere being at a constant subadiabatic index ζ of 1.5 both below the cloud and above to the point where the temperature has decreased to about 250°K. From 250 to 200°K, the atmosphere is subadiabatic with an index of $\zeta \sim 3.3$. Above this, the atmosphere is assumed to be in isothermal equilibrium at 200°K. The region with the high subadiabatic index is the region of the upper cloud layer to which the 8- to 14-micron observations (Refs. 2, 3) are assumed to refer. Also, the high value of the subadiabatic index causes the pressure in this upper cloud to decrease fast enough that at some nominal region in the cloud where it might be assumed that the observed 1- to 2-micron radiation originates, the integrated water above this region would yield the observed upper limit of 100 microns.

The constraint of 100 microns of precipitable H_2O required the computation of this parameter for the model described above. The amount of precipitable water vapor above the clouds under one assumed model has been performed by Menzel and Whipple (Ref. 39). A different calculation was performed here in order to be more adaptable to the model under consideration. From the ideal gas law we have, for the water vapor density ρ, with ϵ' the fractional number of H_2O molecules and P the total pressure,

$$\rho = \frac{\epsilon' MP}{R^*T}$$

where M is the mass of H_2O in grams per mole under ideal conditions. For a subadiabatic lapse rate,

$$P = P_0\left(\frac{T}{T_0}\right)^{\zeta\gamma/(\gamma-1)} \tag{47}$$

Hence

$$\rho = \frac{\epsilon'(T)MP_0T^{[(\zeta-1)\gamma+1]/(\gamma-1)}}{R^*T_0^{\zeta\gamma/(\gamma-1)}} \tag{48}$$

For the isothermal region, the mixing ratio is assumed constant. Hence

$$\rho = \frac{\epsilon' M}{RT_{180}} P_b \exp\left[-\eta(H-H_b)\right] \tag{49}$$

where

$$\eta = \frac{R^*T}{Mg}$$

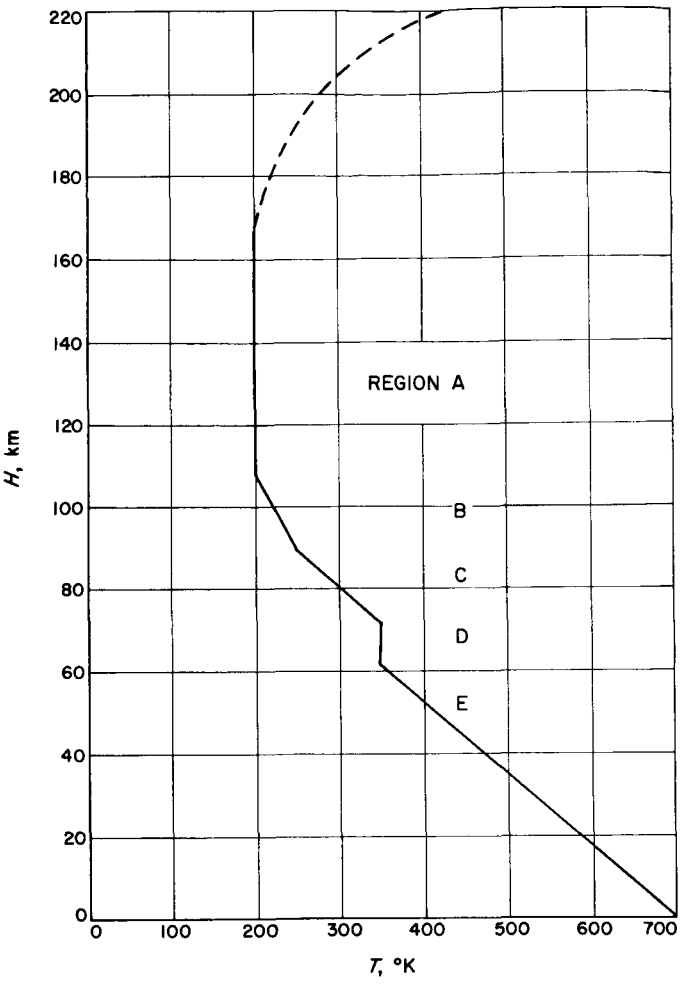

Fig. 41. Temperature profile of multilayer model atmosphere

and where P_b and H_b refer to the base of the isothermal layer. The total integrated water vapor in a column, or the precipitable water, above a layer at a temperature T_0 is then

$$\begin{aligned} S &= \int_{h_0}^{\infty} \rho\, dh \\ &= -\int_{T_0}^{T_b} \frac{\epsilon'(T)MP_0T^{[(\zeta-1)\gamma+1]/(\gamma-1)}}{R^*T_0^{\zeta\gamma/(\gamma-1)}} \frac{\zeta dT}{\beta} \\ &\quad + \int_{H_c}^{\infty} \frac{\epsilon' M}{R^*T_0} P_b \exp\left[\eta(h-H_c)\right] dh \\ &= \int_{T_c}^{T_0} \frac{\epsilon'(T)MP_0T^{[(\zeta-1)\gamma+1]/(\gamma-1)}}{R^*T_0^{\zeta\gamma/\gamma-1}} \frac{\zeta dT}{\beta} + \frac{\epsilon' MP_b}{\eta RT_b} \end{aligned} \tag{50}$$

If the fractional amount of H_2O is low enough, ϵ' will not depend upon T and we have

$$S = \frac{\epsilon' MP_0k}{gmR^*}\left[1 - \left(\frac{T_b}{T_0}\right)^{\zeta\gamma/(\gamma-1)}\right] + \frac{\epsilon' MP_b}{\eta R^*T_b} \tag{51}$$

In some cases, ϵ' could be independent of T to a certain height corresponding to some T_a. From here to T_0 it could be a function of T if at T_a the partial pressure of the H_2O is at the saturation pressure corresponding to T_a. Assuming the latent heat of vaporization to be essentially constant from T_a to T_c, we have for ϵ'

$$\epsilon' = \epsilon'_s = \frac{6.11 \times 10^3}{P} \exp\left[\frac{M\ell}{R^*}\left(\frac{1}{273} - \frac{1}{T}\right)\right] \quad (52)$$

if P is in dynes/cm^2. Hence (letting $x = M\ell/R^*$)

$$\begin{aligned} S &= \frac{\epsilon' MP_0 k}{mgR^*}\left[1 - \left(\frac{T_a}{T_0}\right)^{\zeta\gamma/(\gamma-1)}\right] \\ &\quad + \int_{T_a}^{T_b} \frac{6.11\,M}{R^*T} \exp\left(\frac{1}{273} - \frac{1}{T}\right)\frac{\zeta}{\beta}\,dT \\ &\quad + \frac{\epsilon'_b MP_b}{\eta R^* T_b} \\ &= \frac{\epsilon' MP_0 k}{mgR^*}\left[1 - \left(\frac{T_a}{T_0}\right)^{\zeta\gamma/(\gamma-1)}\right] + \frac{6.11\,M\zeta}{\beta R^*} \\ &\quad \times \left\{\sum_{n=1}^{\infty} \frac{(-1)^n}{n \cdot n!}\left[\left(\frac{\chi}{T_b}\right)^n - \left(\frac{\chi}{T_a}\right)^n\right]\right. \\ &\quad \left. - \left[1 + \exp\left(\frac{\chi}{273}\right)\right] \ln \frac{T_a}{T_b}\right\} + \frac{\epsilon'_b MP_b}{\eta R^* T_b} \end{aligned} \quad (53)$$

In the model assumed in order to explain the microwave brightness temperature spectrum, the fractional amount of H_2O vapor was kept compatible with the saturation vapor pressure corresponding to the temperature at each point in the atmosphere.

The expression for the absorption coefficient due to H_2O is given by (see Barrett and Chung, Ref. 35).

$$\begin{aligned} \alpha_{H_2O} &= \frac{1.05 \times 10^{-28} N\nu^2 \exp(-644/T)}{T^{5/2}} \\ &\quad \times \left[\frac{\Delta\nu}{(\nu-\nu_0)^2 + (\Delta\nu)^2} + \frac{\Delta\nu}{(\nu+\nu_0)^2 + (\Delta\nu)^2}\right] \\ &\quad + 7.60 \times 10^{-52} \frac{N\nu^2 \Delta\nu}{T^{3/2}} \end{aligned} \quad (54)$$

where

$$\Delta\nu = 2.62 \times 10^9 \frac{P/760}{(T/318)^{0.625}}(1 + 0.0046\,\rho) \quad (55)$$

and ρ is the water vapor density in gm/m^3. Here, ρ can be written in terms of the pressure and temperature through the ideal gas law, resulting in

$$\rho = 3.008 \times 10^{-17} \frac{\epsilon' P}{KT}$$

where ϵ', as before, is the fractional number of H_2O molecules, and P is the pressure in dynes/cm^2. The absorption coefficient can be written in terms of the pressure in dynes/cm^2, with the result

$$\begin{aligned} \alpha_{H_2O} &= 7.61 \times 10^{-13} \frac{\epsilon' P\nu^2}{T^{7/2}} \exp(-644/T) \\ &\quad \times \left[\frac{\Delta\nu}{(\nu-\nu_0)^2 + (\Delta\nu)^2} + \frac{\Delta\nu}{(\nu+\nu_0)^2 + (\Delta\nu)^2}\right] \\ &\quad + 5.50 \times 10^{-36} \frac{\epsilon' P\nu^2 \Delta\nu}{T^{5/2}} \end{aligned} \quad (56)$$

$$\Delta\nu = 2.58 \times 10^3 \frac{P}{(T/318)^{0.625}}\left(1 + 1.384 \times 10^{-19} \frac{\epsilon' P}{KT}\right) \quad (57)$$

For this calculation the atmosphere was divided into layers of constant temperature and pressure. In general, if the atmospheric temperature of level i is the brightness temperature of T_i, this level would be

$$T_{A_i} = T_i\left[1 - \exp(-\alpha_i^* \Delta x_i)\right] \quad (58)$$

Since this contribution is attenuated by the layers above, there results

$$T_{A_i} = T_i\left[1 - \exp(-\alpha_i^* \Delta x_i)\right] \exp\left(-\sum_{j=0}^{i-1} \alpha_i^* \Delta x_i\right) \quad (59)$$

and adding the contributions of all layers gives

$$T_A = \sum_i T_i\left[1 - \exp(-\alpha_i^* \Delta h_i \delta)\right] \exp\left(-\sum_{j=0}^{i-1} \alpha_i^* \Delta h_i \delta\right) \quad (60)$$

If the surface contribution is included, there results for this model (see Fig. 41)

$$
\begin{aligned}
T_B = {} & \epsilon' T_s \exp\left[-(\tau_a + \tau_b + \tau_c + \tau_d + \tau_e)\delta\right] \\
& + \left\{T_a\left[1 - \exp(-\alpha^*_{a_o}\Delta h_a\delta)\right] + T_a\sum_{i=1}^{m}\left[1 - \exp(-\alpha^*_{a_i}\Delta h_a\delta)\right]\exp\left(-\sum_{j=0}^{i-1}\alpha^*_{a_j}\Delta h_a\delta\right)\right\} \\
& + \left\{T_{b_o}\left[1 - \exp(-\alpha^*_{b_o}\Delta h_b\delta)\right] + \sum_{i=1}^{n} T_{b_i}\left[1 - \exp(-\alpha^*_{b_i}\Delta h_b\delta)\right]\exp\left(-\sum_{j=0}^{i-1}\alpha^*_{b_j}\Delta h_a\delta\right)\right\}\exp(-\tau_a\delta) \\
& + \left\{T_{c_o}\left[1 - \exp(-\alpha^*_{c_o}\Delta h_c\delta)\right] + \sum_{i=1}^{p} T_{c_i}\left[1 - \exp(-\alpha^*_{c_i}\Delta h_c\delta)\right]\exp\left(-\sum_{j=0}^{i-1}\alpha^*_{c_j}\Delta h_c\delta\right)\right\}\exp\left[-(\tau_a+\tau_b)\delta\right] \\
& + \left\{T_d\left[1 - \exp(-\alpha^*_{d_o}\Delta h_d\delta)\right] + T_d\sum_{i=1}^{q}\left[1 - \exp(-\alpha^*_{d_i}\Delta h_d\delta)\right]\exp\left(-\sum_{j=0}^{i-1}\alpha^*_{d_j}\Delta h_d\delta\right)\right\}\exp\left[-(\tau_a + \tau_b + \tau_c)\delta\right] \\
& + \left\{T_{e_o}\left[1 - \exp(-\alpha^*_{e_o}\Delta h_e\delta)\right] + \sum_{i=1}^{r} T_{e_i}\left[1 - \exp(-\alpha^*_{e_i}\Delta h_e\delta)\right]\exp\left(-\sum_{j=0}^{i-1}\alpha^*_{e_j}\Delta h_e\delta\right)\right\} \\
& \times \exp\left[-(\tau_a + \tau_b + \tau_c + \tau_d)\delta\right] + T_R
\end{aligned}
\tag{61}
$$

where we are using an averaged curvature correction δ (see Appendix C) given by

$$
\delta = \frac{\sqrt{R_p^2\cos^2\theta + 2R_p H_a + H_a^2} - R_p\cos\theta}{H_a}
$$

also

$$
\tau_a = \sum_{i=0}^{m}\alpha^*_{a_i}\Delta h_a
$$

$$
\tau_b = \sum_{i=0}^{n}\alpha^*_{b_i}\Delta h_b
$$

$$
\tau_c = \sum_{i=0}^{p}\alpha^*_{c_i}\Delta h_c
$$

$$
\tau_d = \sum_{i=0}^{q}\alpha^*_{d_i}\Delta h_d
$$

$$
\tau_e = \sum_{i=0}^{r}\alpha^*_{e_i}\Delta h_e
$$

The specific parameters and equations used that are pertinent to the various regions of the model assumed here are given in Appendix C.

If one assumes that the results of Bottema et al. apply to a column above a point where the atmosphere is at least 210°K, then the maximum fractional number of uncondensed H_2O molecules for this model is $\sim 2 \times 10^{-3}$ (with $P_s = 10$ atmospheres) for 100 microns of precipitable water. The integrated disc dark-side brightness temperature spectrum for this model is shown in Fig. 40. The predicted temperature integrated over the channel 2 bandwidth and referred to the center of scan 2 for this model is 480°K, which is considerably higher than the measured value of 390°K.

The assumed amount of water was then increased to the point where the predicted value of T_B related to the center of scan 2 was 390°K, in order to compare the theoretical limb-darkening ratios with the measured values. The predicted ratios were clearly too small, yielding, for example, a value of ~ 0.78 for r_{32}, assuming a rough surface and a surface temperature distribution of the form $T_s = 700°\text{K} + 85°\text{K}\cos\phi$. The amount of precipitable water for this model above the 210°K layer is $\sim$200 microns. Hence both the measured limb-darkening ratios and the precipitable water value are incompatible with the assumption that the low channel 2 temperatures are due only to water vapor line absorption.

It is clear that if the precipitable water assumed for this model is kept compatible with the results of Bottema et al., Dollfus, and Spinrad (the former groups seeing effectively almost to the surface of the planet), the 11.8- and *Mariner* 13.5-mm results require a different microwave line absorber. In this regard, the measurement of Gibson at 13.5 mm (Ref. 40) is of interest. At first glance one might assume that the *Mariner* channel 2 results are in direct conflict with the much higher value of 520 ±40°K quoted by Gibson. However, the preceding discussion regarding the model considered in this Section leads one to consider absorption lines due to molecules other than H_2O. For example, if one recalls the rela-

tively broad RF bandwidth of channel 2 of ~2.5 Gc in comparison with the value of 11 Mc for Gibson's instrument, a model that includes the beginning of strong line absorption just short of 13.5 mm can explain the wavelengths and observations considered specifically here. This suggests the presence of organic molecules in the atmosphere of Venus, although other molecules exhibit lines in this region of the spectrum (Barrett, Ref. 41).

D. Cloud-Type Absorber

Kaplan (Ref. 42) first suggested the possible existence of a higher-temperature cloud layer as a result of his re-analysis of the Adams and Dunham spectra analyzed by Spinrad (Ref. 33). His analysis led to the discovery of two sharp Boltzmann rotational maxima, one corresponding to about 300°K and the other to about 700°K, a finding that implies a stratified cloud layer at a level corresponding to a temperature of about 350°K. He pointed out that this implies molecules with CH bands, and, since these absorb strongly at around 3.5 microns, the required efficient greenhouse effect appears to be easily possible.

In the analysis of this Section it has been found that the ratios of the peak values of the three scans at 19 mm require a cloud-type absorber at a temperature of between 250 and 350°K. The good fit that one obtains to the 4- and 8-mm data by a 300 to 350°K cloud discussed earlier is of interest in this regard. Also, as noted earlier, the anomaly that occurred in scan 2 at 19 mm can be explained by a step change in brightness temperature to a value of 300 to 350°K, which could be interpreted to mean that the clouds associated with the apparent storm zone were becoming more opaque. The possibility of line absorption suggested by the 8-, 11.8-, and 13.5-mm data is, of course, compatible with the suggestion of Kaplan regarding the cloud.

The peak temperature ratios measured by channel 2 are also of interest here (see Table 5). As noted previously in Section VI-C, increasing the fractional amount of uncondensed water vapor until the peak scan 2 temperature is matched not only predicts a degree of limb-darkening that is much greater than that which was measured, but also results in an amount of precipitable water that is clearly too high. An estimated upper limit of the fractional number of water vapor molecules that would be allowed, based upon the channel 2 limb-darkening ratios and associated probable errors alone, is of the order of 1×10^{-3}. An interpretation of both the measured limb-darkening ratios and brightness temperature values observed at 13.5 mm is that the molecules that are creating the line absorption at $\lambda \leq 13.5$ mm must be essentially condensing out in the region of the atmosphere where $T \geq 350°K$ in such a manner that absorption by the vapor form of the molecule is creating negligible absorption at points in the atmosphere where $T < 350°K$.

Since there appeared to be fairly substantial evidence suggesting the existence of a microwave-absorbing cloud layer at 300 to 350°K, it was instructive to consider the possible existence of such a cloud to the extent of determining what general types of molecules might be producing it. Two constraints that the substance or substances comprising the cloud must satisfy are that they condense or polymerize in the vicinity of 300 to 350°K and that the dielectric coefficient of the cloud droplets or particles must be such that microwave energy will be absorbed. Another constraint suggested by the 13.5-mm limb-darkening ratios is, of course, that some of the condensing or polymerizing molecules also exhibit line absorption when in the vapor state. A condensation cloud was considered here.

Some information regarding the probable types of molecules required if a condensation cloud is assumed can be obtained from the expression for the saturation vapor pressure of gas, namely

$$P_c = P_0 \exp\left[\frac{M\ell}{R^*}\left(\frac{1}{T_0} - \frac{1}{T}\right)\right] \tag{62}$$

which is merely an integration of the Clausius–Clapeyron equation assuming that ℓ, the latent heat of evaporation, is constant throughout the temperature range of interest, where M is the molecular mass per mole, R^* the universal gas constant, and P_0 the vapor pressure of the gas at some temperature T_0. If the fractional number of organic molecules being considered is ϵ', then

$$P_c = \epsilon' P_T = P_0 \exp\left[\frac{M\ell}{R^*}\left(\frac{1}{T_0} - \frac{1}{T}\right)\right] \tag{63}$$

Now for condensation to occur we need

$$\epsilon' P_T > P_0 \exp\left[\frac{M\ell}{R^*}\left(\frac{1}{T_0} - \frac{1}{T}\right)\right] \tag{64}$$

or

$$\ln = \frac{P_0}{\epsilon' P_T} < \frac{M\ell}{R^*}\left(\frac{1}{T} - \frac{1}{T_0}\right) \tag{65}$$

Choosing $P_0 = 1$ atmosphere, then

$$\ln = \frac{1}{\epsilon' P_T} < \frac{M\ell}{R^*}\left(\frac{1}{T} - \frac{1}{T_0}\right) \tag{66}$$

One can compute the required surface pressures for various organic molecules for an assumed adiabatic lapse rate or a subadiabatic lapse rate with a subadiabatic index of 1.5. The results for a number of molecules are tabulated in Table 7. The values for ℓ and T_0 were obtained from the *Handbook of Chemistry and Physics*, 38th edition (The Chemical Rubber Publishing Co.) and the *National Bureau of Standards Circular 500*. A model atmosphere of 5% CO_2 and 95% N_2 was assumed.

It is clear that if the cloud is a condensation cloud, then very heavy, complex molecules are required if reasonable pressures are assumed. Based upon the 12.5-cm radar observations, Thaddeus (Ref. 43) has computed an upper limit of ~240 atmospheres for the surface pressure, assuming an atmosphere containing 5% CO_2. As seen in Table 7, this value of surface pressure requires fairly complex organic molecules even if an adiabatic lapse rate is assumed. Other estimates of the surface pressure have placed it at much lower values (Ref. 44).

As mentioned previously, an additional constraint on the cloud material is that of the ability to absorb microwave energy. If the cloud particle size is small (i.e., $\xi = 2\pi a'/\lambda$ is small, where a' is the particle radius and λ the wavelength) then the expression for the absorption cross section Q (Ref. 45) is given by

$$Q = \frac{\lambda}{2\pi}\xi^2(C_1 + C_2\xi^2 + C_3\xi^3) \tag{67}$$

where

$$C_1 = \frac{6\epsilon_i}{(\epsilon_r + 2)^2 + \epsilon_i^2} \tag{68}$$

$$C_2 = \frac{\epsilon_i}{15}\left[\frac{3(7\epsilon_r^2 + 4\epsilon_r - 20 + 7\epsilon_i^2)}{\left[(\epsilon_r + 2)^2 + \epsilon_i^2\right]^2} + \frac{25}{(2\epsilon_r + 3)^2 + 4\epsilon_i^2} + 1\right] \tag{69}$$

$$C_3 = \frac{(\epsilon_r - 1)^2(\epsilon_r + 2)^2 + \epsilon_i^2\left[2(\epsilon_r - 1)(\epsilon_r + 2) - 9\right] + \epsilon_i^4}{\left[(\epsilon_r + 2)^2 + \epsilon_i^2\right]} \tag{70}$$

In order for a cloud of solid particles to attenuate microwave radiation from the surface sufficiently, an extremely dense cloud is required, since ϵ_i is usually much smaller than ϵ_r in solids. However, for liquids, ϵ_i can be comparable to ϵ_r, particularly if the critical wavelength of the substance lies in the wavelength region of interest. This would result in a cloud of reasonable density or total liquid content. Many organic molecules have critical wavelengths in the centimeter region (Ref. 46) and many of these may have the required characteristics for condensation.

A more likely possibility is that the cloud consists of liquid polymers. One would strongly suspect that in such a form the molecule would be a more efficient microwave absorber than in the monomeric form. A polymer cloud would not impose the serious constraint involving extreme surface pressures that the condensation cloud does.

Table 7. Required surface pressure for condensation cloud

Molecule	M, g/mole	ℓ, cal/g	T_0, °K	Surface pressure, atmospheres			
				T_c = 300° K		T_c = 350° K	
				ζ = 1.0	ζ = 1.5	ζ = 1.0	ζ = 1.5
		At 15° C					
Methyl alcohol	32	262.8	337.7	440	2000	1835	6320
Acetonitrile	41	174	354.8	364	1670	1043	3600
Formic acid	46	120	373.6	361	1650	729	2505
Nitromethane	61	135	374.2	144	658	732	2520
Ethanol	46	204	351.4	252	1150	1200	4140
Allyl alcohol	58	163	370	112	510	560	1930
Propionic acid	74	98.8	414.1	75	344	238	819
Acetic anhydride	102	92.2	412.6	31	142	150	515
Butyric acid	88	114	436.5	12	55	69	235
Butyl alcohol	74	141	390.5	36	165	420	1450
p-. Anethole	148	71	508	1.3	6.1	12	42
Carvacarol	152	68	510	1.7	7.9	11	38
p-. Cymene	136	68	450	12.7	58	62	214
		At 25° C					
Pentane	72	87.5	309	1620.6	7400	4368	15033
Hexane	86	87.5	341.7	451.1	2060	1632	5617
Heptane	100	87.2	371.4	116.1	530	576	1982
Octane	114	86.8	398.6	30.7	140	204	702
Nonane	128	86.5	423.8	7.3	33	64.8	223

VII. SUMMARY AND RECOMMENDED PROGRAMS

In this Section the results of the analysis of the preceding Sections are summarized. Several types of observational and research programs are also suggested.

A large portion of the results of this analysis was presented at the session on Planetary Emissions of the Third Western National Meeting of the American Geophysical Union, held at Boulder, Colorado, December 28, 1963 (Ref. 47). Preliminary results regarding the isothermal layer and specular surface were presented in a lecture at Philadelphia, Pennsylvania, May 21, 1963, as part of the lecture series, "Space Age Technology."

A. Summary

The three scans of the planet Venus obtained by the microwave radiometer aboard the *Mariner II* spacecraft exhibited a strong limb-darkening effect at 19 mm and very little, if any, at 13.5 mm. Analysis of the degree of limb-darkening at 19 mm results in the conclusion that a hot surface emitting specularly in combination with a nearly isothermal or cloud-type layer at 250 to 350°K more closely matches the data than other model atmospheres studied. A consideration of the terrestrial 4.3- and 8- to 8.6-mm data results in a more likely temperature for the cloud of 300 to 350°K. Additional support for the existence of such a cloud layer is indicated by the anomaly detected toward the end of scan 2. Such a cloud strongly suggests the presence of heavy hydrocarbons or complex organic molecules as proposed originally by Kaplan (Ref. 42) to explain the two rotational maxima observed in the spectra obtained by Adams and Dunham.

The formulation of a model yielding an upper limit to the fractional number of water vapor molecules consistent with 100 microns of precipitable water is inadequate to predict the low temperatures observed at 13.5 mm, whereas increasing the fractional amount of H_2O until a match to the scan 2 temperature is obtained results in limb-darkening ratios that markedly disagree with the measured values. A small fractional number of water molecules can exist in the atmosphere of Venus, but another microwave absorber of the type that exhibits strong line absorption in the region from ~21.0 to 23.5 Gc and that condenses or polymerizes at $T \geq 350°K$ is required. Since a condensation cloud requires extreme surface pressures, it is more likely that the cloud is composed of liquid polymers.

The specular-type surface that best fits the data is one with a dielectric constant of between 3 and 4 which is in good agreement with the value of ~3.5 obtained by Muhleman (Ref. 48) utilizing the radar data. Since the presence of high-pressure CO_2 tends to decrease the resultant limb-darkening of a specular surface in combination with a cloud-type absorber of lower temperature, it is unlikely that the surface pressure can be very high. An upper limit of about 100 atmospheres for an atmosphere containing 20% CO_2 and an adiabatic lapse rate is obtained. Allowance for subadiabaticity decreases the maximum surface pressure.

Under the assumption of a synchronous-type surface-temperature distribution, the 19-mm data lead to an equation of the form

$$T_s = 700°K + (80 \pm 5)°K \cos \phi$$

for the 250 to 350°K cloud-layer model. The number and precision of those scans obtained were not sufficient to detect any shift in the surface minimum with respect to the anti-subsolar point.

B. Recommended Programs

The *Mariner* results suggest several specific research and observational programs that are required to further increase our knowledge of the planet. These include laboratory and theoretical studies, Venus observational programs, and probe experiments.

The indicated abruptness in the spectrum predicts the presence of absorption lines suggesting a very fruitful measurement program involving the search for lines in the vicinity of 13.5 mm and shorter. As the atmosphere appears to be opaque at wavelengths shorter than 8 mm, the most fruitful search region would appear to be between 8 and 15 mm. Such a program should yield information of considerable worth in regard to establishing the existence of molecules other than CO_2 in the atmosphere of Venus, and particularly, should shed light on the identity of the molecule or molecules that are apparently forming the liquid polymer cloud at $T \sim 350°K$. If there are a large number of absorption lines, it may be that pressure broadening and the signal-to-noise ratios one must contend with in a terrestrially based observation program may well require a multichannel or sweeping radiometer aboard a flyby probe for positive identification.

A comprehensive study of the dielectric properties of liquid polymers that form in the vicinity of 350°K is needed. This may require the measurement of the dielectric properties of some polymers. Laboratory microwave spectral line measurements should also be made. Such a program, serving as a backup to the line search program suggested above, should allow the identification of some of the molecules comprising the cloud and lower atmosphere.

Verification of the existence and temperature range of the cloud layer suggested by the *Mariner* results is of great importance because of the implications regarding heavy organic molecules mentioned previously. Further analysis similar to that of Kaplan (Ref. 42) in the 8000 Å region will certainly shed more light in this regard. As the constraint of being a microwave absorber is an important one, verification of this characteristic of the cloud layer is necessary. Even if sufficiently high-resolution measurements in the microwave region utilizing extensive interferometric arrays become possible, a direct microwave experiment involving an atmosphere entry capsule is desirable.

An experiment involving the detection and measurement of some of the pertinent parameters of a microwave-absorbing cloud was conceived shortly after a paper was presented by Sagan (Ref. 49) in which a liquid-water cloud model for Venus was postulated. In view of the results of the *Mariner II* data, serious consideration should be given to an experiment that would consist of the placement of a simple crystal video microwave radiometer on a parachute-borne Venus entry capsule. Since the wavelength of operation would be 4 mm (here, the integrated opacity of the suggested 350°K cloud would be about 3) the instrumentation involved could be very small and light and could require low power and sample rates.

If the contributions to the brightness temperature of the microwave absorbers other than the cloud are neglected, and if we consider a radiometer switching between upward- and downward-pointing narrow-beamwidth horns, the resultant signal will be proportional to

$$T_B = T_c \left(e^{-\alpha^* x} - e^{-\alpha^*(t^*-x)}\right) + \epsilon T_s\, e^{-\alpha^*(t^*-x)} \qquad (71)$$

where we have assumed a uniform, isothermal cloud of absorption α^* per km for simplicity, where t^* is the cloud thickness and x is the distance the radiometer penetrates the cloud as measured from the cloud top. A study of this "input-switched" mode shows several cloud-detectability criteria. For example, T_B measured prior to entering the cloud could be compared with T_B after having passed through. One finds that the minimum value of T_B obtained while the radiometer is in the cloud compared with the value of T_B either before or after the cloud has been entered is very sensitive to α^*. Denoting $\Delta T_{\max}$ as the difference between the value of T_B obtained after passage through the cloud and the minimum T_B in the cloud, it can readily be shown for the simplified model under discussion that $\Delta T_{\max}$ is given by

$$\Delta T_{\max} = \epsilon T_s - T_c \left[1 - \exp\left(-\alpha^* t^*\right)\right] - 2\sqrt{T_c(\epsilon T_s - T_c)}\exp\left(-\frac{\alpha^* t^*}{2}\right) \qquad (72)$$

One finds that if $\Delta T_{\max}$ is to be used to establish a value for α of the cloud with any certainty, τ must be less than about 9. The limiting value of α^*, of course, depends upon the sensitivity of the radiometer (which is dependent upon how fast samples must be taken) and upon the accuracy required in the determination of α^*. The resulting expression for the allowed value of ΔT_{rms} of the radiometer is

$$\Delta T_{\text{rms}} \cong t^* \times \left[\sqrt{T_c(\epsilon T_s - T_c)}\exp\left(-\frac{\alpha^* t^*}{2}\right) - T_c \exp\left(-\alpha^* t^*\right)\right]\Delta\alpha^* \qquad (73)$$

For $\alpha^* = 0.7$/km, $t^* = 4$ km, and $\Delta\alpha^* = 0.1$/km, we have $\Delta T_{\text{rms}} \sim 21$°K. This is well within the state of the art for a simple crystal video-type radiometer, considering the time constant values one could use. The cloud model used in the computations, of course, has been considerably simplified. If absorption by high-pressure CO_2 is allowed, for example, the problem becomes much more complex.

The apparent smoothness of the surface at 19 mm needs further verification. A comparison of the radar characteristics of the Moon and Venus at shorter wavelengths would be helpful in this regard, although utilization of the Earth itself as a target for air- and satellite-borne radiometers would yield more reliable quantitative results. The latter program is essential if future planetary flyby and orbiter missions are to be optimized.

NOMENCLATURE

$A(\theta,\phi)$ effective area of receiving antenna

a defined by Eq.(B-12)

a' particle radius

b a constant relating the antenna beamwidth to the width of the $\sin^2 x/x^2$ function

c velocity of light

C_1,C_2,C_3 defined by Eqs. (67) through (69)

C_p specific heat at constant pressure of gas

d defined in Fig. 14

D_1, D_2 deflections at outputs of radiometers 1 and 2 respectively, when alternately looking at cold sky and at the absorber disc

D'_1, D'_2 deflections at outputs of radiometers 1 and 2 respectively as noise radiator is turned on and off

F noise figure of audio amplifier

g acceleration due to gravity

$G(\theta,\phi,\nu)$ gain of receiving antenna

h defined in Fig. 14

H defined in Eq. (38)

H_s height above the hard surface of Venus

H_a height of top of atmospheric region A above hard surface of Venus (see Fig. 41)

H_b height of top of atmospheric region B above the hard surface of Venus, or base of region A (isothermal region)

i phase angle; angle between the Earth and the Sun, as seen from Venus

I_D defined by Eq. (39)

I_ν defined by Eq. (35)

j $= \sqrt{-1}$

k Boltzmann constant

k' a factor (see Table 5 and Appendix A)

k^* $= \Delta T/\Delta\nu$

l latent heat of evaporation

M molecular mass per mole, in grams

m average mass of atom in atmosphere, in grams

M_c crystal figure of merit

N number of molecules of H_2O per cm^3

P pressure

P_0 vapor pressure of a gas at some temperature T

P_a,P_b,P_c pressure of the atmosphere at levels A,B,C. (P_c also refers to the atmospheric pressure at the base of the 235°K isothermal layer.)

P_s assumed surface pressure of Venus in terrestrial atmospheres

P_T total pressure

P^* received power at detector due to source of brightness temperature T

P^*_{cal} power change due to the internal calibration noise tube being turned on

P^*_D power change caused by scanning the radiometer from sky to the absorber disc

P^*_V power change caused by scanning from cold space to the planet Venus

Q defined by Eqs. (38)

R^* universal gas constant

r defined in Fig. 53

R_p radius of Venus (to the hard surface)

RC output time constant

s defined by Fig. 14

s^* sample deviation

T total waveform time base

t time

t^* cloud thickness

ΔT_A antenna temperature of planet

T_A assumed atmospheric layer temperature

T_B brightness temperature

t_0 time to increase from $V = 0$ to $V = V_0$

T_a,T_b,T_c temperature of the atmosphere at levels A,B,C. (T_c also refers to the temperature of the isothermal layer above the clouds, in the simple model.)

NOMENCLATURE (Cont'd)

T_{cal} effective antenna temperature of calibration signal

T_D brightness temperature of the absorber disc

T'_D $= [T_D - T_{sky}(\theta, \phi, \nu)]$

T_{grnd} brightness temperature of the ground

$T_{iso} = T_i$ assumed temperature of the ith isothermal region of the model atmosphere

T_N effective brightness temperature of the noise radiator

T_R reflected atmospheric radiation

ΔT_{rms} minimum detectable rms change in antenna temperature

T_s temperature of the hard surface of the planet

T_{sky} brightness temperature of the sky

T_{space} brightness temperature of space

T_{Sun} brightness temperature of the Sun

T_V assumed brightness temperature of Venus

T'_V $= [T_V(\theta, \phi, \nu) - T_{space}(\theta, \phi, \nu)]$

$U(t)$ Heaviside function

V_0 peak value of the assumed trapezoidal voltage

ΔV_{cal} voltage change at output due to excitation of internal calibration noise tube

ΔV_{disc} voltage change at output due to moving radiometer from cold sky to the absorber disc

V_{in} input voltage to RC circuit

V_{out} output voltage of RC circuit

V_{PE} preplanet voltage probable error due to the combined effects of noise and the finite analog-to-digital window width

V_{p-p} peak-to-peak voltage error

ΔV_{rms} rms noise voltage at the radiometer output

$V(t)$ voltage output of an RC circuit if the input voltage is $V_0(t)$

x distance the radiometer penetrates the cloud

x_{i_d} measured voltage value at time of data point

x_{i_t} theoretical value at time of data point

$x(t)$ assumed input waveform to an RC integrator

$X(j\omega)$ assumed complex input signal to circuit

$y(t)$ output waveform of RC integrator

$Y(j\omega)$ assumed complex output signal from circuit

Z_c impedance of the capacitor in the integrator circuit

α circuit parameter converting antenna temperature into voltage

α^* absorption per km

β_D ratio of the absorber disc deflection to that of the internal noise tube

β_{Sun} ratio of the output deflection caused by scanning the Sun to that of the internal noise tube

β'_{Sun} ratio for the Sun corrected for noise tube changes in the instrument prior to final calibration

β_V ratio of the output deflection caused by scanning Venus to that of the internal noise tube

γ ratio of specific heats

γ^* the ratio β_V/β_D, etc.

γ'_h bistatic scattering coefficient, horizontal polarization

γ'_v bistatic scattering coefficient, vertical polarization

δ atmospheric absorption path length factor

ϵ emissivity of the surface

ϵ' the fractional number of molecules being considered

ϵ_d emissivity of a perfectly diffuse surface

$\epsilon_d T_s$ surface brightness temperature

ϵ_h horizontally polarized emissivity

ϵ_i imaginary component of the complex dielectric coefficient of the surface material

ϵ_{pd} emissivity for the predominantly diffuse case

ϵ_r real component of the complex dielectric coefficient of the surface material

ϵ_v vertically polarized emissivity

NOMENCLATURE (Cont'd)

ζ subadiabatic index of atmosphere

η the near field antenna correction factor

θ, ϕ conventional polar and azimuthal angles

λ wavelength

ν frequency

ν_{cal} effective prediction bandwidth of calibration signal

ξ the parameter 2π a′/λ, where (a') is the particle radius and λ is the wavelength

ρ water vapor density

σ variance

τ integrated opacity of a microwave-absorbing layer

τ_c integrated opacity of the atmosphere down to some point above the cloud tops

τ'_c integrated opacity of the atmosphere down to the cloud tops

χ noise tube–standard gain horn coupling factor

ψ parameter defined by Eq. (B-21)

ω angular frequency

Ω solid angle

Ω_D, Ω_N solid angles of the absorber disc and the noise radiator respectively

Ω_s solid angle subtended by the atmosphere at the surface

Ω_{Sun} solid angle subtended by the Sun at the Earth

Ω_{sky} solid angle subtended by the unobstructed terrestrial sky

Ω_V solid angle subtended by the planet Venus at the spacecraft

REFERENCES

1. Mayer, C. H., McCullough, T. P., and Sloanaker, R. M., "Observations of Venus at 3.15-cm Wave Length," *The Astrophysical Journal,* Vol. 127, No. 1, January 1958, pp. 1–10.
2. Pettit, E., and Nicholson, S. B., "Temperatures on the Bright and Dark Sides of Venus," *Publications of the Astronomical Society of the Pacific,* Vol. 67, No. 398, October 1955, pp. 293–303.
3. Sinton, W. M., and Strong, J., "Radiometric Observations of Venus," *The Astrophysical Journal,* Vol. 131, No. 2, March 1960, pp. 470–490.
4. Chamberlain, J. W., and Kuiper, G. P., "Rotational Temperature and Phase Variation of the Carbon Dioxide Bands of Venus," *The Astrophysical Journal,* Vol. 124, No. 2, September 1956, pp. 399–405.
5. Barrett, A. H., "Microwave Absorption and Emission in the Atmosphere of Venus," *The Astrophysical Journal,* Vol. 133, No. 1, January 1961, pp. 281–293.
6. Öpik, E. J., "The Surface Conditions on Venus," *The Irish Astronomical Journal,* Vol. 4, No. 2, June 1956, pp. 37–47.
7. Sagan, C., Abstract of paper presented at the AAS meeting in Pittsburgh, Pa., April 18–21, 1960.
8. Sagan, C., *The Radiation Balance of Venus,* Technical Report No. 32-34, Jet Propulsion Laboratory, Pasadena, Calif., September 15, 1960.
9. Sagan, C., "Structure of the Lower Atmosphere of Venus," *Icarus,* Vol. 1, No. 2, September 1962, pp. 151–169.
10. Jones, D. E., "The Microwave Temperature of Venus," *Planetary and Space Science,* Vol. 5, 1961, pp. 166–167.
11. Tolbert, C. W., and Straiton, A. W., "A Consideration of Microwave Radiation Associated with Particles in the Atmosphere of Venus," *Journal of Geophysical Research,* Vol. 67, No. 5, May 1962, pp. 1741–1744.
12. Scharf, F. L., Report No. 9990-6135-TUOOO, Space Technology Laboratories, Redondo Beach, Calif., 1962.
13. Scharf, F. L., "Plasma Instability and the Microwave Radiation from Venus," *Journal of Geophysical Research,* Vol. 68, No. 1, January 1, 1963, pp. 141–146.
14. Roberts, J. A., "Radio Emission from the Planets," *Planetary and Space Science,* Vol. 11, March 1963, pp. 221–260.
15. Barrett, A. H., Copeland, J., Jones, D. E., and Lilley, A. E., *Objectives of the Mariner Venus Microwave Radiometer Experiment,* Technical Report No. 32-156, Jet Propulsion Laboratory, Pasadena, California, August 22, 1961.
16. Barath, F. T., Barrett, A. H., Copeland, J., Jones, D. E., and Lilley, A. E., "Mariner 2 Microwave Radiometer Experiment and Results," *The Astronomical Journal,* Vol. 69, No. 1, February 1964, pp. 49–58.
17. Copeland, J., Dozier, J. B., Jr., and Whitehurst, R., *A Crystal-Audio Radiometer Analysis,* University of Alabama, Physics Department, Radio Astronomy Laboratory Interim International Technical Report No. 2, February 20, 1957.

REFERENCES (Cont'd)

18. Kellner, M. L., and Renger, H. L., unpublished internal report, Jet Propulsion Laboratory, Pasadena, Calif., 1962.

19. Seeger, C. L., Westerhout, G., and van de Hulst, H. C., "The Flux Densities of Some Radio Sources at 400 Mc/s," *Bulletin of the Astronomical Institute of the Netherlands*, Vol. 13, 1956, pp. 89–99.

20. Staelin, D. H., Barrett, A. H., and Kusse, B. R., "Observations of Venus, the Sun, Moon, and Taurus A at 1.18-cm Wavelength," *The Astronomical Journal*, Vol. 69, No. 1, February 1964, pp. 69–71.

21. Kuzmin, A. D., and Salomonovich, A. E., *Izvestia-Radio Physics*, Vol. 4, 1961, p. 573.

22. Grant, C. R., Corbett, H. H., and Gibson, J. E., "Measurements of the 4.3-mm Radiation of Venus," *The Astrophysical Journal*, Vol. 137, No. 2, February 15, 1963, pp. 620–627.

23. Gibson, J. E., "The Brightness Temperature of Venus at 8.6 mm," *The Astrophysical Journal, Vol.* 137, No. 2, February 15, 1939, pp. 611–619.

24. Copeland, J., Ewen Knight Corp., East Natick, Mass. Private communication, 1963.

25. Lynn, V. L., Meeks, M. L., and Sohigian, M. D., "Observations of Venus, the Region of Taurus A, and the Moon at 8.5-Millimeter Wavelength," *The Astronomical Journal*, Vol. 69, No. 1, February 1964, pp. 65–67.

26. Thornton, D. D., and Welch, W. J., "Radio Emission from Venus at 8.35 mm," *The Astronomical Journal*, Vol. 69, No. 1, February 1964, pp. 71–72.

27. Drake, F. D., "Microwave Observations of Venus, 1962–1963," *The Astronomical Journal*, Vol. 69, No. 1, February 1964, pp. 62–64.

28. Mayer, C. H., McCullough, T. P., and Sloanaker, R. M., "3.5 cm Observations of Venus in 1961," *Proceedings of the Eleventh International Astrophysical Symposium*, Liège, Belgium, July 9–12, 1962, pp. 357–363.

29. Chase, S. C., Kaplan, L. D., and Neugebauer, G., "The Mariner 2 Infrared Radiometer Experiment," *Journal of Geophysical Research*, Vol. 68, No. 22, November 15, 1963, pp. 6157–6169.

30. Murray, B. C., Wildey, R. L., and Westphal, J. A., "Infrared Photometric Mapping of Venus through the 8- to 14-Micron Atmospheric Window," *Journal of Geophysical Research*, Vol. 68, No. 16, August 15, 1963, pp. 4813–4818.

31. Lilley, A. E., Harvard College Observatory, Private communication, 1962.

32. Deirmendjian, D., Paper presented at the Liège Astrophysical Colloquium, June 1963.

33. Spinrad, H., "Spectroscopic Temperature and Pressure Measurements in the Venus Atmosphere," *Publications of the Astronomical Society of the Pacific*, Vol. 74, No. 438, June 1962, pp. 187–201.

34. McCullough, T. P., and Boland, J. W., "Observations of Venus at 2.07 cm," *The Astronomical Journal*, Vol. 69, No. 1, February 1964, p. 68.

REFERENCES (Cont'd)

35. Barrett, A. H., and Chung, V. K., "Method for Determination of High-Altitude Water-Vapor Abundance from Ground-Based Microwave Observations," *Journal of Geophysical Research*, Vol. 67, No. 11, October 1962, pp. 4259–4266.

36. Bottema, M., Plummer, W., and Strong, J., "Water Vapor in the Atmosphere of Venus," *The Astrophysical Journal*, Vol. 139, No. 3, April 1, 1964, pp. 1021–1022.

37. Dollfus, A., "Physique Planétaire—Observation de la vapeur d'eau sur la planéte Vénus," *Comptes Rendus Hebdomadaires des Séances de L'académie des Sciences*, Vol. 256, No. 15, 8 April 1963, pp. 3250–3253.

38. Spinrad, H., "A Search for Water Vapor and Trace Constituents in the Venus Atmosphere," *Icarus*, Vol. 1, No. 3, October 1962, pp. 266–270.

39. Menzel, D. H., and Whipple, F. L., "The Case for H_2O Clouds on Venus," *Publications of the Astronomical Society of the Pacific*, Vol. 67, No. 396, June 1955, pp. 161–168.

40. Gibson, J. E., and Corbett, H. H., "Brightness Temperature of Venus at 1.35 cm," *The Astronomical Journal*, Vol. 68, No. 1, February 1963, p. 74.

41. Barrett, A. H., "Microwave Spectral Lines as Probes of Planetary Atmospheres," *Proceedings of the Eleventh International Astrophysical Symposium*, Liège, Belgium, July 9–12, 1962, pp. 197–219.

42. Kaplan, L. D., *Proceedings of the International Symposium on Molecular Structure and Spectroscopy*, Tokyo, Science Council of Japan, B407, pp. 1–4, 1962.

43. Thaddeus, P., "Structure of the Venus Atmosphere," Paper presented at the 45th annual meeting of the American Geophysical Union, Washington, D. C., April 21–24, 1964.

44. Kaplan, L. D., *A Preliminary Model of the Venus Atmosphere*, Technical Report No. 32-379, Jet Propulsion Laboratory, Pasadena, Calif., December 12, 1962.

45. Goldstein, H., *Propagation of Short Radio Waves*, D. E. Kerr, ed., McGraw-Hill Book Co., Inc., New York, New York, 1951.

46. Smyth, C. P., *Dielectric Behavior and Structure; Dielectric Constant and Loss, Dipole Moment and Molecular Structure*, McGraw-Hill Book Co., Inc., New York, New York, 1955.

47. Jones, D. E., "An Analysis of the Mariner 2 Venus Probe Microwave Radiometer Experiment," *Transactions, American Geophysical Union*, Vol. 44, No. 4, December 1963, pp. 886–887.

48. Muhleman, D. O., "The Electrical Characteristics of the Atmosphere and Surface of Venus from Radar Observations," *Icarus*, Vol. 1, No. 5–6, April 1963, pp. 401–411.

49. Sagan, C., and Giver, L., Paper presented at the American Geophysical Union Symposium on Radio Emission and Thermal Structure of the Venus Atmosphere, UCLA, December 27, 1961.

REFERENCES (Cont'd)

50. Davenport, W. B., Jr., and Root, W. L., *An Introduction to the Theory of Random Signals and Noise,* McGraw-Hill Book Co., Inc., New York, New York, 1958.

51. Barrett, A. H., Massachusetts Institute of Technology, Private communication, 1963.

52. Stratton, J. A., *Electromagnetic Theory,* 1st ed., McGraw-Hill Book Co., Inc., New York, New York, 1941.

53. Chen, S. N. C., and Peake, W. H., "Apparent Temperatures of Smooth and Rough Terrain," *Institute of Radio Engineers Transactions on Antennas and Propagation,* Vol. AP-9, No. 6, November 1961, pp. 567–572.

54. Taylor, R. C., "Terrain Return Measurements at X, K_u and K_a Band," *Institute of Radio Engineers National Convention Record,* Vol. 7, Part 1, March 23–26, 1959, pp. 19–26.

APPENDIX A

In the development of the RC time constant restoration formula, it is assumed that the radiometer integrator circuit can be represented by a simple RC circuit. A careful study of the calibration waveforms indicates that the actual output response of the integrator could not have differed markedly from this. With the indicated input and output we have (Refs. 50 and 51)

$$y(t) = \int_0^\infty x(t-\tau)\, h(\tau)\, d\tau \tag{A-1}$$

and

$$x(t-\tau) = \frac{1}{2\pi}\int_{-\infty}^{\infty} X(j\omega)\, e^{j\omega(t-\tau)}\, d\omega \tag{A-2}$$

Hence

$$\begin{aligned} y(t) &= \frac{1}{2\pi}\int_0^\infty \int_{-\infty}^{\infty} X(j\omega)\, e^{j\omega(t-\tau)}\, h(\tau)\, d\omega\, d\tau \\ &= \frac{1}{2\pi}\int_{-\infty}^{\infty} X(j\omega)\, H(j\omega)\, e^{j\omega t}\, d\omega \\ &= \frac{1}{2\pi}\int_{-\infty}^{\infty} Y(j\omega)\, e^{j\omega t}\, d\omega \end{aligned} \tag{A-3}$$

where

$$Y(j\omega) = X(j\omega)\, H(j\omega)$$

For the assumed RC circuit, with $H(j\omega)$ defined as V_{out}/V_{in},

$$\begin{aligned} H(j\omega) &= \frac{V_{out}}{V_{in}} = \frac{IZ_c}{V_{in}} = \frac{\left(\dfrac{V_{in}}{R + \dfrac{1}{j\omega C}}\right)\dfrac{1}{j\omega C}}{V_{in}} \\ &= \frac{1}{1 + j\omega RC} \end{aligned} \tag{A-4}$$

Hence

$$X(j\omega) = Y(j\omega)(1 + j\omega RC) \tag{A-5}$$

Then the input is related to the output by

$$x(t) = \frac{1}{2\pi}\int_{-\infty}^{\infty} Y(j\omega)\,(1 + j\omega RC)\, e^{j\omega t}\, d\omega$$

or

$$x(t) = y(t) + RC\frac{dy}{dt} \tag{A-6}$$

This equation was used to remove time-constant smoothing effects from the smooth curves drawn through the data points.

For the alternate approach to the data reduction, the equation relating the output in terms of the input to an RC integrator circuit was required. It is easy to show that for an integrator circuit and a step function input,

$$h(\tau) = \frac{1}{RC}\, e^{-\tau/RC} \tag{A-7}$$

Therefore, using Eq. (A-1),

$$y(t) = \int x(t-\tau)\,\frac{e^{-\tau/RC}}{RC}\, d\tau \tag{A-8}$$

Letting $\alpha(t) = x(t)$ normalized to unity at midscan, or

$$x(t) = k'\alpha(t)$$

there results

$$y(t) = k'\int \alpha(t-\tau)\,\frac{\exp(-\tau/RC)}{RC}\, d\tau \tag{A-9}$$

APPENDIX B

The assumed expression for the absorption coefficient due to CO_2 in the presence of N_2 was (see Ref. 5)

$$\alpha^*_{CO_2} = \frac{\alpha_0^* \nu^2 P^2_{CO_2}}{T^{3.7}}\left(1 + 0.378\frac{P_{N_2}}{P_{CO_2}}\right) \text{cm}^{-1} = \frac{\alpha_0' \nu^2 P_T^2}{T^{3.7}} \tag{B-1}$$

where

$$\alpha_0' = \alpha_0^* \epsilon'^2_{CO_2}\left(1 + 0.378\frac{P_{N_2}}{P_{CO_2}}\right)$$

$$\epsilon'_{CO_2} = \frac{P_{CO_2}}{P_T}$$

$$\alpha_0^* = 8.89 \times 10^{-32}$$

In order to obtain equations compatible with either an adiabatic or subadiabatic lapse rate, a subadiabatic index ($\zeta \geq 1$) was assumed, where the true temperature lapse rate would be ζ^{-1}, the adiabatic lapse rate.

Hence

$$\frac{\partial T}{\partial h} = -\frac{g}{\zeta C_p} \tag{B-2}$$

Then

$$T = T_s - \frac{\beta}{\zeta} h \tag{B-3}$$

where

$$\beta = \frac{\gamma - 1}{\gamma}\frac{mg}{k}$$

γ being the ratio of specific heats. For the pressure variation with height, we note that, assuming an ideal gas, or

$$P = nkT$$

we have

$$\frac{dP}{dh} = nk\frac{dT}{dh} + kT\frac{dn}{dh} \tag{B-4}$$

Since

$$\frac{dP}{dh} = -\rho g$$

$$\frac{dn}{dh} = \frac{1}{m}\frac{d\rho}{dh}$$

there results

$$-\rho g = \frac{\rho k}{m}\frac{dT}{dh} + \frac{kT}{m}\frac{d\rho}{dh}$$

$$= -\frac{\rho k}{m}\frac{\beta}{\zeta} + \frac{k}{m}(T_s - \rho/\zeta h)\frac{d\rho}{dh} \tag{B-5}$$

and

$$\frac{dh}{\frac{k}{m}\left(T_s - \frac{\beta}{\zeta}h\right)} = \frac{d\rho}{\left(\frac{k}{m}\frac{\beta}{\zeta} - g\right)\rho} \tag{B-6}$$

Integrating from 0 to h and from ρ_0 to ρ, there is obtained (see also Ref. 9)

$$P = P_s\left(\frac{T}{T_s}\right)^{\zeta\gamma/(\gamma-1)} \tag{B-7}$$

The brightness temperature is given by

$$T_B = \epsilon T_s \exp(-\tau_{\max}\delta) + \left[\int_0^{\tau_a'} T\exp(-\tau_a\delta)\delta\, dT\right]\exp(-\tau_c'\,\delta) + T_c$$

$$\times\left[1 - \exp(-\tau_c'\,\delta)\right] + T_R \tag{B-8}$$

where T_R is the contribution to T_B of the atmospheric radiation that strikes the surface, is reflected, and is then attenuated by the atmosphere above the surface.

Also

$$\delta = \frac{\sqrt{R_p^2\cos^2\theta + 2R_pH + H^2} - R_p\cos\theta}{H} \tag{B-9}$$

with R_p the radius of Venus (to the hard surface), and H the height above the surface. For the midpoints of the scan, δ is approximated by sec θ.

Since

$$\tau_a = \int_h^{H_c}\alpha dh = \alpha_0'\nu^2\int\frac{P^2}{T^{3.7}}\,dh \tag{B-10}$$

making the substitutions

$$P^2 = P_s^2\left(\frac{T}{T_s}\right)^{2\zeta\gamma/(\gamma-1)}$$

$$dh = -\frac{\zeta}{\beta}\,dT$$

results in

$$\tau_a = -\frac{\alpha_0' \nu^2 P_s^2 \zeta}{\beta T_s^{(2\zeta\gamma)/(\gamma-1)}} \int_T^{T_c} T^{\{[(2\zeta-2.7)\gamma+2.7]/(\gamma-1)-1\}}\, dT$$

$$= \frac{\alpha_0' \nu^2 P_s^2 \zeta}{\beta T_s^{(2\zeta\gamma)/(\gamma-1)}} \left(\frac{\gamma-1}{a}\right)\left(T^{a/(\gamma-1)} - T_c^{a/(\gamma-1)}\right) \tag{B-11}$$

where

$$a = (2\zeta - 2.7)\gamma + 2.7 \tag{B-12}$$

Hence

$$\tau_a' = \frac{\alpha_0' \nu^2 P_s^2 \zeta (\gamma-1)}{\beta T_s^{(2\zeta\gamma)/(\gamma-1)} a} T_c^{a/(\gamma-1)} \left[\left(\frac{T_s}{T_c}\right)^{a/(\gamma-1)} - 1\right] \tag{B-13}$$

which reduces to the adiabatic expression used by Barrett (Ref. 5) when $\zeta = 1$. Some simplification results if we let A be defined by

$$A = \frac{\zeta \alpha_0' \nu^2 P_s^2}{\beta T_s^{(2\zeta\gamma)/(\gamma-1)}}$$

For the isothermal portion

$$(\tau_{iso})_{max} = \tau_c' = \int_{H_c}^{\infty} \alpha\, dh = \frac{\alpha_0' \nu^2}{T_2^{3.7}} \int_{H_c}^{\infty} P_c^2 \exp\left[-2\eta(h - H_c)\right] dh = \frac{\alpha_0' \nu^2 P_c^2}{2mg\, T_c^{3.7}} \tag{B-14}$$

Since

$$\frac{P_s^2}{T_s^{(2\zeta\gamma)/(\gamma-1)}} T_c^{a/(\gamma-1)} = \frac{P_c^2}{T_c^{(2\zeta\gamma-a)/(\gamma-1)}} = \frac{P_c^2}{T_c^{2.7}} \tag{B-15}$$

then

$$\tau_{max} = \tau_c' \left\{1 + \frac{2\zeta\gamma}{a}\left[\left(\frac{T_s}{T_c}\right)^{a/(\gamma-1)} - 1\right]\right\} \tag{B-16}$$

Also

$$\alpha^* T\, dh = -\frac{\zeta \alpha_0' \nu^2 P_s^2}{\beta T_s^{(2\zeta\gamma)/(\gamma-1)}} T^{a/(\gamma-1)}\, dT \tag{B-17}$$

Finally

$$T_B = \epsilon T_s \exp(-\tau_{max} \sec\theta) + A \exp(-\tau_c' \sec\theta) \int T^{a/(\gamma-1)} \exp(-\tau_a \sec\theta) \sec\theta\, dT$$

$$+ T_c \left[1 - \exp(-\tau_c' \sec\theta)\right] + T_R \tag{B-18}$$

Note that an infinitely narrow antenna beamwidth has been assumed. Even more important, since we have assumed an ideal gas, no allowance is made for the variation of C_p with P and T, which is caused by the fact that the gas is not ideal. Any departure from the assumption of an ideal gas, such as utilizing the fact that $\gamma = \gamma(P, T)$, would in fact require a rederivation of the pressure–temperature relationship of Eq. (B-7), not only in the requirement of one of the other forms of the gas law, such as the van der Waals equation, but also in the requirement for modification of the temperature equation (B-3). Such a refinement was not justified.

The reflected radiation term, T_R, will of course depend upon the character of the surface. Basically, several possibilities exist: the surface is perfectly rough (a diffuse scatterer), perfectly smooth, or somewhere between these two extremes. If the surface is perfectly smooth, then the Fresnel reflection coefficients (Ref. 52) can be used leading to

$$\epsilon_h = 1 - \frac{\left(\cos\theta - Q^{1/2}\cos\frac{\psi}{2}\right)^2 + Q\sin^2\frac{\psi}{2}}{\left(\cos\theta + Q^{1/2}\cos\frac{\psi}{2}\right)^2 + Q\sin^2\frac{\psi}{2}} \tag{B-19}$$

$$\epsilon_v = 1 - \frac{\left(\epsilon_r\cos\theta - Q^{1/2}\cos\frac{\psi}{2}\right)^2 + \left(\epsilon_i\cos\theta + Q^{1/2}\sin\frac{\psi}{2}\right)^2}{\left(\epsilon_r\cos\theta + Q^{1/2}\cos\frac{\psi}{2}\right)^2 + \left(\epsilon_i\cos\theta - Q^{1/2}\sin\frac{\psi}{2}\right)^2} \tag{B-20}$$

where

$$Q = \left[(\epsilon_r - \sin^2\theta)^2 + \epsilon_i^2\right]^{1/2} \tag{B-21}$$

$$\psi = \tan^{-1}\left(\frac{-\epsilon_i}{\epsilon_r - \sin^2\theta}\right) \tag{B-22}$$

and ϵ_r and ϵ_i are the real and imaginary components of the complex dielectric coefficient of the surface material. For this case, T_R becomes

$$\begin{aligned} T_R(\theta) = {} & \zeta[1-\epsilon(\theta)]A\exp\left\{-\left[\zeta A\left(\frac{\gamma-1}{a}\right)T_s^{a/(\gamma-1)} + \tau_{\max}\right]\sec\theta\right\} \\ & \times \int_{T_c}^{T_s} T^{a/(\gamma-1)}\exp\left[\zeta A\left(\frac{\gamma-1}{a}\right)T^{a/(\gamma-1)}\sec\theta\right]\sec\theta\, dT \\ & + [1-\epsilon(\theta)]T_c\,[1-\exp(-\tau_c'\sec\theta)]\exp[-(\tau_a' + \tau_{\max})\sec\theta] \end{aligned} \tag{B-23}$$

If the surface is not a perfectly diffuse scatterer, the emissivity or reflectivity will depend upon the bistatic scattering coefficient of the surface. The expression for the emissivity becomes (see S. N. C. Chen and W. H. Peake, Ref. 53) for the predominantly diffuse case

$$\epsilon_{pd} = 1 - \frac{1}{4\pi}\int\left[\gamma_h(\theta_0,\phi_0,\theta_s,\phi_s) + \gamma_v(\theta_0,\phi_0,\theta_s\phi_s)\right]d\Omega_s \tag{B-24}$$

where γ_h and γ_v are the bistatic scattering coefficients and where (θ_0,ϕ_0) and (θ_s,ϕ_s) refer to the direction from which radiation impinges on the surface and the

direction into which radiation is scattered, respectively. The subscripts h and v refer to horizontal and vertical polarization, respectively. The reflected atmospheric radiation T_R is then given for the predominantly diffuse case

$$T_R = \zeta A \int_{\Omega_s} (1-\epsilon_{pd}) \exp\left\{-\left[\zeta A\left(\frac{\gamma-1}{a}\right) T_s^{a/(\gamma-1)}\, \zeta(\theta_s) + \tau_{\max} \sec\theta\right]\right\}$$
$$\times \left\{\int_{T_c}^{T_s} T^{a/(\gamma-1)} \exp\left[\zeta A\left(\frac{\gamma-1}{a}\right) T^{a/(\gamma-1)}\, \delta(\theta_s)\right] \delta(\theta_s)\, dT\right\} d\Omega_s$$
$$+ \int_{\Omega_s} (1-\epsilon_{pd})\, T_c \left\{1 - \exp\left[-\tau_c' \delta(\theta_s)\right] \exp\left[-\tau_a' \delta(\theta_s) + \tau_{\max} \sec\theta\right]\right\} d\Omega_s \tag{B-25}$$

If (see Chen and Peake)

$$\gamma(0, s) = \frac{\gamma_0}{2} \frac{(\cos\theta_0 + \cos\theta_s)}{\cos\theta_0} \tag{B-26}$$

then

$$\epsilon_{pd} = 1 - \gamma_0\left(\frac{1}{4} + \frac{1}{8}\sec\theta_0\right) \tag{B-27}$$

At 15Gc, $\gamma_0 \sim 0.070$ (see R. C. Taylor, Ref. 54) and hence at $\theta = 0$, 0.833, and 1.0492 radians, $\epsilon_{pd} = 0.973$, 0.978, and 0.966 respectively. Considering the *Mariner* data, these values are sufficiently close that the complex expression of Eq. (B-24) can be replaced by the idealized diffuse-scatterer approximation to the surface. Hence

$$T_R \simeq (1-\epsilon_d)\, A \exp\left\{-\left[\zeta A\left(\frac{\gamma-1}{a}\right) T_s^{a/(\gamma-1)}\, \bar{\delta} + \tau_{\max} \sec\theta\right]\right\}$$
$$\times \int_{T_c}^{T_s} T^{a/(\gamma-1)} \exp\left[\zeta A\left(\frac{\gamma-1}{a}\right) T^{a/(\gamma-1)}\, \bar{\delta}\right] \bar{\delta}\, dT$$
$$+ (1-\epsilon_d) T_c \left[1 - \exp(-\tau_c'\, \bar{\delta})\right] \exp\left[-(\tau_a'\, \bar{\delta} + \tau_{\max} \sec\theta)\right] \tag{B-28}$$

where

$$\bar{\delta} = \frac{2}{\pi} \int_0^{\pi/2} \frac{\sqrt{R_p^2 \cos^2\theta + 2R_pH + H^2} - R_p \cos\theta}{H}\, d\theta$$
$$\approx \frac{2}{\pi}\left(\frac{R_p+H}{H}\right) \int_0^{\pi/2} \left[\sqrt{1 - k^2 \sin^2\theta} - \left(\frac{1}{R_p+H}\right)\cos\theta\right] d\theta \tag{B-29}$$

with $k = R_p/R_p + H$. An average H has been assumed, a simplification justified by the data. The first integral, being an elliptic integral of the second kind, is tabulated for values of k, and with the models of Venus considered here, there results $\bar{\delta} \sim 2$.

APPENDIX C

The parameters, equations, etc., pertinent to the various regions for the multilayer line absorption model are (see Fig. 41)

Region A

$$H_a - H_b = 60 \times 10^5 \text{ cm}$$

$$\Delta h_a = \frac{H_a - H_b}{m + 1}$$

$$m = 19$$

$$\alpha^*_{a_i} = 7.61 \times 10^{-13} \frac{\epsilon'_a P_{a_i} \nu^2 \exp\left(-\frac{644}{T_a}\right)}{T_a^{7/2}} \left[\frac{\Delta\nu_{a_i}}{(\nu - \nu_0)^2 + (\Delta\nu_{a_i})^2}\right] + 5.50 \times 10^{-36} \frac{\epsilon'_a P_{a_i} \nu^2 \Delta\nu_{a_i}}{T_a^{5/2}} + \frac{\alpha'_0 \nu^2 P^2_{a_i}}{T_a^{3.7}}$$

$$P_{a_i} = P_{ab} \exp\left\{-\eta_a \left[H_a - H_b - (i+1)\Delta h_a\right]\right\}$$

$$P_{ab} = P_{bc}\left(\frac{T_{ab}}{T_{bc}}\right)^{(\zeta_b \gamma)/(\gamma - 1)}$$

$$\eta_a = \frac{mg}{kT_a}$$

and

$$\Delta\nu_{a_i} = \frac{2.58 \times 10^3 P_{a_i}}{(T_a/318)^{0.625}} \left\{1 + 1.384 \times 10^{-19} \frac{\epsilon'_a P_{a_i}}{kT_a}\right\}$$

if $\Delta\nu_{a_i}$ was computed to be greater than $\Delta\nu = 3.18 \times 10^4$.

If $\Delta\nu_{a_i}$ was computed to be $\leq 3.18 \times 10^4$, then $\Delta\nu_{a_i}$ was set equal to 3.18×10^4.

$$T_a = 200 = T_{ab}$$

$$T_{bc} = 250$$

$$\zeta_b = 3.3$$

Region B

$$H_b - H_c = (T_{bc} - T_{ac}) \frac{\zeta_b}{\beta}$$

$$\beta = \frac{\gamma - 1}{\gamma} \frac{mg}{k}$$

$$\Delta h_b = \frac{H_b - H_c}{n + 1}$$

$$n = 9$$

$$\alpha^*_{b_i} = 7.61 \times 10^{-13} \frac{\epsilon'_{b_i} P_{b_i} \nu^2 \exp\left(-\frac{644}{T_{b_i}}\right)}{T_{b_i}^{5/2}} \left[\frac{\Delta\nu_{b_i}}{(\nu-\nu_0)^2 + (\Delta\nu_{b_i})^2}\right]$$

$$+ 5.50 \times 10^{-36} \frac{\epsilon'_{b_i} P_{b_i} \nu^2 \Delta\nu_{b_i}}{T_{b_i}^{5/2}} + \frac{\alpha'_0 \nu^2 P_{b_i}^2}{T_{b_i}^{3.7}}$$

$$\epsilon'_{b_i} = \epsilon'_a$$

$$P_{b_i} = P_{bc}\left(\frac{T_{b_i}}{T_{bc}}\right)^{(\zeta_b\gamma)/(\gamma-1)}$$

$$T_{b_i} = T_{bc} - \frac{\beta}{\zeta_b}\left[H_b - H_c - (i+1)\Delta h_b\right]$$

$$\Delta\nu_{b_i} = \frac{2.58 \times 10^3 P_{b_i}}{(T_{b_i}/318)^{0.625}}\left\{1 + 1.384 \times 10^{-19} \frac{\epsilon'_{b_i} P_{b_i}}{kT_b}\right\}$$

Region C

$$H_c - H_d = (T_d - T_{bc})\frac{\zeta_c}{\beta}$$

$$\Delta h_c = \frac{H_c - H_d}{p+1}$$

$$p = 9$$

$$\alpha^*_{c_i} = 7.61 \times 10^{-13} \frac{\epsilon'_{c_i} P_{c_i} \nu^2 \exp\left(-\frac{644}{T_{c_i}}\right)}{T_{c_i}^{7/2}}$$

$$\times \left[\frac{\Delta\nu_{c_i}}{(\nu-\nu_0)^2 + (\Delta\nu_{c_i})^2} + \frac{\Delta\nu_{c_i}}{(\nu+\nu_0)^2 + (\Delta\nu_{c_i})^2}\right]$$

$$+ 5.50 \times 10^{-36} \frac{\epsilon'_{c_i} P_{c_i} \nu^2 \Delta\nu_{c_i}}{T_{c_i}^{5/2}}$$

$$+ \frac{\alpha'_0 \nu^2 P_{c_i}^2}{T_{c_i}^{3.7}}$$

$$\Delta\nu_{c_i} = \frac{2.58 \times 10^3 P_{c_i}}{(T_{c_i}/318)^{0.625}}\left(1 + 1.384 \times 10^{-19} \frac{\epsilon'_{c_i} P_{c_i}}{kT_{c_i}}\right)$$

$$P_{c_i} = \left(\frac{T_{c_i}}{T_d}\right)^{(\zeta_c\gamma)/(\gamma-1)}$$

$$T_{c_i} = T_d - \frac{\beta}{\zeta_c}\left[H_c - H_d - (i+1)\Delta h_c\right]$$

$$T_d = 350$$

Region D

$$H_d - H_e = \frac{\chi'}{\eta_d}$$

$$\chi' = 1$$

$$\eta_d = \frac{mg}{kT_d}$$

$$\Delta h_d = \frac{H_d - H_e}{q+1}$$

$$q = 9$$

$$\alpha^*_{d_i} = 7.61 \times 10^{-13} \frac{\epsilon'_{d_i} P_{d_i} \nu^2 \exp\left(-\frac{644}{T_d}\right)}{T_{d_i}^{7/2}} \times \left[\frac{\Delta\nu_{d_i}}{(\nu-\nu_0)^2 + (\Delta\nu_{d_i})^2} + \frac{\Delta\nu_{d_i}}{(\nu+\nu_0)^2 + (\Delta\nu_{d_i})^2}\right] + 5.50 \times 10^{-36} \frac{\epsilon'_{d_i} P_{d_i} \nu^2 \Delta\nu_{d_i}}{T_d^{5/2}} + \frac{\alpha'_0 \nu^2 P^2_{d_i}}{T_d^{3.7}} + \frac{\tau_d}{(q+1)\Delta h_d}$$

$$P_{d_i} = P_{de} \exp\{-\eta_d[H_d - H_c - (i+1)\Delta h_d]\}$$

$$\epsilon'_{d_i} = \epsilon'_d = \epsilon'_c$$

$$\Delta\nu_{d_i} = \frac{2.58 \times 10^3 P_{d_i}}{(T_d/318)^{0.625}}\left(1 + 1.384 \times 10^{-19} \frac{\epsilon'_{d_i} P_{d_i}}{kT_d}\right)$$

$$\tau_d = \tau_{15.8}\left(\frac{\nu}{15.8 \times 10^9}\right)^2$$

$$\tau_{15.8} = 0.135$$

Region E

$$H_e = \left(T_s - T_d \frac{\zeta_e}{\beta}\right)$$

$$\Delta h_c = \frac{H_e}{r+1}$$

$$r = 49$$

$$\alpha^*_{e_i} = 7.61 \times 10^{-13} \frac{\epsilon'_{e_i} P_{e_i} \nu^2 \exp\left(-\frac{644}{T_{e_i}}\right)}{T_{e_i}^{7/2}} \times \left[\frac{\Delta\nu_{e_i}}{(\nu-\nu_0)^2 + (\Delta\nu_{e_i})^2} + \frac{\Delta\nu_{e_i}}{(\nu+\nu_0)^2 + (\Delta\nu_{e_i})}\right] + 5.50 \times 10^{-36} \frac{\epsilon'_{e_i} P_{e_i} \nu^2 \Delta\nu_{e_i}}{T_{e_i}^{5/2}} + \frac{\alpha'_0 \nu^2 P^2_{e_i}}{T_{e_i}^{5.7}}$$

$$\Delta\nu_{e_i} = \frac{2.58 \times 10^3 P_{e_i}}{(T_{e_i}/318)^{0.625}}\left(1 + \frac{1.384 \times 10^{-19} \epsilon'_{e_i} P_{e_i}}{kT_{e_i}}\right)$$

$$P_{e_i} = P_s \left(\frac{T_{e_i}}{T_s}\right)^{(\zeta_e \gamma)/(\gamma-1)}$$

$$T_{e_i} = T_s - \frac{\beta}{\zeta_e}\left[H_e - (i+1)\,\Delta h_e\right]$$

$$\zeta_e = \zeta_c = 1.5$$

Since the line absorption model discussed in Section VI involved calculations with θ varying from 0 to 90 deg, the approximation leading to the usage of sec θ could not be used. In our case (see Fig. C-1), we have for the optical path to the observer (neglecting refraction) from the point P

$$x_i = x - x_0$$

$$x = \sqrt{R_p^2 \cos^2\theta + 2R_p H_a + H_a^2} - R_p \cos\theta \qquad \text{(C-1)}$$

$$x_{0_i} = \sqrt{R_p^2 \cos^2\theta + 2R_p h_i + h_i^2} - R_p \cos\theta \qquad \text{(C-2)}$$

Then

$$x_i = \sqrt{R_p^2 \cos^2\theta + 2R_p H_a + H_a^2} - \sqrt{R_p^2 \cos^2\theta + 2R_p h_i + h_i^2} \qquad \text{(C-3)}$$

Defining

$$\delta_i = \frac{x_i}{H_a - h_i}$$

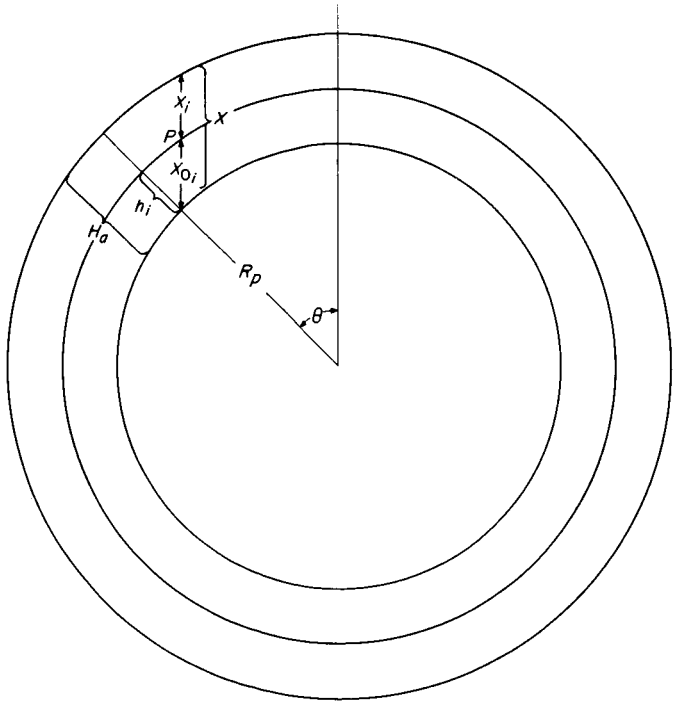

Fig. C-1. Allowance for curvature for a stratified atmosphere

we have

$$\Delta x_i = \delta_i \, \Delta h_i$$

For region B, for example, there results

$$\Delta x_{b_i} = \Delta h_{b_i} \frac{\sqrt{R_p^2 \cos^2\theta + 2R_p H_a + H_a^2} - \sqrt{R_p^2 \cos^2\theta + 2R_p h_{b_i} + h_{b_i}^2}}{H_a - h_{b_i}} \tag{C-4}$$

where

$$h_{b_i} = \sum_{j=i+1}^{n} h_{b_j} + H_c + H_d + H_e \tag{C-5}$$

In order to simplify the problem somewhat, an average curvature factor was used, namely

$$\delta_i \to \delta = \frac{\sqrt{R_p^2 \cos^2\theta + 2R_p H_a + H_a^2} - R_p \cos\theta}{H_a} \tag{C-6}$$

In view of the accuracy of the data, this simplification was felt to be justified.

The expression for T_R used for this model was that appropriate for reflection from a smooth surface. Here, T_R is given by

$$\begin{aligned}
T_R = (1-\epsilon') \Bigg\{ & T_a \left[1 - \exp\left(-\alpha_{a_0} \Delta h_a \, \delta\right)\right] \exp\left[-\left(\sum_{i=1}^{m} \alpha_{a_i}^* \Delta h_a + \tau_b + \tau_c + \tau_d + \tau_e + \tau_{\max}\right)\delta\right] \\
& + T_R \sum_{i=1}^{m} \left[1 - \exp\left(-\alpha_{a_i}^* \Delta h_a \, \delta\right)\right] \exp\left[-\left(\sum_{j=i+1}^{m} \alpha_{a_i}^* \Delta h_a + \tau_b + \tau_c + \tau_d + \tau_e + \tau_{\max}\right)\delta\right] \\
& + T_{b_0} \left[1 - \exp\left(-\alpha_{b_0}^* \Delta h_b \, \delta\right)\right] \exp\left[-\left(\sum_{i=1}^{n} \alpha_{b_i}^* \Delta h_b + \tau_c + \tau_d + \tau_e + \tau_{\max}\right)\delta\right] \\
& + \sum_{i=1}^{n} T_{b_i} \left[1 - \exp\left(-\alpha_{b_i}^* \Delta h_b \, \delta\right)\right] \exp\left[-\left(\sum_{j=i+1}^{n} \alpha_{b_i}^* \Delta h_b + \tau_c + \tau_d + \tau_e + \tau_{\max}\right)\delta\right] \\
& + T_{c_0} \left[1 - \exp\left(-\alpha_{c_0}^* \Delta h_c \, \delta\right)\right] \exp\left[-\left(\sum_{i=1}^{p} \alpha_{c_i}^* \Delta h_c + \tau_d + \tau_e + \tau_{\max}\right)\delta\right] \\
& + \sum_{i=1}^{p} T_{c_i} \left[1 - \exp\left(-\alpha_{c_i}^* \Delta h_c \, \delta\right)\right] \exp\left[-\left(\sum_{j=i+1}^{p} \alpha_{c_i}^* \Delta h_c + \tau_d + \tau_e + \tau_{\max}\right)\delta\right] \\
& + T_d \left[1 - \exp\left(-\alpha_{d_0}^* \Delta h_d \, \delta\right)\right] \exp\left[-\left(\sum_{i=1}^{q} \alpha_{d_i}^* \Delta h_d + \tau_e + \tau_{\max}\right)\delta\right] \\
& + T_d \sum_{i=1}^{q} \left[1 - \exp\left(-\alpha_{d_i}^* \Delta h_d \, \delta\right)\right] \exp\left[-\left(\sum_{j=i+1}^{q} \alpha_{d_i}^* \Delta h_d + \tau_e + \tau_{\max}\right)\delta\right] \\
& + T_{e_0} \left[1 - \exp\left(-\alpha_{e_0}^* \Delta h_e \, \delta\right)\right] \exp\left[-\left(\sum_{i=1}^{r} \alpha_{e_i}^* \Delta h_e + \tau_{\max}\right)\delta\right] \\
& + \sum_{i=1}^{r} T_{e_i} \left[1 - \exp\left(-\alpha_{e_i}^* \Delta h_e \, \delta\right)\right] \exp\left[-\left(\sum_{j=i+1}^{r} \alpha_{e_i}^* \Delta h_e + \tau_{\max}\right)\delta\right] \Bigg\}
\end{aligned} \tag{C-7}$$

ACKNOWLEDGMENT

I would like to express my sincere gratitude to the engineering staff of the Jet Propulsion Laboratory, whose skill and perseverance made the *Mariner II* spacecraft successful. The tireless efforts of the Radio Science Group at JPL, particularly of F. T. Barath, E. J. Johnston, M. L. Kellner, E. A. De Rosa and H. L. Renger, are greatly appreciated. I also wish to thank the computer staff at JPL and in particular M. H. Horton for the programming of the various models.

I also wish to express my appreciation to the co-experimenters Drs. A. H. Barrett, J. Copeland, and A. E. Lilley and particularly to Dr. J. R. Ballif, of Brigham Young University, for their encouragement and many helpful discussions.